Synthesis of Nanoparticles of Iron Oxide, Silver and Gold for Photodegradation and Detection of 2,4,6-Trinitrotoluene

By

Gloria Marcela Herrera Sandoval

A dissertation of thesis submitted in partial fulfillment of the requirements for the degree of

DOCTOR OF PHILOSOPHY
in
Applied Chemistry
(Environmental Chemistry)

UNIVERSITY OF PUERTO RICO
MAYAGÜEZ CAMPUS

_____   _____
Samuel P. Hernández-Rivera, PhD   Date
President, Graduate Studies Committee

_____   _____
Arturo Hernández-Maldonado, PhD   Date
Member Graduate Studies Committee

_____   _____
Nilka Rivera-Portalatín, PhD   Date
Member Graduate Studies Committee

_____   _____
Félix Román-Velázquez, PhD   Date
Member Graduate Studies Committee

_____   _____
Ernesto Otero-Morales, PhD   Date
Representative of Graduate Studies

_____   _____
René S. Vieta, PhD   Date
Chairperson of the Department

ABSTRACT

Various nano-structured materials were synthesized to be used in the purification and detection of contaminants in water. Iron oxides and extruded polystyrene/TiO_2 nanocomposites were synthesized, characterized and evaluated for potential applications as a photocatalyst in water treatment processes in which heterogeneous photocatalysis forms an essential part. Three iron oxides were synthesized and characterized by X-ray diffraction as hematite, magnetite and Au/magnetite. The last oxide consists of magnetite coated with gold nanoparticles to improve its effectiveness in photodegradation treatments. A dye (methylene blue) was chosen as the test molecule to evaluate dye discoloration during the photocatalytic process. Degradation of about 90% was observed at 6 h of exposure to ultraviolet light. Similarly, a decrease of over 90% in orto-nitrophenol concentration was observed at 3 h of treatment. These results suggest that B-Fe_3O_4 and Au/Fe_3O_4 can be used as photocatalyst, to remove contaminants present in water. Taking advantage of their magnetic properties, the oxides may be easily removed from water after the proposed application. Also, satisfactory outcomes were obtained for aqueous solutions of 2,4,6-trinitrotoluene (TNT). The results show that at 9 h of the process 2,4 6-trinitrotoluene concentration decreased to 80% of the initial values. During the study, parameters such as pH, irradiation wavelength and addition of H_2O_2 as oxidant were evaluated.

Degradation of solutions of the highly energetic material cyclotrimethylenetrinitramine (commonly known as RDX) was studied at three wavelengths of ultraviolet radiation (240, 254, and 365 nm). The results show that at 240 and 254 nm, the RDX solutions were degraded without the presence of the photocatalyst. At 365 nm the

cyclotrimethylenetrinitramine was resistant to degradation without presence of photocatalyst. Degradation of 70% percent of the explosive in solutions was observed in the presence of magnetite. Also, an evaluation of the degradation of TNT at three pH values (pH = 4, 7, and 9) was carried out. Degradation of 43% was obtained over a period of 3 h of treatment at pH 9.

Furthermore, when EPS/TiO$_2$ was evaluated as photocatalyst, methylene blue (MB) solutions were efficiently decolorized using ultraviolet radiation at 254 nm and an intensity value of 600 mW/cm^2. The results show a 98% discoloration of MB in solution. A higher stability of the polymer was evidenced through of the incorporation of TiO$_2$ using thermal analysis.

Finally, gold and silver nanoparticles were prepared by laser ablation, using water as solvent. 4-Aminobenzenethiol was chosen as probe molecule to determine if nanoparticles deposited served to increase vibrational signals in surface enhanced Raman scattering (SERS) experiments. Parameters such as ablation time and pH of the suspensions were evaluated. TNT was used as analyte to probe if metallic nanoparticles can be substrates in SERS experiments. The results demonstrate that gold and silver nanoparticle substrates prepared by the methods developed show favorable results based on the studies conducted and could be the basis for the development of micro sensors.

RESUMEN

Varios materiales nanoestructurados se sintetizaron con el fin de usarse en la purificación y la detección de contaminantes en agua. Óxidos de hierro y un nanocompuesto de EPS/TiO$_2$ se prepararon en forma sencilla y posteriormente se caracterizaron y evaluaron en aplicaciones como fotocatalizadores en procesos de tratamiento de aguas llamados Tecnologías de Oxidación Avanzada, dentro de los cuales se encuentra fotocatálisis heterogénea. Tres óxidos de hierro se sintetizaron e identificaron por difracción de rayos x como hematita, magnetita y Au/magnetita. A este último se le agregaron partículas de oro con el fin de mejorar el tratamiento de fotodegradación. El colorante azul de metileno (MB, por siglas en inglés) fue escogido como molécula de prueba para evaluar la descoloración del tinte bajo el proceso de fotocatálisis. Los resultados muestran una degradación de alrededor de 90% a 6 h de exposición a la luz UV. Igualmente, un decrecimiento de más de 90% en la concentración del compuesto ortonitrofenol (ONP por siglas en inglés) se observó a 3h de tratamiento. Esto indica que los óxidos B-Fe$_3$O$_4$ y Au/Fe$_3$O$_4$ podrían ser utilizados como fotocatalizadores, para eliminar contaminantes presentes en el agua. Tomando ventaja de las propiedades magnéticas, los óxidos podrían ser fácilmente retirados del agua. Igualmente, buenos resultados fueron obtenidos cuando 2,4,6-trinitrotolueno (TNT) fue utilizado como compuesto para ser removido del agua y se encontró que a 9 h del proceso, la concentración del explosivo había disminuido en un 80%. Se evaluaron los efectos de pH, longitud de onda de irradiación y adición H$_2$O$_2$ como un agente oxidante.

La degradación de una solución de RDX se estudió a 3 longitudes de onda (240 nm, 254 nm and 365 nm). Los resultados muestran que a 240 y 254 nm RDX tiende a degradarse sin la presencia del fotocatalizador; pero a 365 nm (rayos solares) RDX fue resistente a la degradación sin presencia del fotocatalizador. Se encontró Una degradación de 70% del explosivo en presencia de magnetita. Se llevó a cabo una evaluación de la degradación de TNT a tres diferentes pH (4, 7 y 9). Se alcanzó 43% de degradación a 3 h de análisis para pH = 9.

Por otra parte, el nanocompuesto EPS/TiO$_2$ fue eficientemente decolorando MB bajo una radiación de 254 nm y una intensidad de 600 mW/cm^2. Los resultados muestran un 98% de descoloración de MB. Una mayor estabilidad del polímero fue demostrada debido a la incorporación de TiO$_2$ a través de análisis térmico.

Finalmente, nanopartículas de oro y plata fueron preparadas usando ablación por láser y agua como solvente. El compuesto 4-aminobencenothiol se elegió como molécula de prueba para determinar si las nanopartículas depositadas sirven para aumentar la señal Raman. Se evaluaron parámetros tales como tiempo de ablación y pH del agua. Un material altamente energético, 2,4,6-trinitrotolueno (TNT) se utilizó como analito en los experimentos de amplificación de la señal Raman. Los espectros Raman se midieron utilizando un microespectrómetro Raman. Los resultados demuestran que los sustratos de oro y plata fabricados por los métodos desarrollados muestran resultados prometedores para detección usando la técnica de aumento de señal Raman y podría conducir al desarrollo de micro sensores.

This dissertation contains portions that were published by the author in the Journal of Materials Science and Applications (published by Scientific Research), Nanomaterials (published by MDPI online) and the Nanoscale Research Letters (published by Springer)

Este título se lo quiero dedicar a Dios, porque gracias a su fortaleza hemos llegado hasta aquí. A mis dos bellos hijos Jesús y María, quienes llenan mi vida y me dan las fuerzas para continuar. A mi esposo Olben Okieff, a quien amo y siempre ha creído en mí... A mis padres Gloria y Juan...y mis hermanos...quienes llevo pegados a mi alma y corazón en todo momento...

ACKNOWLEDGMENTS

I want to thank my *alma mater*, the University of Puerto Rico, Mayagüez Campus, for the opportunity of concluding my graduate studies at this prestigious academic institution. I want to thank my advisor Dr. Samuel P. Hernández-Rivera, for his help and dedication. Thanks for believing in me and for the opportunity to be part of his research team for the past nine years. I am very grateful of all the members of my graduate committee, Dr. Arturo Hernández-Maldonado for his collaboration and support in this work, to Dr. Félix Román-Velázquez for serving on my committee and for reviewing my work, to Dr. Nilka Rivera-Portalatín, for her wise suggestions and her availability in every moment. Particular thanks to Dr. Ernesto Otero for his help. Special thanks to Dr. Francisco Márquez-Linares, for the opportunity to carry out research during my internship at the University of Turabo. Thanks to María Cotto, Verónica Castro, Carmen Bonilla and Abraham for their pleasant company and help in all moments during the development of my internship. I am grateful with Dr. Rolando Roque in the University of Turabo for facilitating some experiments during my internship.

Thanks to my dear husband Olben ... because he's been with me all the time giving me encouragement and support at all times. We have shared the happy and sad moments and he has been my support in the difficult times. Special thanks to, my super friends Dr. Sandra Natalia Correa, Dr. Andrea Cabanzo, Dr. Hilsamar Félix, Bibiana Báez, Yleana Colón, and Ana Gómez, for their friendship, collaboration and support. To my lab partners: Eduardo Espinosa, Pedro Fierro, and José Ruiz, thanks for their assistance and support during long days of work. I am sincerely grateful to Aracelys and

TABLE OF CONTENTS

ABBREVIATION LIST

BOD	Biochemical oxygen demand
sAOT	Advanced oxidation technologies
CTAB	Cetyltrimethylammonium bromide
LC	Liquid chromatography
GC	Gas chromatography
MS	Mass spectrometry
SSER	Surface enhanced Raman spectroscopy
RS	Raman spectroscopy
Au	Gold
Ag	Silver
NPs	Nanoparticles
TNT	Trinitrotoluene
B-Fe_3O_4	Magnetite
R-Fe_2O_3	Hematite
MB	Methylene blue
HPLC	High-performance liquid chromatograph
RDX	Ciclotrimethylentrinitramine
L-H	Langmuir-Hinshelwood
UV	Ultraviolet
EPS	Expanded polystyrene
TiO_2	Titanium dioxide
PS	Polystyrene
SEM	Scanning electron microscope
TEM	Transmission electron microscope
TGA	Thermal gravimetric analyzer
4-ABT	4-aminobenzenethiol
SEF	Surface enhancement factor
XRD	X-ray diffraction
FT-IR	Fourier transformer infrared
RS	Raman spectroscopy
rpm	Revolution per minute
DTGS	Deuterated triglycine sulfate
nm	Nanometers
AC	Active carbon
HR -TEM	High resolution transmission electron microscope
BET	Brunauer-Emmett-Teller
ppm	Parts per million
mg	milligrams

LIST OF FIGURES

LIST OF TABLES

Chapter 1

INTRODUCTION

Small amounts of common household products are discharged to sewage waters every day. Among these are caffeine, hormones, detergents, antibiotics and pharmaceuticals compounds. Most of these persist in the environment (Murray, 2010) since treatment plants are not designed to remove these emerging contaminants (Deblonde, 2011). This global problem has aroused the interest of scientists, who have carried out a series of investigations to generate alternative processes whose primary goal is to prevent such compounds to reach water resources considered appropriate for consumption. Therefore, a great emphasis has been placed on the study of various advanced and tertiary treatment processes (Klavarioti, 2009). There are numerous ongoing initiatives in this new field in order to design efficient and low cost wastewater treatment technologies.

In recent years Advanced Oxidation Technologies (AOTs), have been widely used for pollutant degradation and detoxification of wastewater containing recalcitrant compounds. This technology is based on production of hydroxyl radicals (OH•), which are known for being a powerful and non-selective oxidizing agent (2.8 V compared to standard hydrogen electrode). During the process organic matter is mineralized producing organic residues and inorganic anions, CO_2 and H_2O. Advanced Oxidation Processes (AOP), on the other hand, is the term given to a number of technologies that use strong oxidizing agents such as ozone, ultraviolet light, ultrasound and homogeneous and heterogeneous catalysis degradation.

Heterogeneous photocatalysis is based on the use of a catalyst for the generation of hydroxyl radicals. This is carried out through surface level redox reactions due to the action of UV light and the presence of an oxidizing agent such as oxygen in air or hydrogen peroxide in water. In the interfacial region between the excited radicals and the solid solution, reactions take place that destroy contaminants, without the photocatalyst undergoing chemical changes. The photocatalyst may be used immobilized on supported or in suspension form to increase the surface area available to reaction. If the photocatalyst is immobilized on a support, a subsequent separation step is avoided and the material can be reused. The most recognized photocatalyst to date is commercial titanium dioxide (TiO_2, also known as Degussa P25). This is the most widely used unsupported photocatalyst due to its superior effectiveness in degradation processes (Hincapié-Mejía, 2011; Valencia, 2011). Heterogeneous photocatalysis has employed other semiconductor catalysts such as ZnO, Fe_2O_3, Fe_3O_4, CdS, GaP, and ZnS. These have demonstrated their efficiency in degrading a wide range of refractory organics into readily biodegradable compounds, eventually mineralizing them to form innocuous carbon dioxide and water (Chong, 2010).

During the last few years, synthesis of iron oxide particles (Etienne, 2012; Mamoru, 2004; Masashi, 2005) has attracted a great deal of attention because these nanoparticles (NPs) exhibit electrical, optical and magnetic properties that are different from their bulk counterparts (Diamandescu, 1999; Mandel, 2011; Xavier, 2002). Iron oxides include $-Fe_2O_3$, $-Fe_2O_3$ and Fe_3O_4 and exhibit different structures: $-Fe_2O_3$ has a corundum structure, while the other two have cubic structure (James, 2005). The study of iron oxides has attracted attention over the past decades due to the extended

range of applications in catalysis (Chang, 2004; Fajaroh, 2013; Herrmann, 1995), printing ink (Principi, 1993), gas sensors (Althainz, 1995; Aronniemi, 2008; Belle, 2011), ferrofluids (Markus, 2008; Rinaldi C., 2004), high density magnetic recording media (Principi, 1993), magnetic resonance imaging (Rozenman, 1991; Yilmaz, 2013) and biomedical applications (Figuerola, 2010; Gupta, 2005; F. Marquez, 2011; F. Marquez, Herrera, G., Campo, T., Cotto, M., Duconge, J., Sanz, J., Elizalde, E., Perales, O., and Morant, C., 2012) among others. Many synthetic procedures have been used, according to the nature of the magnetic particles required. These methods include reduction of iron salts in micelles (Martino, 1997), thermal reactions (El-Sheikh, 2009), electrochemical methods (Nasibi, 2012), co-precipitation (Sowichai, 2012), microemulsions (Chin, 2007; Wongwailikhit, 2011), hydrothermal synthesis (Behdadfar, 2012; Daou, 2006; Diamandescu, 1999) and sol gel method (Khaleel, 2012). All these methods of preparing iron oxide nanostructures are in general complicated and expensive (Hosseinian, 2011).

In Chapter 2 of this work, we report the synthesis of NPs of iron oxide through a hydrothermal method using inexpensive metal salts, cetyltrimethylammonium bromide (CTAB), urea and water. In addition, the applications of iron oxide as photocatalysts were explored. For improving photocatalytic properties of iron oxide gold was added to magnetite during the synthesis and its photocatalytic activity was also studied.

Chapter 3 reports a study on the parameters that influence photodegradation processes. Irradiation wavelength, pH, and addition of H_2O_2 were studied to determine the optimal conditions for degradation processes when magnetite and Au/magnetite are used as photocatalysts.

Chapter 4 presents an easy procedure for the preparation of nanocomposites of TiO$_2$ and expanded polystyrene (EPS). This study presents a new and simple way to recycle EPS into an EPS/TiO$_2$ nanocomposite. The new material was characterized by transmission electron microscopy (TEM), scanning electron microscopy (SEM), thermal gravimetric analysis (TGA), Fourier transformer-infrared (FT-IR) and Raman spectroscopy (RS). Photocatalytic experiments were conducted to evaluate the catalytic properties of this new material. In addition, the results were compared with those from commercially available TiO$_2$.

Chapter 5 includes a description of the synthesis of gold (Au) and silver (Ag) NPs prepared by laser ablation in water as solvent. Laser ablation in liquid occurs when a high-power laser beam is focused for a fixed time onto a solid target that is submerged in a liquid (see Figure 1.1). The metal target is placed at the focal point of a lens and heated by laser action. Due to the heat transferred from the metal spot, the liquid layer immediately adjacent to the solid surface is also heated to a high local temperature which is a much higher than the boiling point of the liquid at normal pressure. The liquid is, therefore, vaporized producing a high temperature, high-pressure plasma plume containing highly ionized species. The plume expands violently shattering the melted target material into nano-sized clusters that are super cooled by the surrounding liquid (Fukata, 2005; Kabashin, 2006; Okada, 2007).

In surface enhanced Raman scattering (SERS) experiments conducted with the ablated nanoparticles, 4-aminobenzebethiol (4-ABT) was chosen as probe molecule to determine the optimum irradiation time and the pH of aqueous synthesis of the laser

4

ablation-based synthesis of metallic NPs. A highly energetic material, TNT, was used as the target compound in the SERS experiments.

The most important conclusions obtained during the development of this thesis are given in Chapter 6.
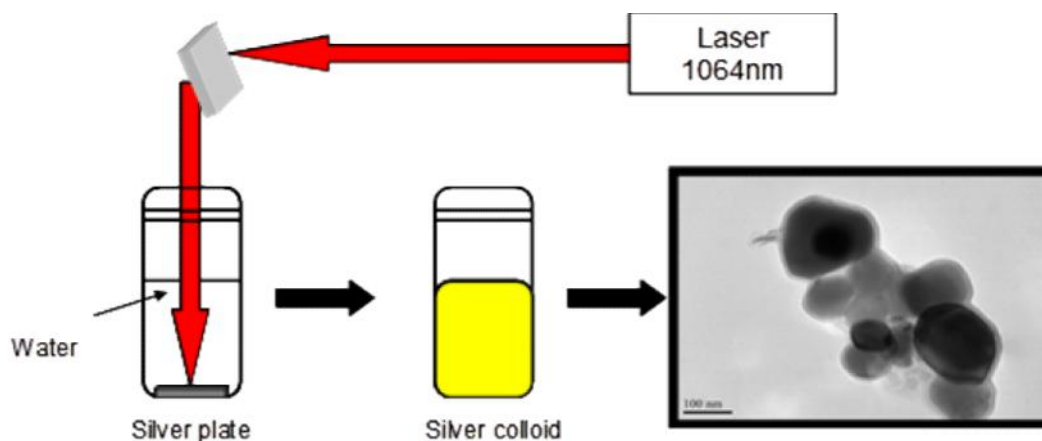
Figure 1.1. Schematic for the laser ablation procedure of gold and silver nanoparticles in water.

References

Althainz, P., Schuy, L., Goschnick, J., and Ache, H.J. (1995), 'The influence of morphology on the response of iron-oxide gas sensors', *Sens. Actuators, B,* 25 (1–3), 448-450.

Aronniemi, M., Saino, J., and Lahtinen, J. (2008), 'Characterization and gas-sensing behavior of an iron oxide thin film prepared by atomic layer deposition', *Thin Solid Films,* 516 (18), 6110-6115.

Behdadfar, B., Kermanpur, A., Sadeghi-Aliabadi, H., Morales, M.d.P., and Mozaffari, M. (2012), 'Synthesis of high intrinsic loss power aqueous ferrofluids of iron oxide nanoparticles by citric acid-assisted hydrothermal-reduction route', *J. Solid State Chem.,* 187 (0), 20-26.

Belle, C.J., Bonamin, A., Simon, U., Santoyo-Salazar, J., Pauly, M., Bégin-Colin, S., and Pourroy, G. (2011), 'Size dependent gas sensing properties of spinel iron oxide nanoparticles', *Sens. Actuators, B,* 160 (1), 942-950.

Chang, C.M., Wang, Y.J., Lin, C., and Wang, M.K. (2004), 'Novel predicting methods for the removal of divalent metal ions by magnetite/amorphous iron oxide composite systems', *Colloids Surf., A,* 234 (1–3), 1-7.

Chin, A.B. and Yaacob, I.I. (2007), 'Synthesis and characterization of magnetic iron oxide nanoparticles via w/o microemulsion and Massart's procedure', *J. Mater. Process. Technol.,* 191 (1–3), 235-237.

Chong, M.N., Jin, B., Chow, C.W.K., and Saint, C. (2010), 'Recent developments in photocatalytic water treatment technology: A review', *Water Res.,* 44 (10), 2997-3027.

Daou, T.J., Pourroy, G., Bégin-Colin, S., Grenèche, J.M., Ulhaq-Bouillet, C., Legaré, P., Bernhardt, P., Leuvrey, C., and Rogez, G. (2006), 'Hydrothermal Synthesis of Monodisperse Magnetite Nanoparticles', *Chem. Mater.,* 18 (18), 4399-4404.

Deblonde, T., Cossu-Leguille, C., and Hartemann, P. (2011), 'Emerging pollutants in wastewater: A review of the literature', *Int. J. Hyg. Environ. Health,* 214 (6), 442-448.

Diamandescu, L., Mihaila-Tarabasanu, D., Popescu-Pogrion, N., Totovina, A., and Bibicu, I. (1999), 'Hydrothermal synthesis and characterization of some polycrystalline -iron oxides', *Ceram. Int.,* 25 (8), 689-692.

El-Sheikh, S.M., Harraz, F.A., and Abdel-Halim, K.S. (2009), 'Catalytic performance of nanostructured iron oxides synthesized by thermal decomposition technique', *J. Alloys Compd.,* 487 (1–2), 716-723.

Etienne, D., Marie-Hélène, D., and Stéphane, M. (2012), 'Synthesis and Characterisation of Iron Oxide Ferrite Nanoparticles and Ferrite-Based Aqueous Fluids', in Thanh, N.T.K. (ed.), *Magnetic Nanoparticles* (Boca Raton, FL.: CRC Press, Taylor & Francis Group), 47-72.

Fajaroh, F., Setyawan, H., Nur, A., and Lenggoro, I.W. (2013), 'Thermal stability of silica-coated magnetite nanoparticles prepared by an electrochemical method', *Adv. Powder Technol.,* 24 (2), 507-511.

Figuerola, A., Di Corato, R., Manna, L., and Pellegrino, T. (2010), 'From iron oxide nanoparticles towards advanced iron-based inorganic materials designed for biomedical applications', *Pharmacol. Res.,* 62 (2), 126-143.

Fukata, N., Oshima, T., Tsurui, T., Ito, S., and Murakami, K. (2005), 'Synthesis of silicon nanowires using laser ablation method and their manipulation by electron beam', *Sci. Technol. Adv. Mater.,* 6 (6), 628-632.

Gupta, A.K. and Gupta, M. (2005), 'Synthesis and surface engineering of iron oxide nanoparticles for biomedical applications', *Biomaterials,* 26 (18), 3995-4021.

Herrmann, J.M. (1995), 'Heterogeneous photocatalysis: an emerging discipline involving multiphase systems', *Catal. Today,* 24 (1–2), 157-164.

Hincapié-Mejía, G.M., Ocampo, D., Restrepo, G.M., and Marín, J.M. (2011), 'Fotocatálisis Heterogénea y Foto-Fenton Aplicadas al Tratamiento de Aguas de Lavado de la Producción de Biodiesel', *Información tecnológica,* 22, 33-42.

Hosseinian, A.R., H.; Mahjoub, A. R. (2011), 'Preparation of Nanosized Iron Oxide and their Photocatalytic Properties for Congo Red', *World Academy of Science, Engineering and Technology,* 52, 736-739.

James, A. and Nikolla, Q. (2005), in Lal, R. (ed.), *Encyclopedia of Soil Science* (2nd edn.; Boca Raton, FL: CRC Press, Taylor & Francis Group).

Kabashin, A.V.M., M. (2006), 'Laser ablation-based synthesis of functionalized colloidal nanomaterials in biocompatible solutions.', *J. Photochem. Photobiol., A,* 182 (3), 330-334.

Khaleel, A. and Al-Marzouqi, A. (2012), 'Alkoxide-free sol–gel synthesis of aerogel iron–chromium mixed oxides with unique textural properties', *Mater. Lett.,* 68 (0), 385-387.

Klavarioti, M., Mantzavinos, D., and Kassinos, D. (2009), 'Removal of residual pharmaceuticals from aqueous systems by advanced oxidation processes', *Environ. Int.,* 35 (2), 402-417.

Mamoru, S. (2004), 'Iron Oxide Nanoparticles', *Dekker Encyclopedia of Nanoscience and Nanotechnology* (6; New York, USA: Marcel Dekker, Inc.).

Mandel, K., Hutter, F., Gellermann, C., and Sextl, G. (2011), 'Synthesis and stabilisation of superparamagnetic iron oxide nanoparticle dispersions', *Colloids Surf., A,* 390 (1–3), 173-178.

Markus, Z., Carlos, R., Tahir, C., and Thomas, F. (2008), 'Magnetic Ferrofluids', *Dekker Encyclopedia of Nanoscience and Nanotechnology, Second Edition - Six Volume Set (Print Version)* (CRC Press), 1922-1938.

Marquez, F., Campo, T., Cotto, M., Polanco, R., Roque, R., Fierro, P., Sanz, J., Elizalde, E., and Morant, C. (2011), 'Synthesis and characterization of monodisperse magnetite hollow microspheres', *Soft Nanosci Lett,* 1, 25 - 32.

Marquez, F., Herrera, G., Campo, T., Cotto, M., Duconge, J., Sanz, J., Elizalde, E., Perales, O., and Morant, C. (2012), 'Preparation of hollow magnetite microspheres and their applications as drugs carriers', *Nanoscale Res. Lett.,* 7 (1), 210.

Martino, A., Stoker, M., Hicks, M., Bartholomew, C.H., Sault, A.G., and Kawola, J.S. (1997), 'The synthesis and characterization of iron colloid catalysts in inverse micelle solutions', *Appl. Catal., A,* 161 (1–2), 235-248.

Masashi, I. (2005), 'Solvothermal Synthesis', *Chemical Processing of Ceramics, Second Edition* (Materials Engineering; Boca Raton, FL: CRC Press, Taylor & Francis Group), 21-64.

Murray, K.E., Thomas, S.M., and Bodour, A.A. (2010), 'Prioritizing research for trace pollutants and emerging contaminants in the freshwater environment', *Environ. Pollut.,* 158 (12), 3462-3471.

Nasibi, M., Golozar, M.A., and Rashed, G. (2012), 'Nano iron oxide (Fe2O3)/carbon black electrodes for electrochemical capacitors', *Mater. Lett.,* 85 (0), 40-43.

Okada, T. and Suehiro, J. (2007), 'Synthesis of nano-structured materials by laser-ablation and their application to sensors', *Appl. Surf. Sci.,* 253 (19), 7840-7847.

Principi, G., Maddalena, A., Gupta, A., Bottoni, G., Candolfo, D., Cecchetti, A., and Corradi, A.R. (1993), 'Structural and magnetic characterization of metal particles used as magnetic recording media', *Nucl. Instrum. Methods Phys. Res., Sect. B,* 76 (1–4), 143-145.

Rinaldi C., C.T., Franklin T., Zahn M. (2004), 'Magnetic Nanoparticles in Fluid Suspension', *Dekker Encyclopedia of Nanoscience and Nanotechnology - Six Volume Set (Print Version)* (Boca Raton, FL.: CRC Press, Taylor & Francis Group).

Rozenman, Y., Zou, X., and Kantor, H.L. (1991), 'Magnetic resonance imaging with superparamagnetic iron oxide particles for the detection of myocardial reperfusion', *Magn. Reson. Imaging,* 9 (6), 933-939.

Sowichai, K., Supothina, S., Nimittrakoolchai, O.-u., Seto, T., Otani, Y., and Charinpanitkul, T. (2012), 'Facile method to prepare magnetic multi-walled carbon nanotubes by in situ co-precipitation route', *J. Ind. Eng. Chem.,* 18 (5), 1568-1571.

Valencia, S.H., Marín, J.M., and Restrepo, G.M. (2011), 'Efecto del pH en la Degradación Fotocatalítica de Materia Orgánica Natural', *Información tecnológica,* 22, 57-66.

Wongwailikhit, K. and Horwongsakul, S. (2011), 'The preparation of iron (III) oxide nanoparticles using W/O microemulsion', *Mater. Lett.,* 65 (17–18), 2820-2822.

Xavier, B. and Amílcar, L. (2002), 'Finite-size effects in fine particles: magnetic and transport properties', *J. Phys. D: Appl. Phys.,* 35 (6), R15.

Yilmaz, A., Rösch, S., Klingel, K., Kandolf, R., Helluy, X., Hiller, K.-H., Jakob, P.M., and Sechtem, U. (2013), 'Magnetic resonance imaging (MRI) of inflamed myocardium using iron oxide nanoparticles in patients with acute myocardial infarction — Preliminary results', *Int. J. Cardiol.,* 163 (2), 175-182.

Chapter 2

SYNTHESIS OF HEMATITE, MAGNETITE AND Au/Fe$_3$O$_4$: CHARACTERIZATION AND EVALUATION OF PHOTOCATALYTIC ACTIVITY

Abstract

Three oxides were synthesized through a hydrothermal method. The oxides obtained presented differences in color and oxidation states. The phases identified were, magnetite and hematite. To obtain better catalytic properties, gold nanoparticles were added to the iron oxides during the synthesis to obtain a gold/magnetite composite. X-ray diffraction, Raman and infrared spectra were used to characterize the oxides. The photocatalytic degradation of iron oxides methylene blue (MB) and ortho-nitrophenol (ONP) were photodegraded using ultraviolet radiation at 254 nm by addition of fixed amounts of nano-oxide to aqueous solutions of the target contaminants in known concentrations. The quantitative analysis of pollutant degradation was carried out using ultraviolet-visible spectrometry and high-performance liquid chromatography equipped with diode array ultraviolet detector. The decrease in the characteristic absorption band of MB was attributed to the oxidative degradation of the organic compound by iron oxides. Magnetite and gold/magnetite showed the best performance in photocatalytic degradation of MB and ONP.

Keywords: photodegradation, heterogeneous photocatalysis, photocatalyst, degradation, TNT, iron oxide, magnetite, hematite.

2.1 Introduction

Investigations on iron oxides started when early on in development of human kind in applications such in and technological areas and in art. Scientists have found many applications in various fields, the first and main of these oxides was its use as paint additive. Oxidation processes of iron were the first topic of interest to researchers in this area, developing a large number of investigations in corrosion processes (Stratmann, 1990). Applications of iron oxides have continued to expand thanks to technological advances and investigations conducted. Iron oxides are used as magnetic inks (Spratt, 2001), magnetic seals in motors (Charles, 1987; Ravaud, 2010), optical memory instruments, gyroscopes (Snowball, 1997), magnetic refrigeration units (Pecharsky, 2006; Yu, 2003), marking cell separation (Kinoshita, 2007), contrast media in clinical imaging (Corot, 2006) , transportation and release of drugs (Marquez, 2012; Maver, 2009) and hyperthermia with magnetic fluids (Ito, 2005; Mürbe, 2008).

There are two major global issues of concern to scientists, the first is about searching for new materials that contribute to human health and the second issue is research of new materials that improve the quality of the environment. The still emerging field of nanotechnology has pursued the search for materials with photocatalytic properties with the ability to degrade pollutants in water and air. Recent scientific interest in TiO_2 mediated photocatalysis has been motivated by observations that aqueous solutions of colloidal TiO_2 nanoparticles exhibit significantly enhanced chemical and photochemical reactivity due to so-called quantum size effects (Ao, 2008; Bahnemann, 2004; Gimeno, 2005). Iron oxides present similar properties as photocatalyst (Lei, 2006; Wang, 2009). The photocatalytic activity of -Fe_2O_3 colloids

has been compared to the activities of colloidal suspensions of ZnO and TiO$_2$ (Kormann, 1989). Moreover, some oxides present an important properties such as their magnetic behavior that permit that the nanoparticles of oxides can be recovered.

In this study, experiments were conducted to explore the photocatalytic degradation by iron oxides powders in nano sized; the same procedure was used to obtain gold/iron oxide. The oxides were characterized using XRD, SEM, FT-IR and Raman spectroscopic techniques. Photocatalytic capacity was evaluated using MB and two nitrocompounds (2,4,6-trinitrotoluene and ONP) as contaminants.

2.2 Materials and Methods

2.2.1 *Synthesis of metal oxides nanoparticles through hydrothermal method*

For a typical synthesis, 2 mmol of Fe(NO$_3$)$_3$·9H$_2$O (99.98% analytical grade, Fisher Scientific International), 1 gram of CTAB (HPLC grade, Sigma-Aldrich Chemical Company) and 15 mmol urea (HPLC grade, Sigma-Aldrich Chemicals) were dissolved in 35 mL of distilled, deionized water (ddH$_2$O). The solution was placed in a vacuum oven at 70 °C, at 16 Pa for 24 h. The products were recovered by several cycles of centrifugation (8000 rpm/5 min), rinsed with ddH$_2$O, and finally charred at 550 °C to remove organic residues (Liu, 2007). In the synthesis of catalyst Au/Fe$_2$O$_3$, the same procedure was used but the water was replaced by a gold solution (HAuCl$_4$, HPLC grade, Sigma-Aldrich) at 1% w/w.

2.2.2 *Characterization of oxides*

The size, shape, and spectroscopic properties of nanoparticles were the principal parameters studied of oxides obtained. Surface area measurements were carried out using the Brunauer-Emmett-Teller (BET) method where nitrogen adsorption isotherms as well as surface area measurements were performed using nitrogen at 77 K as described elsewhere (Ao, 2008; Gimeno, 2005; Wang, 2009). Before measurements, the samples were degassed using heating at a rate of 5 K/min and an evacuation rate of 50 mmHg/s for 4 h. XRD patterns were recorded in the 2 h range of 15–85 °C at a scan rate of 4 °C/min on XRD Siemens.

Spectroscopic characterization was carried out. Raman spectra were collected using a Renishaw RM2000 micro-Raman: equipped with 532 and 785 nm excitation sources. Raman spectra were acquired using the following conditions: spectral range: 100-3200 cm^{-1}, accumulations: 2, acquisition time: 20 s, laser Power levels: 10 – 60 mW. A Bruker Optics IFS 66 series Fourier transformer infrared (FT-IR) interferometer coupled to infrared microscope and deuterated triglycine sulfate (DTGS) detector running under OPUS v. 4.0. FT-IR experiments were used to obtain spectra of nano-sized oxides prepared.

Sizes and morphology of nano-oxides were obtained from images acquired with a high-resolution transmission electron microscope (HR-TEM), Carl Zeiss (Peabody, MA), model 922 operated at 200 kV. TEM grids were prepared by insertion of 3 µL of NPs suspensions on ultrathin carbon film/holey carbon 400 mesh copper grids (01824) obtained from Ted Pella, Inc. (Redding, CA). The solvent was evaporated at room temperature and the grids were kept in desiccators promote a dust free atmosphere.

2.2.3 *Photocatalytic evaluation of nano-sized oxides in contaminated water*

The photocatalytic activity of nano-sized oxides was evaluated using selected pollutants as targets: MB, ONP and 2,4,6-trinitrotoluene (TNT). A systematic study was conducted by exposing aqueous solution of target analytes, to which known amounts of nano oxides were added, to an ultra violet (UV) radiation source The suspensions were irradiated at 254 nm with an intensity of 600 mW/cm^2 measured by a UV-A radiation meter. At given time intervals, aliquots from the suspensions were removed and immediately centrifuged at 8500 rpm. The supernatant liquid was analyzed using an Agilent 8453 UV-Visible spectrometer. During the irradiation, the solutions were stirred to keep the homogenous suspensions. The temperature was maintained at 25 °C. Quantitative analyses of nitrocompounds were carried out using an HPLC. Parameters for HPLC and other instruments were based on results reported by Cruz-Uribe et al. (Cruz-Uribe, 2007), Psillakis et al. (Psillakis, 2000), Correa (Correa-Torres, 2011) and Baez et al. (Baez, 2006). The analyses were carried out in an Agilent Technologies HPLC, model 1100, equipped with diode-array UV-VIS detector (model 996), a quaternary pump model G1311A, and an automatic injector (G1313A). The HPLC methodology was performed in reverse-phase mode using Eclipse XDB-C$_{18}$ columns (150 mm, 5 μm ID, 4.6 particle size) at room temperature, with isocratic mobile phases consisting of a mixture of water/methanol (50:50). The flow rate used was 1.0 mL/min for 10 min. The method was based on EPA 8330, designed for trace analysis of explosives residues by HPLC coupled to a UV detector, with some modifications. The samples that can be analyzed by this method are explosives residues in water, soil, or sediment matrices.

2.3 Results and discussion

2.3.1 *Characterizations of nano-sized oxides prepared*

All samples were obtained through the reaction between iron nitrate and water under hydrothermal conditions at 70 °C. During the calcination procedure two different compounds were obtained. The first compound exhibited a red-brown color characteristic of hematite (R-Fe_2O_3). During the second synthesis a black colored iron oxide was obtained, with high resemblance to magnetite (B-Fe_3O_4). The same procedure was used to prepare Au/Fe_3O_4. Figure 2.1 shows the XRD patterns for the prepared powders of iron oxide and gold iron oxide. The most abundant phase identified as red–brown iron oxide was Fe_2O_3 (hematite). The narrow and high intensity peaks of samples show that the prepared powders are highly crystalline and the average crystallite size was calculated using the diffractions peaks from Scherer's equation. The size average of crystal calculated for three samples of nano-sized oxide was 63.91 nm for red oxide, 9 nm for black oxide and 21 nm for the Au doped oxide. The data is summarized in Table 1. Results of BET analysis are also included. The results of XRD patterns for hematite and magnetite are shown in Figure 2.2 to demonstrate differences in their reflections. The strong peaks at 2θ = 104, 110, and 116 are characteristic of the X-ray pattern of α-Fe_2O_3 (hematite), namely the (110) reflection (in rhombohedral coordinates). Additionally, much weaker peaks that correspond to the (102), (104), (113), (024), (214), and (300) planes (Souza, 2009).
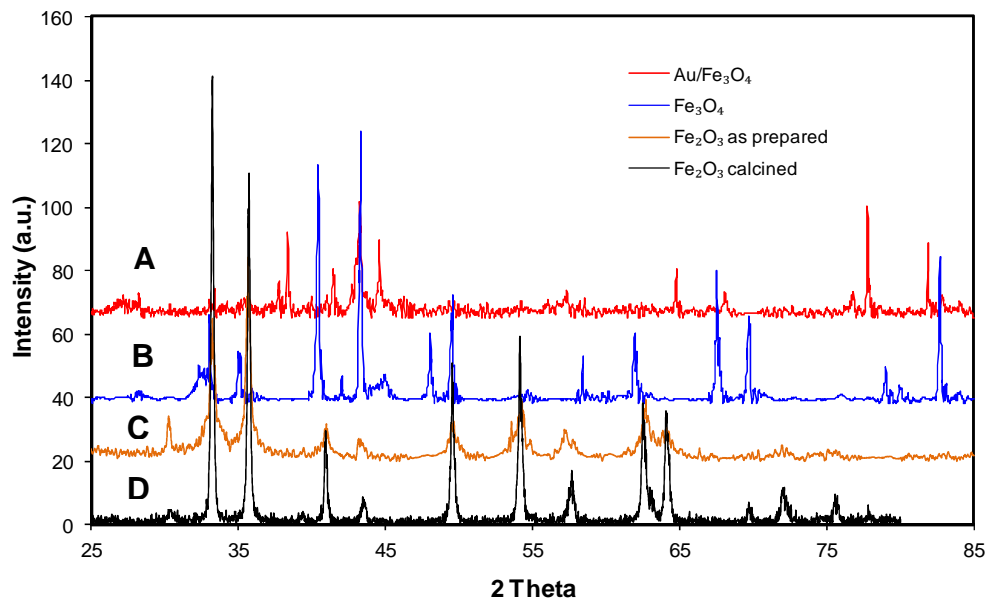
Figure 2.1. XRD patterns of, A: Black Au/Fe$_3$O$_4$, B: Black /Fe$_3$O$_4$, C: as-prepared Fe$_2$O$_3$, and D: calcined red iron oxide (Fe$_2$O$_3$).
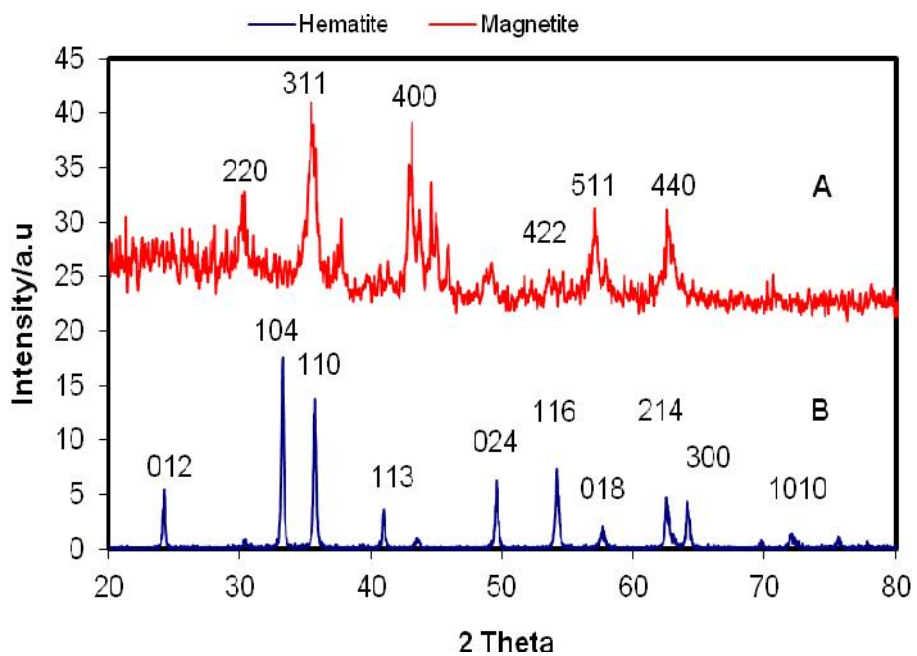
Figure 2.2. Figure 2.1. XRD patterns of, A: Black Au/Fe3O4, B: Black /Fe3O4, C: as-prepared Fe$_2$O$_3$, and D: calcined red iron oxide (Fe$_2$O$_3$).
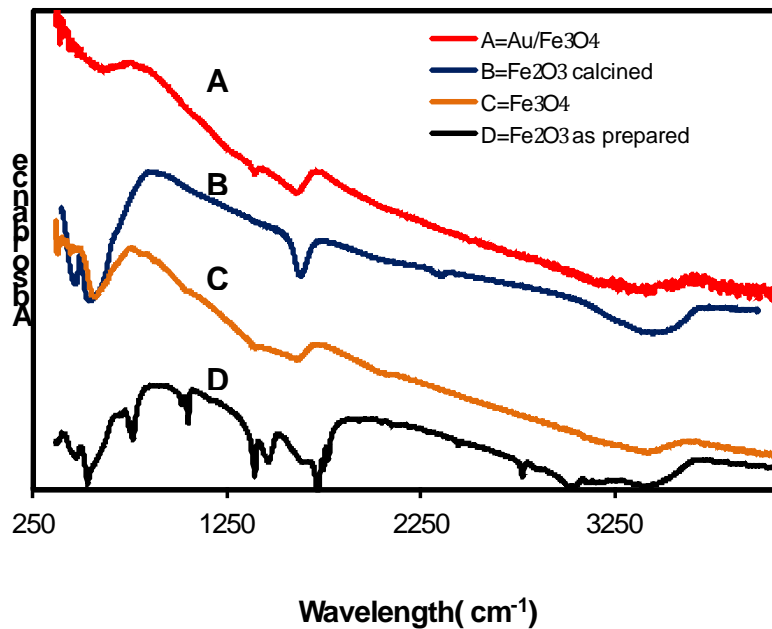
Figure 2.3. FT-IR spectra of as-prepared nanosized iron oxide of, A: Black Au/Fe$_3$O$_4$. B: calcined red iron oxide (Fe$_2$O$_3$), C: Black Fe$_3$O$_4$, and D: the as-prepared Fe$_2$O$_3$.
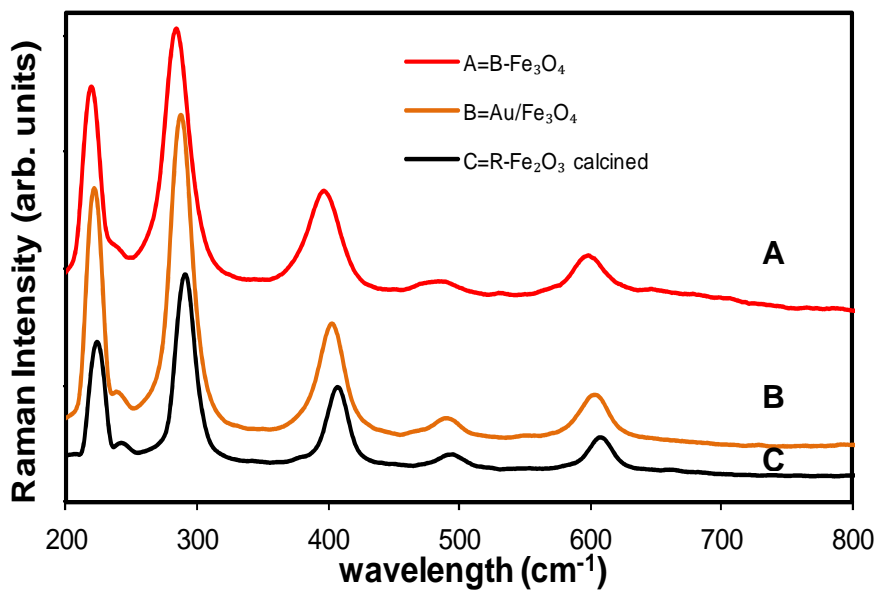
Figure 2.4. Raman spectra of iron oxide of, A: correspond to B-Fe$_3$O$_4$, B: presents the spectrum of as prepared Fe$_2$O$_3$, C: presents the spectrum of Au/Fe$_3$O$_4$, and D: corresponds to R-Fe$_2$O$_3$.

Results obtained for FT-IR analysis (vibrational information) of three oxides: B-Fe_3O_4, Au/Fe_3O_4, and $R-Fe_2O_3$ are shown in Figure 2.3. The signature peak of B-Fe_3O_4 appeared at 588 cm^{-1}. The IR signal observed at 3350 cm^{-1} was tentatively assigned to a hydroxyl (-OH group) that is characteristic peak of water absorbed on the surface. The FT-IR spectrum of Au/Fe_3O_4 shows the same bands than B-Fe_3O_4. $R-Fe_2O_3$ nanoparticles exhibited characteristic bands of hematite at 457 cm^{-1}, 532 cm^{-1} and again the broad band of water. Figure 2.4 illustrates typical Raman spectra obtained for oxides prepared. In this figure the presence of hematite ($R-Fe_2O_3$) is shown in the characteristic region of 200-800 cm^{-1}. The main bands observed are located at 225 cm^{-1} and 492 cm^{-1} (symmetric Fe-O stretch) and at 245, 295, 408 and 611 cm^{-1} due to bending vibrations. These results are similar to the ones reported by Legodi and collaborators (Legodi, 2007).

Table 2.1. Summary of relevant properties of Hematite, Magnetite, and Au/Fe_3O_4

Physical properties			Vibrational information		Surface properties		Magnetic properties		
Material	Color	Size (nm)	IR bands (cm^{-1})	Raman Bands (cm^{-1})	BET Surface (m²/g)	Porosity Width (nm)	Magnetization Ms (emu/g)	Coercitivity (G)	Retentivity Mr (emu/g)
Fe_2O_3 as prepared	red	12	470, 534,1461,1650 3997	226, 293, 411, 501, 613	146	0.70	21.42	201.6	4.48
Fe_2O_3 calcined	red	64	552, 458	225, 291, 408, 611	50	0.73	0.6364	2524	0.22
Fe_3O_4	black	9	566	219, 284,397, 600	9	1.32	53.40	267.61	8.00
Au/Fe_3O_4	black	21	580	221, 287, 405, 492, 604	19	0.85	58.10	499.48	8.81

Magnetic properties such as saturation magnetization (Ms), coercivity (Hc) and remnant magnetization (Mr) are also displayed in Table 1 for each oxide prepared.

17

Figure 2.5 shows the magnetization curve of three oxides prepared. The results of magnetization for B-Fe_3O_4 and black Au/Fe_3O_4 oxide were 53.4 and 58.0 emu/g, respectively. This similarity in the results indicates that the presence of gold on the oxide leads to retention of magnetic properties in the new material. Otherwise, as-prepared and calcined R-Fe_2O_3 exhibits low results for magnetization. The weak ferromagnetic behavior of R-Fe_2O_3 is manifested in the hysteresis cycle presented in Figure 2.5C. The hysteresis loop did not reach saturation up to the maximum field employed in the measurement system. The remnant of magnetization was determined to be 0.22 emu/g for calcined R-Fe_2O_3 and 4.48 emu/g in as-prepared R-Fe_2O_3. The results are in good agreement with published results on hematite particles of different geometries (Plaza, 2001). The super paramagnetic behaviors of black oxide and black Au/Fe_3O_4 make the photocatalyst powder easy to separate using a magnet or an applied magnetic field.
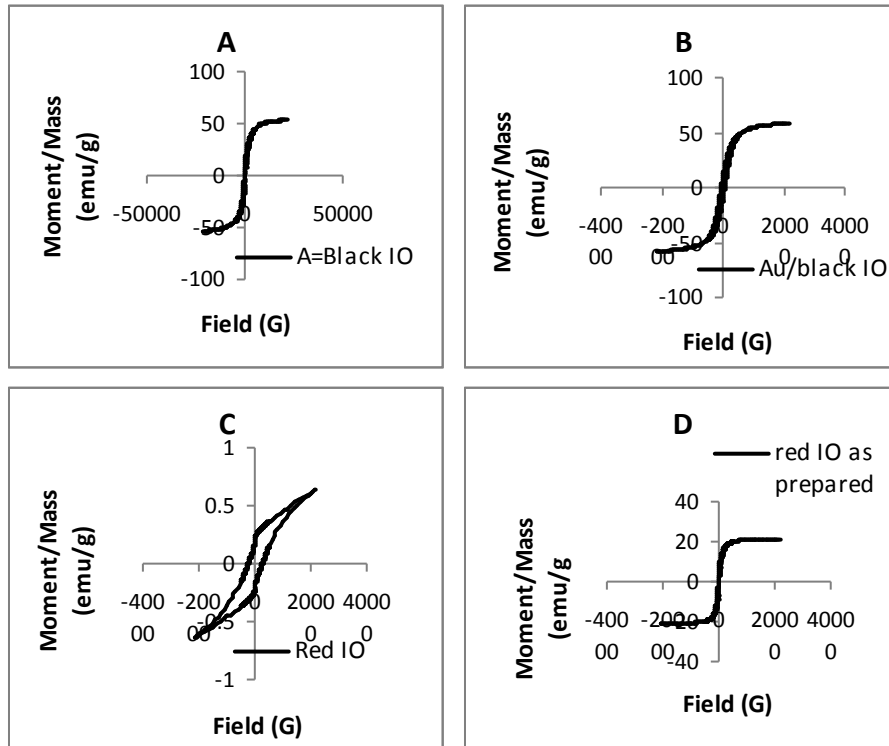
Figure 2.5. Magnetization curves of iron oxide prepared of, A: B-Fe$_3$O$_4$, B: AuFe$_3$O$_4$, C: R- Fe$_2$O$_3$, and D: as prepared R-Fe$_2$O$_3$.
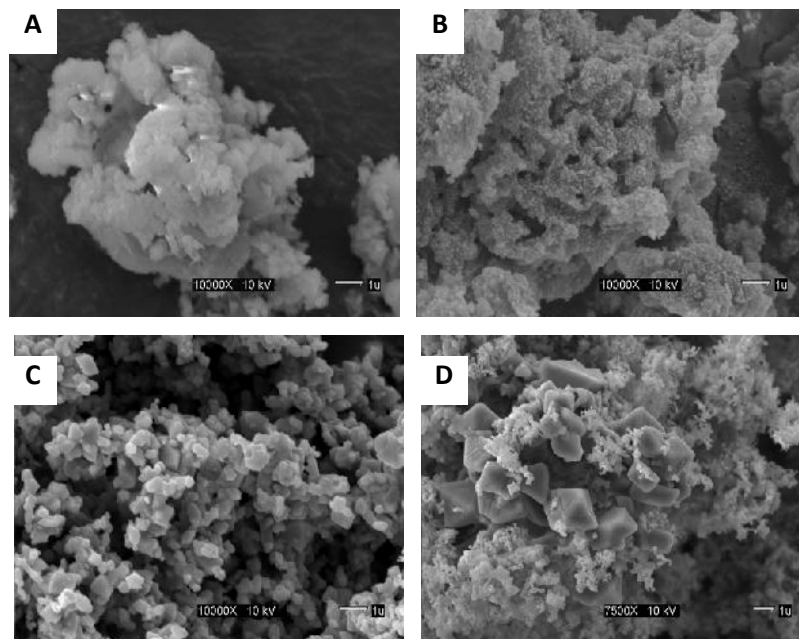
Figure 2.6. SEM photographs of particles obtained using the hydrothermal method. A: R-Fe$_2$O$_3$ as-prepared, B: R- Fe$_2$O$_3$ calcined at 500 ÊC, C: B-Fe$_3$O$_4$ calcined at 500 ÊC, and D: Au/ Fe$_3$O$_4$ calcined at 500 ÊC.

SEM images of hydrothermally prepared particles are shown in Figure 2.6. In the image of as-prepared R-Fe$_2$O$_3$ (Figure 2.6A) agglomeration of nanoparticles can be noticed. The particle size is below 100 nm. The particle size of the amorphous powders hydrothermally synthesized and calcined at 500 °C was about 250 nm. As the hydrothermal temperature was raised above 500 °C, the particle size increased with increasing temperature. Figure 2.6D shows the SEM images of the B-Fe$_3$O$_4$ oxide with different morphologies. Some particles are spherical and of nanometer size. In the images of Au/Fe$_3$O$_4$ (Figure 2.6D) small spherical particles were found on the magnetite surface. The surface in this image was smooth which again indicates the high quality of the nanoparticles, similar to magnetite octahedrons prepared (Mao, 2006). TEM images were collected. The results are shown in Figure 2.7
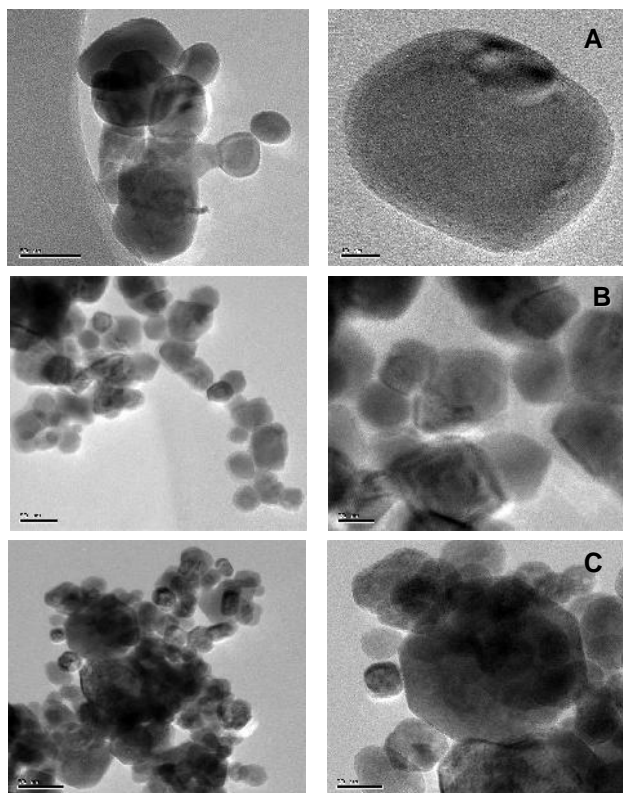
Figure 2.7. TEM images of particles obtained using the hydrothermal method. A: R-Fe$_2$O$_3$ calcined at 500 ͡C, B: B-Fe$_3$O$_4$ calcined at 500 ͡C, C: Au/Fe$_3$O$_4$ calcined at 500 ͡C.
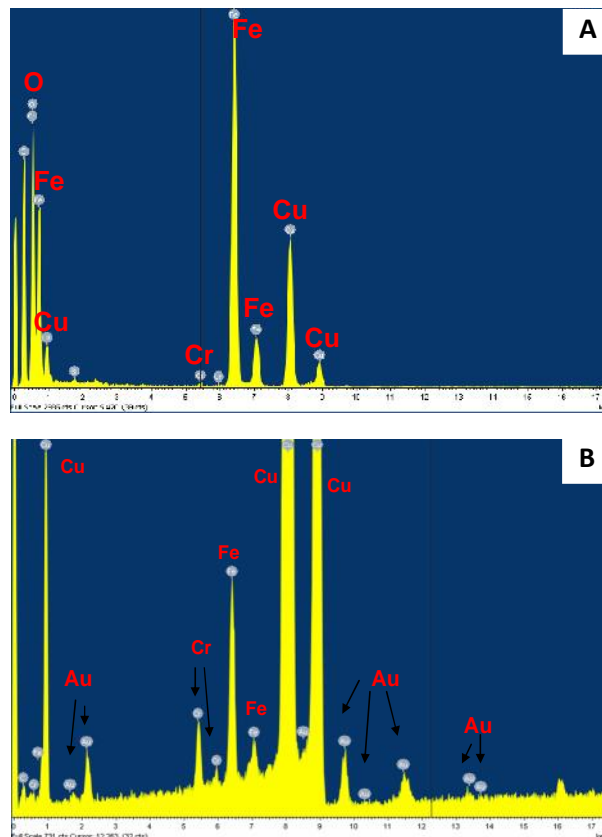
Figure 2.8. EDS spectra of, A: B-Fe$_3$O$_4$, and B: Au/Fe$_3$O$_4$.

Figure 2.7A shows an image of hematite (R-Fe$_2$O$_3$). The particles are highly crystalline and of spherical form. The range in size of spherical particles is between 25 and 60 nm. TEM images of B-Fe$_3$O$_4$ (magnetite) in figure 2.7B show prisms and spheres. Tiny crystals with size of about 50 nm are observed. Crystalline planes are present and dislocations are displayed in some crystals. Images of Au/ Fe$_3$O$_4$ are shown in Figure 2.7C. Newly, crystalline planes are observed, the particles present approximately 70 nm in size. Spherical particles on the bigger crystals are also found with particle size between 15 and 25 nm. Elemental analysis was carried out to corroborate the presence of gold in the particles. The analysis was performed in the TEM equipment, and the results are shown in Figure 2.8 (EDS spectrum). Figure 2.8A

shows the elemental analysis of B-Fe₃O₄;. Fe, O, Cu, and Cr were detected. The presence of traces of chromium is possibly due a cross contamination of the sample during the preparation. Figure 2.8B shows the results for Au/Fe₃O₄ oxide. The presence of Au, Fe, O and Cr was established. Elemental analysis confirmed the gold content in the sample.

To evaluate the photocatalytic capacity of the oxides obtained, solutions of MB, ONF, and TNT were and compared to nano-powder in the presence of UV illumination. Figure 2.9 shows decay of the concentration of MB catalyzed by iron oxide. Each experiment included a set of control when the analyte is place under UV light without catalyst. Solutions were placed in a dark box to eliminate contributions from degradation from ambient light. In the case of control runs, no discoloration was observed. Maximum absorbance by MB solutions was monitored at 663 nm. The absorbance rapidly decreased with irradiation time for solutions in contact with B-Fe₃O₄ and Au/Fe₃O₄.
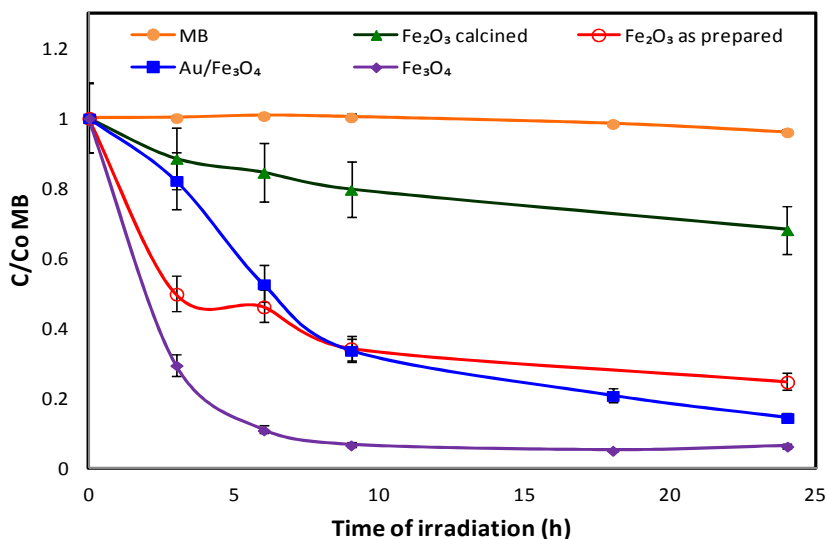
Figure 2.9. Degradation of MB under $UV_{254 nm}$ in photolysis and photocatalysis, : Neat MB in water, : mixture of MB with calcined Fe₂O₃, : mixture of MB with R-Fe₂O₃ as prepared, : mixture of MB with Au/Fe₃O₄, and : mixture of MB with B-Fe₃O₄.Experimental photocatalytic condition: MB 5.7 mg/L in a ratio of MB:oxide of 1:400.
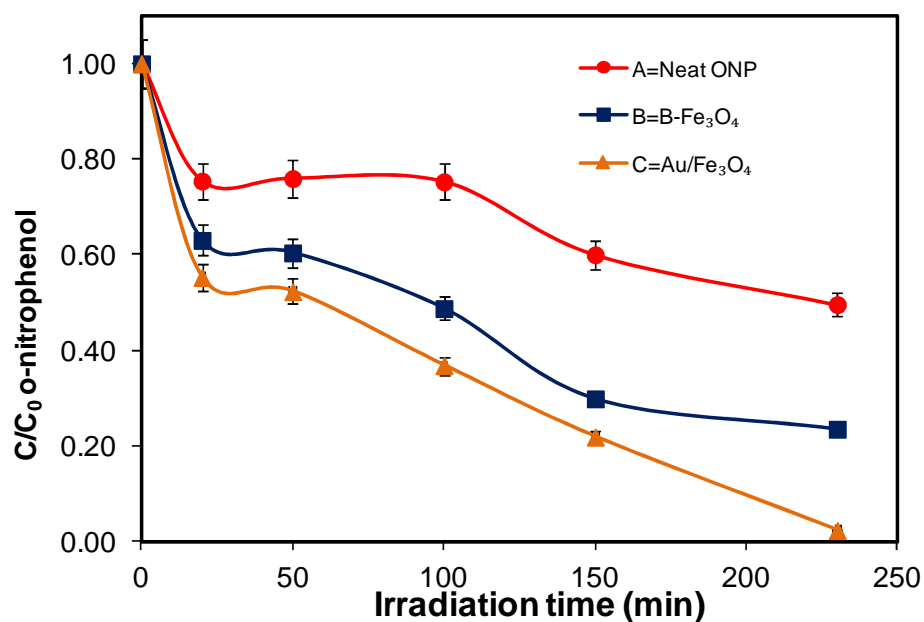
Figure 2.10. Degradation of ONP under UV$_{254\text{ nm}}$ in photolysis and photocatalysis, : Neat ONP in water, : mixture of ONP with R-Fe$_3$O$_4$, and : mixture of ONP with Au/Fe$_3$O$_4$.Experimental photocatalytic condition: ONP 39 mg/L in a ratio of ONP:oxide of 1:400.
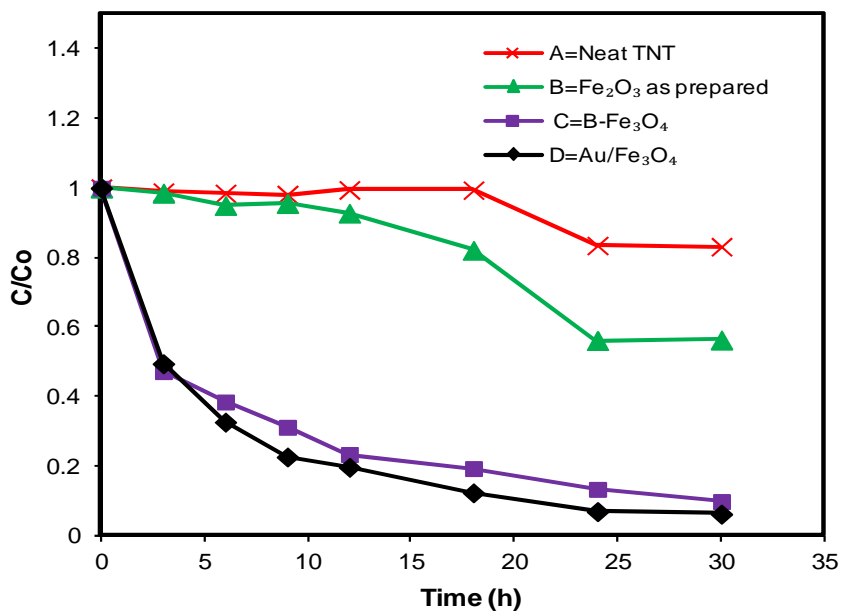
Figure 2.11. Degradation of TNT in photolysis at UV$_{254\text{ nm}}$. Î : Neat TNT in water, : mixture of TNT with calcined Fe$_2$O$_3$, : mixture of TNT with R-Fe$_3$O$_4$, and : mixture of TNT with Au/Fe$_3$O$_4$. Experimental photocatalytic conditions were: TNT 25 mg/L in a ratio of TNT:oxide of 1:400.

To complement the results obtained for MB solutions oxides (B-Fe_3O_4 and Au/Fe_3O_4) that showed best results with MB were added to ONP and TNT solutions to verify the photocatalytic activity. Nitroaromatic compounds are pollutants derived from Industrial synthesis of munitions. In 1998 the Environmental Protection Agency (EPA) classified the TNT as a priority EPA pollutant (US EPA, 1988). The results for degradation of nitrocompounds are presented in Figures 2.10 and 2.11. Synthesized oxides exhibited photocatalytic activity and promise to be useful as photocatalyst at large scale degrading contaminants present in water. The doped oxide showed the best results at 240 minutes of irradiation time. This oxide degraded about 95% of ONP in aqueous solution. For TNT at 9 h of UV treatment the degree of degradation found was about 80% for Au/ Fe_3O_4.

2.4 Conclusions

Iron oxides: magnetite and hematite were prepared. The type of oxide obtained depended on the environment to which the oxides were exposed during their calcinations. Heating processes with open air flow environment result a less oxidized nanopowder (hematite). On the other hand, a closed end environment without air flow, a higher oxidation form of the nanopowder was obtained. All oxides were characterized to determine the principal phase present.

XRD results show that R-Fe_2O_3 is present in the hematite form. Magnetite characteristic bands are the dominant XRD signatures. Magnetic and vibrational properties and pore and particle size were determined.

In the evaluation of catalytic activity using MB, degradation was appreciated at approximately 6 h of exposure to UV light. Similarly, a decrease in more than 90% in the

concentration of ONP was observed. This indicates that B-Fe$_3$O$_4$ and Au/Fe$_3$O$_4$ could be used as photocatalyst agents to remove contaminants in water. These oxides could be easily removed from water using their magnetic properties.

Acknowledgments

References

Ao, Y., Xu, J., Shen, X., Fu, D., and Yuan, C. (2008), 'Magnetically separable composite photocatalyst with enhanced photocatalytic activity', *J. Hazard. Mater.,* 160 (2–3), 295-300.

Baez, B., Florian, V., Hernandez-Rivera, S., Cabanzo, A., Correa, S., Irrazabal, M., Briano, J.G., Castro, M. (2006), 'Detection of chemical signatures from TNT buried in sand at various ambient conditions: phase II.', *Detection and Remediation Technologies for Mines and Minelike Targets XI* (Orlando: SPIE International Society Optical Engineering), 62171M.

Bahnemann, D. (2004), 'Photocatalytic water treatment: solar energy applications', *Solar Energy,* 77 (5), 445-459.

Charles, S.W. (1987), 'Some applications of magnetic fluids— use as an ink and in microwave systems', *Magn. Magn. Mater.* 65 (2–3), 350-358.

Corot, C., Robert, P., Idée, J.-M., and Port, M. (2006), 'Recent advances in iron oxide nanocrystal technology for medical imaging', *Adv. Drug Delivery Rev.,* 58 (14), 1471-1504.

Correa-Torres, S.N. (2011), 'Absorption of Toxic Nitroaromatics Compounds from Culture Media and Soil using Plants as Phytoremediation Models', (University of Puerto Rico).

Cruz-Uribe, O., Cheney, D., Rorrer, G. (2007), 'Comparison of TNT removal from seawater by three marine Macroalgae', *Chemosphere,* 67, 1469-1476.

Gimeno, O., Carbajo, M., Beltrán, F.J., and Rivas, F.J. (2005), 'Phenol and substituted phenols AOPs remediation', *J. Hazard. Mater.,* 119 (1–3), 99-108.

Ito, A., Shinkai, M., Honda, H., and Kobayashi, T. (2005), 'Medical application of functionalized magnetic nanoparticles', *J. Biosci. Bioeng.,* 100 (1), 1-11.

Kinoshita, T., Seino, S., Mizukoshi, Y., Nakagawa, T., and Yamamoto, T.A. (2007), 'Functionalization of magnetic gold/iron-oxide composite nanoparticles with oligonucleotides and magnetic separation of specific target', *J. Magn. Magn. Mater.,* 311 (1), 255-258.

Kormann, C., Bahnemann, D.W., and Hoffmann, M.R. (1989), 'Environmental photochemistry: Is iron oxide (hematite) an active photocatalyst? A comparative study: -Fe2O3, ZnO, TiO2', *J. Photochem. Photobiol., A,* 48 (1), 161-169.

Legodi, M.A. and de Waal, D. (2007), 'The preparation of magnetite, goethite, hematite and maghemite of pigment quality from mill scale iron waste', *Dyes Pigm.,* 74 (1), 161-168.

Lei, J., Liu, C., Li, F., Li, X., Zhou, S., Liu, T., Gu, M., and Wu, Q. (2006), 'Photodegradation of orange I in the heterogeneous iron oxide–oxalate complex system under UVA irradiation', *J. Hazard. Mater.,* 137 (2), 1016-1024.

Liu, Q., Zhang, W.-M., Cui, Z.-M., Zhang, B., Wan, L.-J., and Song, W.-G. (2007), 'Aqueous route for mesoporous metal oxides using inorganic metal source and their applications', *Microporous Mesoporous Mater.,* 100 (1–3), 233-240.

Mao, B., Kang, Z., Wang, E., Lian, S., Gao, L., Tian, C., and Wang, C. (2006), 'Synthesis of magnetite octahedrons from iron powders through a mild hydrothermal method', *Mater. Res. Bull.,* 41 (12), 2226-2231.

Marquez, F., Herrera, G., Campo, T., Cotto, M., Duconge, J., Sanz, J., Elizalde, E., Perales, O., and Morant, C. (2012), 'Preparation of hollow magnetite microspheres and their applications as drugs carriers', *Nanoscale Res. Lett.,* 7 (1), 210.

Maver, U., Bele, M., Makovec, D., ampelj, S., Jamnik, J., and Gaberš ek, M. (2009), 'Incorporation and release of drug into/from superparamagnetic iron oxide nanoparticles', *J. Magn. Magn. Mater.,* 321 (19), 3187-3192.

Mürbe, J., Rechtenbach, A., and Töpfer, J. (2008), 'Synthesis and physical characterization of magnetite nanoparticles for biomedical applications', *Mater. Chem. Phys.,* 110 (2–3), 426-433.

Pecharsky, V.K. and Gschneidner Jr, K.A. (2006), 'Advanced magnetocaloric materials: What does the future hold?', *Int. J. Refrig.,* 29 (8), 1239-1249.

Plaza, R.C., Gómez-Lopera, S.A., and Delgado, A.V. (2001), 'Magnetic Properties of Composite Hematite/Yttrium Oxide Colloidal Particles', *J. Colloid Interface Sci.,* 240 (1), 48-53.

Ravaud, R., Lemarquand, G., and Lemarquand, V. (2010), 'Mechanical properties of ferrofluid applications: Centering effect and capacity of a seal', *Tribol. Int.,* 43 (1–2), 76-82.

Snowball, I.F. (1997), 'The detection of single-domain greigite (Fe3S4) using rotational remanent magnetization (RRM) and the effective gyro field (Bg): mineral magnetic and palaeomagnetic applications', *Geophys. J. Int.,* 130 (3), 704-716.

Souza, F.L., Lopes, K.P., Nascente, P.A.P., and Leite, E.R. (2009), 'Nanostructured hematite thin films produced by spin-coating deposition solution: Application in water splitting', *Sol. Energy Mater. Sol. Cells,* 93 (3), 362-368.

Spratt, G. and Hobby, P. (2001), 'Magnetic Recording Media: Advanced', in Editors-in-Chief: , K.H.J.B., Robert, W.C., Merton, C.F., Bernard, I., Edward, J.K., Subhash, M., and Patrick, V. (eds.), *Encyclopedia of Materials: Science and Technology (Second Edition)* (Oxford: Elsevier), 4893-4897.

Stratmann, M. (1990), 'The Atmospheric Corrosion of Iron — A Discussion of the Physico-Chemical Fundamentals of this Omnipresent Corrosion Process Invited Review', *Ber. Bunsen Ges. Phys. Chem.,* 94 (6), 626-639.

Wang, Y., Liu, C.S., Li, F.B., Liu, C.P., and Liang, J.B. (2009), 'Photodegradation of polycyclic aromatic hydrocarbon pyrene by iron oxide in solid phase', *J. Hazard. Mater.,* 162 (2–3), 716-723.

Yu, B.F., Gao, Q., Zhang, B., Meng, X.Z., and Chen, Z. (2003), 'Review on research of room temperature magnetic refrigeration', *Int. J. Refrig.,* 26 (6), 622-636.

Chapter 3

EVALUATION OF pH AND H_2O_2 EFFECTS ON PHOTOCATALYTIC ACTIVITY OF IRON OXIDE

Abstract

Photocatalytic degradation of TNT, cyclotrimethylenetrinitramine (RDX) and MB was investigated in the presence of aqueous iron oxide (Fe_3O_4) suspensions subject to UV irradiation. Various parameters that play leading roles in the photocatalytic degradation were investigated including pH, irradiation wavelength, and addition of H_2O_2.

Adsorption kinetics data were determined by the change in TNT concentration as a function of irradiation time measured by HPLC chromatography. The results showed a significant dependence pH on the photocatalytic degradation of TNT. Similarly, the effect of the addition of a strong oxidant such as hydrogen peroxide on the increase in TNT degradation was also investigated.

Keywords: RDX, photocatalyst, degradation, TNT, irradiation

3.1 Introduction

New technologies have been developed to eliminate pollutants present in water. Heterogeneous photocatalytic degradation is a new technique that has the potential to complete mineralization of organic pollutants. Among the advantages of photocatalysis are a relatively fast process, low costs and use of renewable resources such as sunlight (Wang, 2000).

Some investigators have proposed that photocatalytic reactions are zero- or first-order kinetics processes. These statements are applicable for limited conditions where the solute concentration is inadequately low. In most kinetic studies, the kinetic profiles are usually show that the oxidation rates increase with irradiation time until the rate becomes zero. The Langmuir-Hinshelwood (L-H) kinetic model has been used to explain the mineralization process kinetics and to assume automatically that reactions take place at the surface of the catalyst particle, without any corroborating independent evidence to support this (Chong, 2010).

The L-H model was initially developed to quantitatively describe gaseous–solid reactions (Butt, 1970). However, the model was also employed to describe solid–liquid reactions (Ollis, 1985). In this model, the reaction rate *(r)* is proportional to the surface fraction covered by the substrate *( )* (Laoufi, 2008).

$$r = -\frac{dC}{dt} = k_{r}\,\text{"}$$

3. 1

Considering Langmuir's equation

$$\text{"} = \frac{KC}{(1 + KC)} \qquad \qquad \textbf{3.2}$$

$$r = -\frac{dC}{dt} = k_{r''\ x} = \frac{k_r KC}{1 + KC} \qquad \qquad \textbf{3.3}$$

The equation can be simplified to a pseudo-first order equation if KC<<1

$$\ln \frac{Co}{C} = k_r Kt = k't \qquad \qquad \textbf{3.4}$$

In these relationships C_0 is the initial concentration, C the concentration at time t, K is the constant of adsorption equilibrium of L-H or the Langmuir constant, k_r the reaction rate constant, and k_a is the adsorption constant. A plot of $\ln\{C_0/C\}$ vs. time is a straight line, the slope of which upon linear regression equals the apparent first-order rate constant k' (Laoufi, 2008).

The photocatalytic systems are highly dependent on a number of the operation parameters that govern the kinetics of photo-mineralization and photo-disinfection. The principal parameters are: photocatalysts loading, pH, temperature, and light wavelength. In works previously published, pH is by far the major factor influencing the rate of degradation of compounds such as chlorophenol (Laoufi, 2008) in the photocatalytic process. For other organic compounds (Piscopo, 2001) studies of operational variables were reported without a conclusion about pH effect. When TiO_2 was used as photocatalyst the reaction was faster by lowering the pH, and was found to be of apparent first-order following Langmuir–Hinshelwood model (Wang, 2000).

Another important parameter studied in the photocatalytic degradation of organic pollutants was the effect of hydroxyl radicals •OH. Therefore, electron acceptors have

been used to enhance the degradation rates since they generate •OH radicals (Sun, 1996). The addition of small concentrations of hydrogen peroxide (H_2O_2), to photocatalytic systems may enhance the process efficiency. At higher concentrations, hydrogen peroxide was found to have an inhibiting effect on photocatalytic reactions. Hydrogen peroxide can accelerate the reaction rate by capturing electrons, reacting with excess oxygen, or absorbing light with wavelengths shorter than 310 nm. In all situations described •OH radicals, which are critical for the process due to their high reactivity, mediated (Smida, 2012).

In the present work, the effects of various experimental parameters, such as pH, addition of H_2O_2 on the photocatalytic degradation of TNT and RDX were examined. These are organic nitrocompounds used for military purposes in explosive events. The objective of the present work was to evaluate the effect H_2O_2 and pH on the photocatalytic degradation of them. The change in concentration of TNT and RDX containing solutions was monitored at various pH and H_2O_2 dosages.

3.2 Materials and Methods

3.2.1 *Synthesis of metal oxides nanoparticles through hydrothermal method*

In a typical synthesis, 2 mmol of $Fe(NO_3)_3 \cdot 9H_2O$ (99.98%, analytical grade, Fisher Scientific International), 1 gram of CTAB (HPLC grade, Sigma-Aldrich Chemicals) and 15 mmol urea (HPLC grade, Sigma-Aldrich Chemicals) were dissolved in 35 mL of water. The solutions were placed in a vacuum oven at 70 °C/16 Pa for 24 h. The products were recovered by several cycles of centrifugation (8000 rpm/5 min), rinsed with ddH$_2$O, and finally charred at 550 °C to remove organic residues (Liu, 2007).

31

In the synthesis of catalyst Au/Fe_2O_3, the same procedure was used but the water was replaced by a gold solution ($HAuCl_4$, HPLC grade, Sigma-Aldrich Chemicals) at 1% w/w.

3.2.2 *Photocatalytic evaluation of nano-sized oxides in contaminated water.*

To evaluate photo catalytic activity of nano-sized oxides, using selected pollutants such as TNT and RDX a systematic study was conducted via UV irradiation. Fixed amounts of nano oxide were added to aqueous solutions of TNT (Chem. Service Inc., West Chester, PA: crystals, 98%, 30% water) and RDX (ChemService, Inc., West Chester, PA). The suspensions were then irradiated by ultraviolet (UV) light with at 254 nm and an intensity of 600 mW/cm^2 measured by a UVA radiation meter. At given time intervals, aliquots from suspension were obtained and immediately centrifuged at 8500 rpm. The supernatant liquid was analyzed using an Agilent 8453 UV-Visible spectrometer. During irradiation, the solutions were stirred to keep the homogenous suspensions. The temperature used during the procedure was 25 °C.

The quantitative analysis of nitrocompounds was carried out using an Agilent HPLC with a UV detector diode array. The column used was a C_{18}. In order to remove the catalyst before analysis, all aqueous samples were filtered.

3.2.3 *Effect of pH of the solution*

The pH of solutions were measured using 8682 digital pH meter (AZ Instrument Corp., Taiwan, China) and adjusted with HCl (0.1 M) or NaOH (0.1 M). All experiments were conducted at 25 °C. The amount of photocatalysts added followed the ratio 1:400

(iron oxide: volume of TNT solution). The same procedure as described in section **3.2.2** was followed.

3.2.4 *Effect of addition of H_2O_2*

Experiments were carried out to examine the effects of H_2O_2 on the photocatalytic degradation of TNT. The degradation procedure used was the same described in the section **3.2.2**, but the corresponding volume of H_2O_2 for the desired molar ratio was added immediately before starting the lamp. This was taken as the initial time for reactions under light. The initial concentration of TNT was fixed at 15 ppm and the iron oxide dosage was 2.5 g/L.

3.3 **Results and Discussion**

3.3.1 *Evaluation of adsorption activity of iron oxide in contaminated water*

Magnetic particles can be used to adsorb contaminants from aqueous or gaseous effluents and after the adsorption is carried out, the adsorbent can be separated from the medium by a simple magnetic process. In this experiment TNT and RDX were used as water contaminants to test adsorptive capacity of iron oxide prepared. Calibration runs were prepared to quantify the TNT and RDX present in water before and after of the adsorption process. Figure 3.1 and 3.2 display the calibration curve to quantify TNT and RDX in aqueous solution.

Calibration curve TNT

y = 21.264x - 6.1696
R² = 0.9999
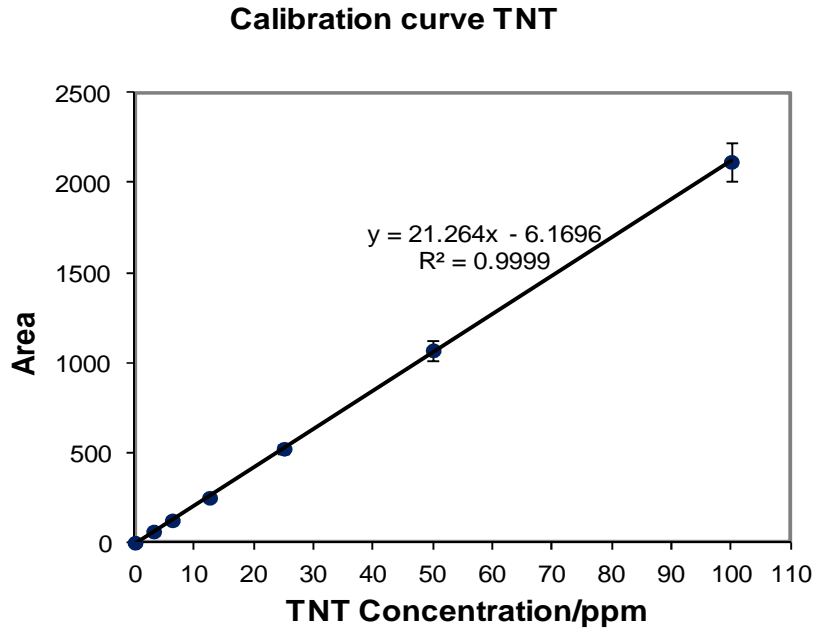
Figure 3.1 UV calibration curve for TNT in water in the range of concentration of 0 at 100 ppm.

Calibration curve of RDX

y = 6.0216x - 0.1816
R^2 = 0.9995
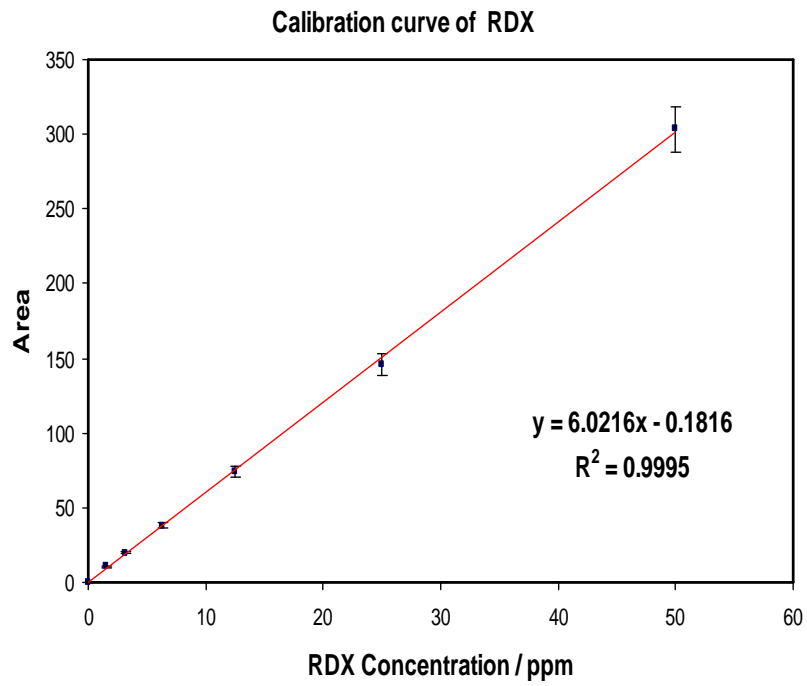
Figure 3.2 UV calibration curve for RDX in water in the range of concentration of 0 at 50 ppm.

Adsorption is a unit operation in which dissolved constituents was removed from the solvent (water) by inter-phase transfer to the surfaces of an adsorbent particle (H. Y. Chen, 1995; B. Chen, 2011; Oliveira, 2003). Adsorption by activated carbon (AC) is most often used to remove organic contaminants (Derylo-Marczewska, 2011; Matsui, 2003; Yin, 2007). Many studies have used AC to remove also inorganic contaminants such as lead (Depci, 2012; Zhang, 2005), mercury (Gomez-Serrano, 1998; Zabihi, 2010) and chlorine (MacDonald, 2000; Martin, 1990) of water. An adsorption isotherm is used to characterize the equilibrium between the amount of adsorbate (contaminant) that accumulates on the adsorbent and the concentration of the dissolved adsorbate. The Langmuir adsorption isotherm and the Freundlich isotherm are two common isotherms used to describe equilibrium involved. Langmuir's isotherm describing the adsorption of an adsorbate onto the surface of the adsorbent requires three assumptions:

- The surface of the adsorbent is in contact with a solution containing an absorbate that which is strongly attracted to the surface.

- There are only an amount specific of number of sites on the surface, where the solute molecules can be adsorbed.

- The adsorption represents the attachment of only one layer of molecules on the surface, producing a monolayer adsorption.

- The Langmuir isotherm is described by:

$$qe = \frac{QokCe}{KCe+1}$$ **3. 1**

where q_e is the amount adsorbed per mass unit of adsorbent (wt/wt), Q_o and k are empirical constants, and C_e is the equilibrium concentration of adsorbate in solution

after adsorption. The constants Q_o and k can be determined by plotting C_e/q_e vs. C_e and rewriting equation (3.5) as:

$$\frac{Ce}{qe} = \frac{1}{Qok} + \frac{1}{Qo}Ce \qquad\qquad \textbf{3. 2}$$

However, an empirical equation describes the Freundlich isotherm and typically proves to be a better relation. For the Freundlich isotherm, adsorption is described by:

$$qe = K_f Ce^{1/n} \qquad\qquad \textbf{3. 3}$$

Where K_F and n are constants. Rewriting the equation as:

$$Log(qe) = LogK_f + \frac{1}{n}LogCe \qquad\qquad \textbf{3. 4}$$

Plotting log{q_e} vs. log{C_e} allows the determination of K_f and $1/n$.

Adsorption of TNT and RDX on Fe_3O_4
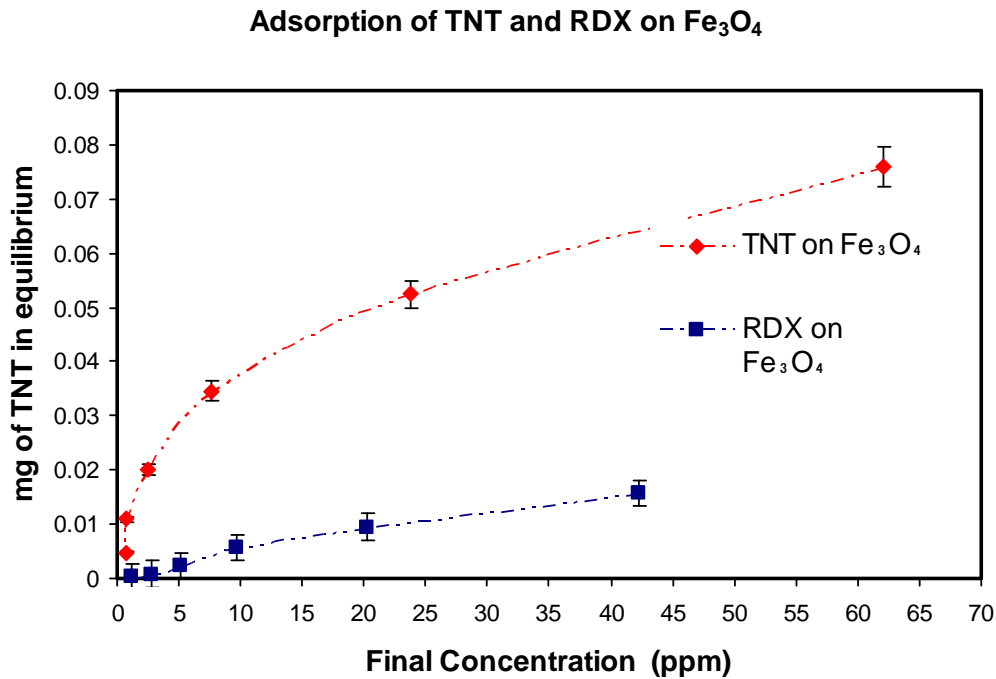
Figure 3.3 Equilibrium isotherms gathered at 28 ± 1 °C for adsorption of TNT or RDX onto iron oxide.

36

The adsorption isotherms are shown in Figure 3.3. It can be observed that the adsorption capacity increases in the order of RDX < TNT. Adsorption isotherm for activated carbon (AC) was carried out. The results were compared to those of iron oxide. TNT was completely adsorbed in the low concentration region and at high concentrations its adsorption was constant (Figure 3.5).

Figures 3.4 and 3.5 show the results of the analyses of the data in terms of adsorption model representing the behavior of TNT solution on iron oxide. The results show that the adsorption of TNT was more closely aligned the Langmuir model (R^2 = 0.998). Fitting the data to the Freundlich model resulted in more modest statistical description of the adsorption process (R^2 = 0.989). The basic premise upon for Langmuir isotherm is that TNT is absorbed by iron oxide at specific locations, so that when a TNT molecule occupies an active site, this site is saturated and it is not possible continue the adsorption process. The linear fit of the adsorption data that is shown in Figure 3.4 is *C/qe = O.08 (C_{eq}) + 5.2818* (with a coefficient of determination of R^2 = 0.998, $1/Q_0$ = 0.08 (Q = 12.5) and K = 0.015).

Lagmuir isotherm of adsorption of TNT on Fe₃O₄

$$y = 0.08x + 5.2818$$
$$R^2 = 0.998$$
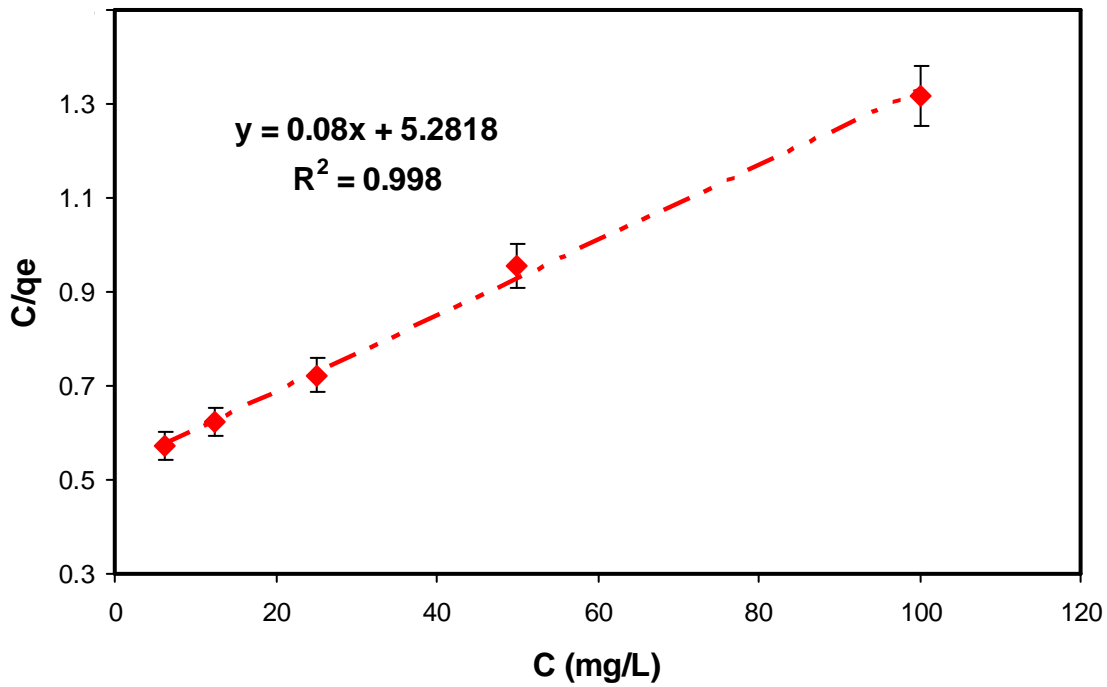
Figure 3.4. Langmuir isotherm model for the adsorption of TNT onto iron oxide.

Freundlich Isotherm of Adsorption of TNT on Fe₃O₄

$$y = 0.6984x + 0.5194$$
$$R^2 = 0.9887$$
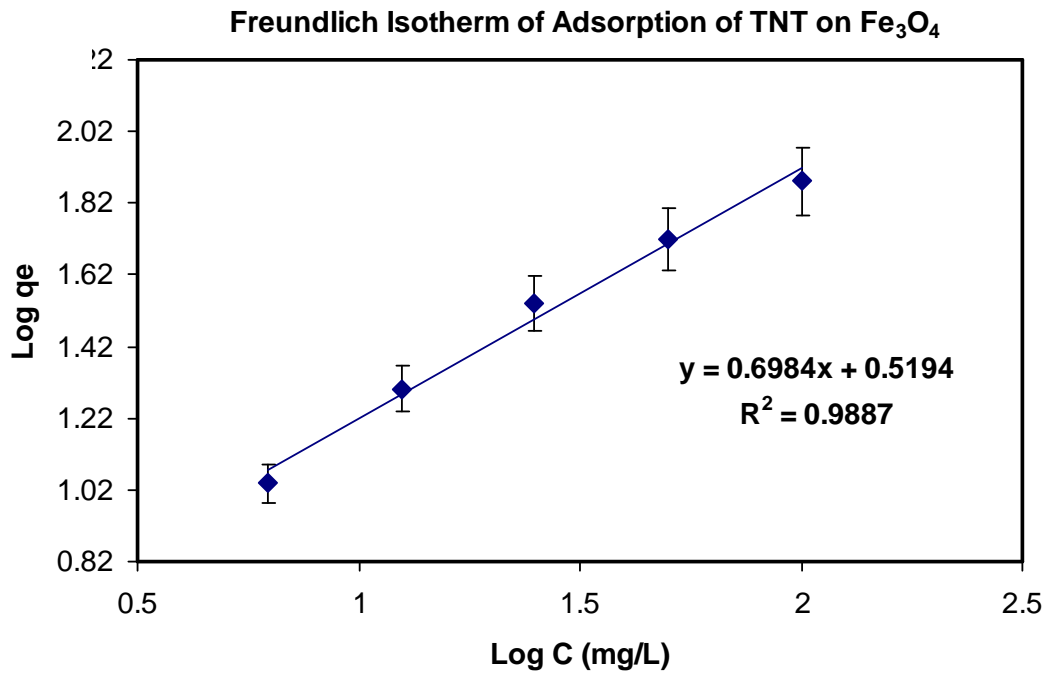
Figure 3. 5. Freundlich isotherm model for the adsorption of TNT onto iron oxide.

3.3.2 *Evaluation of photocatalytic activity of nano-sized oxides in RDX aqueous solution at different irradiation wavelengths*

A comparative study was carried out about on influence of the source in the photodegradation process of RDX in the presence of Fe_3O_4 as catalyst. Three wavelengths were used to degrade aqueous RDX under UV irradiation. Figure 3.6 shows the results of irradiating aqueous solutions of RDX. A UV laser was used as radiation source. The wavelength of the source was 240 nm. The kinetics of degradation of RDX when the solution is in contact with the oxide under UV irradiation and when the net solution of RDX is placed only under irradiation light is shown in Figure 3.6. The results show the solutions containing the explosive are degraded under the influence of the laser action only when they contain iron oxide.
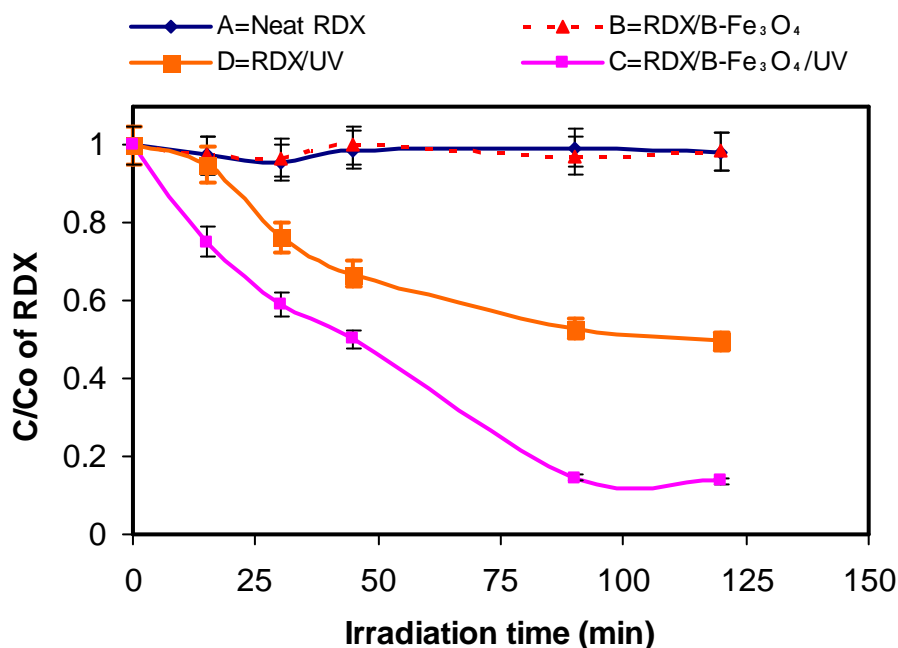
Figure 3.6. UV photodegradation of aqueous RDX solutions using iron oxide as catalyst. UV source was used at 240 nm. Samples were stirred while irradiated.

.

The effect of RDX concentration with Fe_3O_4 without the presence of UV light can be observed. RDX is not degraded without the presence of oxide. Same results were observed when the source of UV light was of 254 nm. Figure 3.7 displays the same behavior. In this experiment the explosive was degraded in the RDX-oxide mixture irradiated at 254 nm. Control batches were added to verify that the decrease in RDX concentration can be attributed to the photocatalytic properties of magnetite. The control batches were RDX solution without magnetite and RDX with magnetite without UV irradiation. In these last two the concentrations remaining unchanged.

Two different sources of radiation were used in the experiments. For 240 nm a dye laser system (Syrah, Newport-Spectra Physics) pumped by a pulsed diode laser system was used. The dye laser was frequency doubled to 240 nm. For 254/365 nm a UV lamp cabinet model C-70 (UVP) with 15 W for short wave (254 nm) and long wave (365 nm). When laser source was used, the photodegradation was carried out very fast.
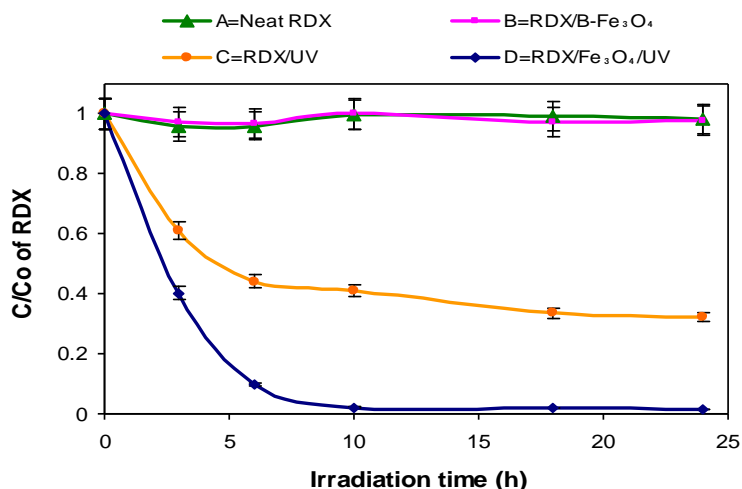
Figure 3. 7 UV photodegradation of aqueous RDX solutions using iron oxide as catalyst. A UV lamp chamber was used at 254 nm. Samples were stirred while irradiated.
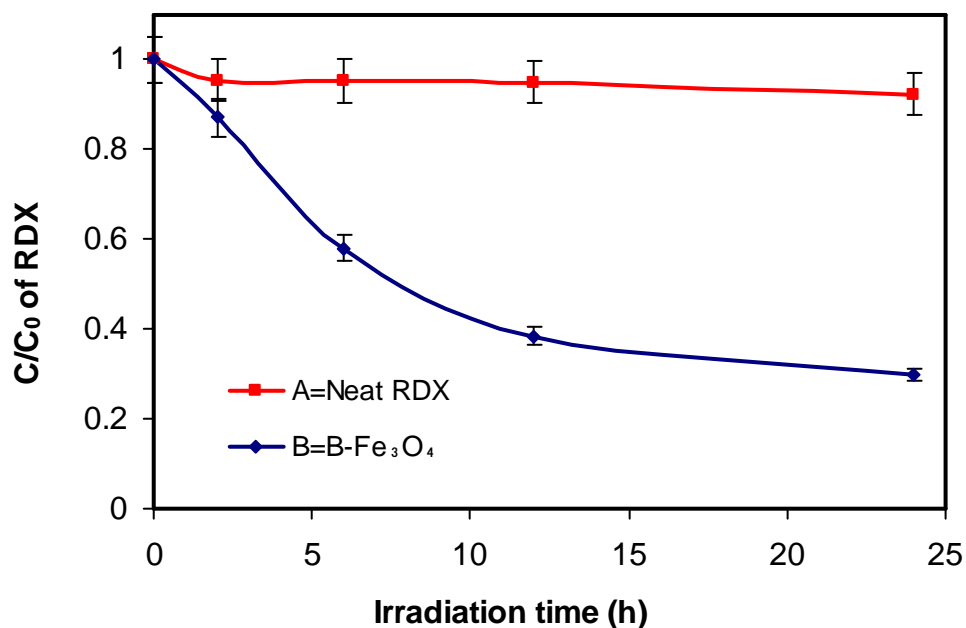
Figure 3.8. UV photodegradation of aqueous RDX solution using Fe_3O_4. A laser was used as source at 365 nm.

Figure 3.8 shows how the concentration of RDX is constant when was irradiated in the presence of UV light without addition of photocatalyst. Moreover, the solutions that contained RDX in the presence of iron oxide showed decrease in concentration with increasing irradiation time. These results are very important because the sunlight passes through the atmosphere, all UVC and approximately 90% of UVB radiation is absorbed by ozone, water vapor, oxygen and carbon dioxide. However, UVA radiation is less affected by the atmosphere. Therefore, the UV radiation reaching the Earth's surface is largely composed of UVA with a small UVB component (Robyn Lucas, 2006). Perchet et al. in 2009 studied the degradation of nitrate compounds contained in wastewater by using a photocatalytic treatment (Perchet, 2009). The method used by the authors involved degradation of nitrophenols by TiO_2 treatment for 8 h, which contrasts with 78 days necessary for liquid anaerobic bioremediation assays. However,

RDX and particularly HMX appeared more resistant to TiO_2 photocatalytic treatment. In the results presented in Figure 3.8 it is observed that the catalyst used (magnetite) showed better results. In summary, photocatalysis of RDX at 365 nm led to rapid decomposition in the presence of Fe_3O_4, but reactions at shorter wavelengths (240 and 254nm) resulted in photodegration of RDX with or without magnetite in contrast with the reaction at longer wavelengths (365 nm), which took place only in the presence of the photocatalyst.

3.3.3 Effect of pH on photocatalytic activity of nano-sized oxides

The effect of the pH of the solution on the photochemical degradation process was also analyzed in this study. The pH of the solution was changed to acid or basic at constant concentration of iron oxide and aqueous solution of TNT. Figure 3.9 shows how the pH affects the degradation process. The analysis was carried out for 3 h. At this time, the optimal pH value was 9, where about 46% of TNT was degraded, when $AuFe_3O_4$ was used as photocatalyst. At acid and neutral pH values, the reaction was clearly less efficient, obtaining lower photodegradation yields.

The degradation of TNT increased on increasing pH of the medium. The explanation for this effect is in an enhanced of number of OH- ions and as consequence increase the •OH radicals. Ameta et al. (2012), studied the pH effect of solution when cooper/iron oxide was used. The range of pH studied was 6.5 – 10.0. They found maximum rates of degradation at pH=9 and decrease of degradation at pH > 9 (Ameta, 2012).
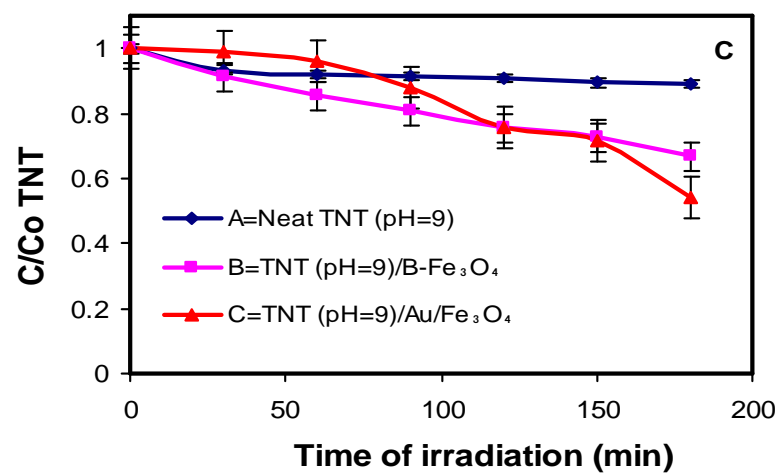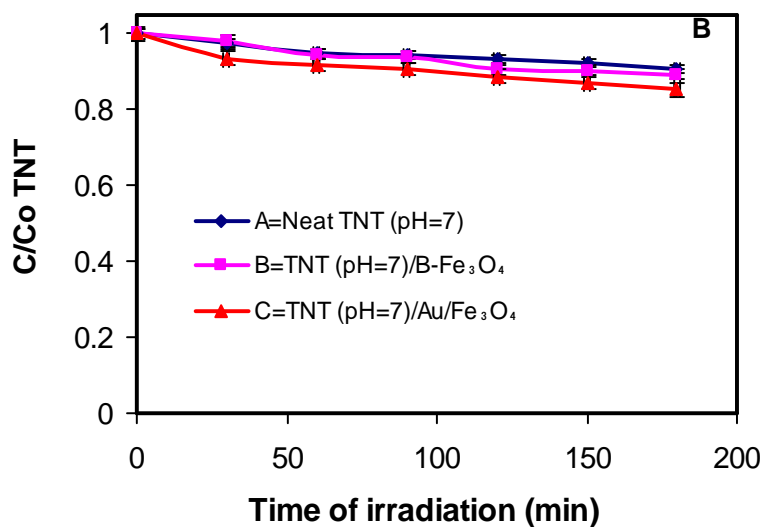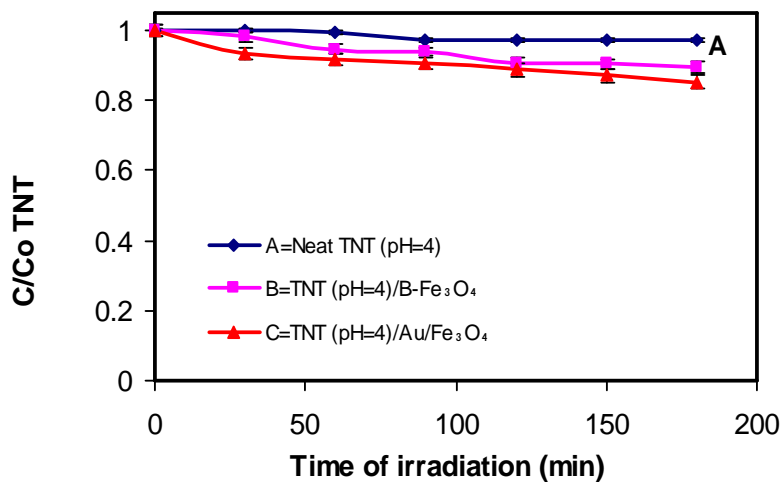
Figure 3. 9. Effect of pH of the reaction mixture on the heterogeneous photocatalysis of TNT. Fe_3O_4 and $AuFe_3O_4$ were used as catalyst. The values of pH studied were 4, 7 and 9: A: TNT / photocatalyst at pH=4; B: TNT / photocatalyst at pH=7; C: TNT / photocatalyst at pH=9.

3.3.4 Effect of addition of H_2O_2

Some substances may affect the efficiency of photodegradation processes. The reaction may be accelerate or inhibit the mineralization rate of the contaminant. One possible reason for degradation inhibition is related to the adsorption of other substances present in the samples (ions) on the catalyst, competing with the adsorption of the contaminant, particularly when they promote pair recombination.
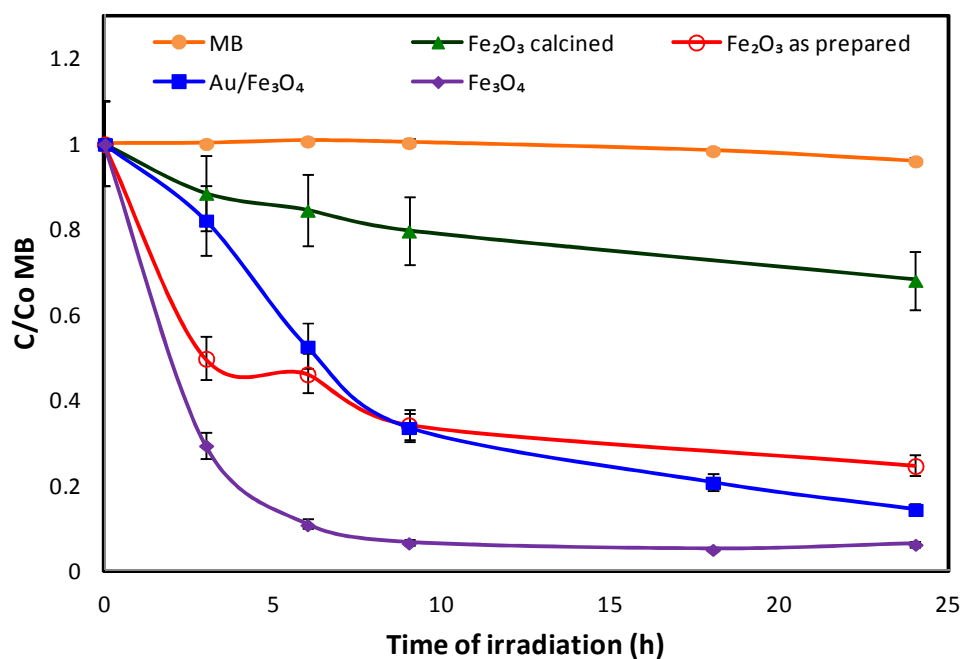
Figure 3.10. Photodegradation of MB using a Fe_3O_4/UV system (see Figure 2.9.

Meanwhile, the presence of oxidizing agents is essential for degradation of the contaminant. Involvement in the oxidation reaction could be possible by hollow capturing if the agent is a very effective oxidizing agent to capture the hollow, speeding the process. The addition of another oxidant such as oxygen allows for even greater speed and higher efficiency in the process. Oxygen is employed because it is cheaper

and does not compete with the substrate in the adsorption process. After oxygen, hydrogen peroxide (H_2O_2) is the next oxidizing agent extensively used and investigated. Hydrogen peroxide performs multiple roles in heterogeneous photocatalysis, and in most cases, the process speed increases according to the following sequence: $O_2 <$ $H_2O_2 < (H_2O_2/O_2)$. H_2O_2 is involved in heterogeneous photocatalysis process because it is capable of reacting with both holes and electrons, and both processes generate •OH radicals. Also it can oxidize directly some of the intermediaries, generating additional •OH radicals in the process.

In Figure 3.10 we can see how it affects the discoloration of a solution of MB when treatment used is $Fe_3O_4/H_2O_2/UV$. One can observe that the clearing time is halved by the addition of peroxide. For Fe_3O_4/UV degradation process that typically takes from 12 to 24 h, the degradation time in the presence of H_2O_2 is reduced to 3-5 h as shown in Figure 3.11. In these studies the addition the oxidizing agent hydrogen peroxide (H_2O_2) increased degradation rate process, resulting in a reduction of the reaction time of approximately half.
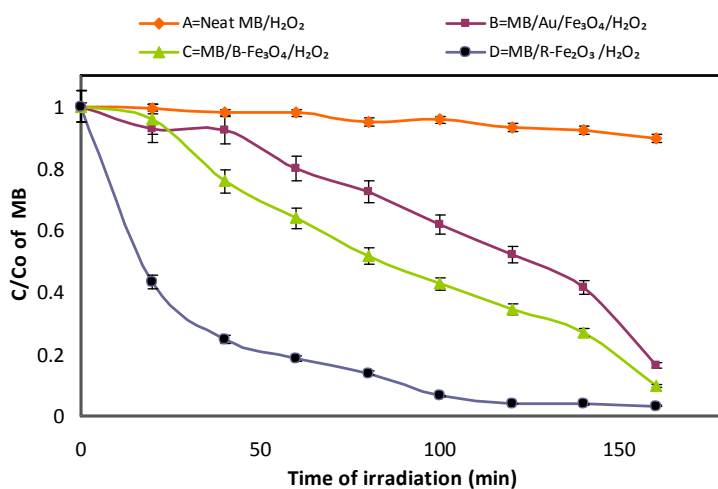
Figure 3.11. Photodegradation of MB using $Fe_3O_4/H_2O_2/UV$ system. : mixture of MB with B- Fe_3O_4. : Neat MB with Au/Fe_3O_4, : mixture of MB with B- Fe_3O_4 , and : mixture of MB with R-Fe_2O_3.

3.4 Conclusions

Degradation of TNT, RDX and MB was conducted mediated by heterogeneous photocatalysis with magnetite. For TNT containing solutions it was found that at 24 h of treatment the nitroaromatic pollutant was photodegraded at the 98% level. For MB at 9 h of irradiation of dye solution the analyte was decolorized up to 93%.

A photodegradation study of highly energetic material RDX was conducted. Solutions containing RDX were irradiated by 240, 254 and 365 nm UV light. The results show that at low wavelengths degradation of RDX without the presence of the photocatalyst took place. At these wavelengths RDX was photosensitive to degradation even without catalytic action. At 365 nm RDX was persistent to degradation and a 70% percent of the explosive was degraded only in the presence of magnetite.

An evaluation of TNT degradation at three pH values (pH = 4, 7, 9) was carried out. The degradation of TNT Increased by increasing pH of the medium. At pH = 9, 46% degradation was obtained at 3 h of exposure to near-UV radiation. The explanation can be attributed to an enhanced number of OH^- ions and as consequence increase in the formation of •OH radicals.

References

Ameta, N.S., Jyoti; Sharma, Sanyogita; Kumar, Sudhish; Punjabi, Pinki B (2012), 'Copper modified iron oxide as heterogeneous photo-Fenton reagent for the degradation of coomasie brilliant blue R-250', *Indian J. Chem., Sect A,* 51 (07), 943-948.

Butt, J.B. (1970), 'Mass transfer in heterogeneous catalysis, C. N. Satterfield, Massachusetts Institute of Technology Press, Cambridge, Mass. (1970). 267 pages', *AIChE J.,* 16 (3), 509-510.

Chen, B. and Huang, W. (2011), 'Effects of compositional heterogeneity and nanoporosity of raw and treated biomass-generated soot on adsorption and absorption of organic contaminants', *Environ. Pollut.,* 159 (2), 550-556.

Chen, H.Y., Zahraa, O., Bouchy, M., Thomas, F., and Bottero, J.Y. (1995), 'Adsorption properties of TiO2 related to the photocatalytic degradation of organic contaminants in water', *J. Photochem. Photobiol., A,* 85 (1–2), 179-186.

Chong, M.N., Jin, B., Chow, C.W.K., and Saint, C. (2010), 'Recent developments in photocatalytic water treatment technology: A review', *Water Res.,* 44 (10), 2997-3027.

Depci, T., Kul, A.R., and Önal, Y. (2012), 'Competitive adsorption of lead and zinc from aqueous solution on activated carbon prepared from Van apple pulp: Study in single- and multi-solute systems', *Chem. Eng. J.,* 200–202 (0), 224-236.

Derylo-Marczewska, A., Buczek, B., and Swiatkowski, A. (2011), 'Effect of oxygen surface groups on adsorption of benzene derivatives from aqueous solutions onto active carbon samples', *Appl. Surf. Sci.,* 257 (22), 9466-9472.

Gomez-Serrano, V., Macias-Garcia, A., Espinosa-Mansilla, A., and Valenzuela-Calahorro, C. (1998), 'Adsorption of Mercury, Cadmium and Lead from Aqueous Solution on Heat-Treated and Sulphurized Activated Carbon', *Water Res.,* 32 (1), 1-4.

Laoufi, N.A., Tasslit, D., and Bentahar, F. (2008), 'The Degradation Of Phenol In Water Solution By TiO$_2$ Photocatalysis In A Helical Reactor ', *Global NEST Journal,* 10 (3), 404-418.

Liu, Q., Zhang, W.-M., Cui, Z.-M., Zhang, B., Wan, L.-J., and Song, W.-G. (2007), 'Aqueous route for mesoporous metal oxides using inorganic metal source and their applications', *Microporous Mesoporous Mater.,* 100 (1–3), 233-240.

MacDonald, J.A.F., Evans, M.J.B., Liang, S., Meech, S.E., Norman, P.R., and Pears, L. (2000), 'Chlorine and oxygen on the carbon surface', *Carbon,* 38 (13), 1825-1830.

Martin, R.J. and Shackleton, R.C. (1990), 'Comparison of two partially activated carbon fabrics for the removal of chlorine and other impurities from water', *Water Res.,* 24 (4), 477-484.

Matsui, Y., Fukuda, Y., Inoue, T., and Matsushita, T. (2003), 'Effect of natural organic matter on powdered activated carbon adsorption of trace contaminants: characteristics and mechanism of competitive adsorption', *Water Res.,* 37 (18), 4413-4424.

Oliveira, L.C.A., Rios, R.V.R.A., Fabris, J.D., Sapag, K., Garg, V.K., and Lago, R.M. (2003), 'Clay–iron oxide magnetic composites for the adsorption of contaminants in water', *Appl. Clay Sci.,* 22 (4), 169-177.

Ollis, D.F. (1985), 'Contaminant degradation in water', *Environ. Sci. Technol.,* 19 (6), 480-484.

Perchet, G., Merlina, G., Revel, J.C., Hafidi, M., Richard, C., and Pinelli, E. (2009), 'Evaluation of a TiO2 photocatalysis treatment on nitrophenols and nitramines contaminated plant wastewaters by solid-phase extraction coupled with ESI HPLC–MS', *J. Hazard. Mater.,* 166 (1), 284-290.

Piscopo, A., Robert, D., and Weber, J.V. (2001), 'Influence of pH and chloride anion on the photocatalytic degradation of organic compounds: Part I. Effect on the benzamide and para-hydroxybenzoic acid in TiO_2 aqueous solution', *Appl. Catal., B,* 35 (2), 117-124.

Robyn Lucas, T.M., Wayne Smith, and Bruce Armstrong (2006) *Solar Ultraviolet Radiation: Global burden of disease from solar ultraviolet radiation* [online text], World Health Organization Public Health and the Environment

Smida, H.B.Y. and Jamoussi, B. (2012), 'Degradation of Nitroaromatic Pollutant by Titanium dioxide/Zinc Phthalocyanine: Study of the Influencing Factors', *IOSR Journal of Applied Chemistry (IOSR-JAC),* 2 (3), 11-17.

Sun, L. and Bolton, J.R. (1996), 'Determination of the Quantum Yield for the Photochemical Generation of Hydroxyl Radicals in TiO_2 Suspensions', *J. Phys. Chem.,* 100 (10), 4127-4134.

Wang, K.-H., Hsieh, Y.-H., Wu, C.-H., and Chang, C.-Y. (2000), 'The pH and anion effects on the heterogeneous photocatalytic degradation of o-methylbenzoic acid in TiO2 aqueous suspension', *Chemosphere,* 40 (4), 389-394.

Yin, C.Y., Aroua, M.K., and Daud, W.M.A.W. (2007), 'Review of modifications of activated carbon for enhancing contaminant uptakes from aqueous solutions', *Sep. Purif. Technol.,* 52 (3), 403-415.

Zabihi, M., Haghighi Asl, A., and Ahmadpour, A. (2010), 'Studies on adsorption of mercury from aqueous solution on activated carbons prepared from walnut shell', *J. Hazard. Mater.,* 174 (1–3), 251-256.

Zhang, K., Cheung, W.H., and Valix, M. (2005), 'Roles of physical and chemical properties of activated carbon in the adsorption of lead ions', *Chemosphere,* 60 (8), 1129-1140.

Chapter 4

Novel EPS/TiO$_2$ Nanocomposite Prepared from Recycled Polystyrene

Abstract

The synthesis and characterization of a new nanocomposite material that was prepared from recycled expanded polystyrene (EPS) and titanium dioxide (TiO$_2$) is reported here. The EPS was obtained from chemical reagent box insulation. To obtain the nanocomposite, these materials were dispersed in a solvent, mixed with TiCl4 and heated. The resulting new material was characterized with SEM, TEM, TGA, BET, Raman and IR techniques. The Raman and IR spectra provided complementary information regarding the structure of the nanocomposite. The Raman spectra were used to identify the crystalline structure of TiO$_2$ in the nanocomposite. In contrast, the IR spectra were used to identify the organic portion of the nanocomposite. The TEM images indicated that the nanocomposites had an average particle size of 6-12 nm. In addition, the adsorption and photocatalytic properties of the new material were evaluated. The EPS/TiO$_2$ nanocomposite was efficient at degrading methylene blue (MB) dye solutions under UV irradiation. Furthermore, according to thermal analysis, this material had greater polymer stability due to the incorporation of TiO$_2$.

Keywords: nanocomposite, expanded polystyrene; TiO$_2$, photodegradation, methylene blue

4.1 Introduction

Titanium dioxide (TiO_2) is a common material that is used daily and is present in paints (as a pigment), cosmetics and foods. TiO_2 is inexpensive, non-toxic, and thermally stable, and it has a high refractive index and does not absorb visible light.(Nohynek, 2010) In addition, TiO_2 has three different crystalline forms including anatase, rutile and brookite.(Fujishima, 2008) TiO_2 is a semi-conductor material with well-established photocatalytic activity, especially when used in its anatase crystalline form.(Alonso, 2009; Kawahara, 2003; Ohno, 2003; Porkodi, 2007; J. Wang, 2007a) Furthermore, TiO_2 is a strong oxidant that can be used to mineralize organic contaminants.(Zan, 2004)-(Lim, 2008) In recent years, TiO_2 was extensively used in the development of new water and air treatment technologies because it is easy to implement and operates across a broad temperature range. However, because of its size, TiO_2 must be fixed on a suitable substrate to improve the effectiveness of the oxidation process. Several different types of materials have been used as substrates including metals (Choudhary, 2008)], glass, ceramics (Cho, 2001; Lin, 2011; Yang, 2010) and polymers (Lowes, 2009). One specific polymer that has been used for this purpose is polystyrene (PS) (Magalhães, 2009; Shang, 2003). However, polymers like PS can cause serious environmental and economic problems because they do not biodegrade well and may be pollution sources. Thus, various polymer recycling methods were developed in the last few years (Fa, 2008; Kumar, 2009; G. L. Liu, 2009; G. Liu, 2010; Shang, 2003; Yang, 2010; Zan, 2004; Zan, 2006; Zhao, 2008). Very small beads of extruded polystyrene (EPS) can be manufactured that contain between 4 and 7% of the blowing agent (usually pentane or butane). Due to its versatility, dimensional

51

stability, cleanliness and low cost, EPS is widely used, especially in insulation and packing materials.

Several studies have focused on the synthesis of nanocomposites, such as PS/TiO$_2$. These studies have captured a great deal of attention in the past few years (Gandhi, 2012; Jaleh, 2011; Luo, 2008; Song, 2008; Wibawa, 2011). The use of reagents and monomers to produce these nanocomposites generates high energy and, in some cases, produces more contaminated waste (Antonietti, 2002; Palaniappan, 2008; Peng, 2009; Rozenberg, 2008; Tang, 2007; Y. Wang, 2007b; Wu, 2010; Zhang, 2006). This study introduces the use of an alternative material for creating new nanocomposites from TiO$_2$ and recycled expanded polystyrene (EPS).

Because EPS usually ends up in landfills or is incinerated, the large physical volume of EPS poses a severe contamination problem. In the past few years, EPS has been manually recycled as a hardwood replacement for garden furniture, as a slate replacement for roofing tiles and as a medium for new plastic items, such as coat hangers, CDs and video cases (2005; Montgomery, 2004; Singh, 2008; Suresh Kumar, 2004; Yan, 2008) .

This study presents a new and simple way to recycle EPS into a EPS/TiO$_2$ nanocomposite. This new material was characterized by TEM, SEM, TGA, FT-IR and Raman spectroscopy. Photocatalytic experiments were conducted to evaluate the catalytic properties of this new material. In addition, the results were compared with those from commercially available TiO$_2$.

4.2 Experimental

4.2.1 *Reagents*

Reagent grade titanium tetrachloride ($TiCl_4$), benzene and methylene blue (MB) were used in these experiments. The EPS was obtained from the insulation and packaging materials that were used to ship solvent grade acetone bottles. This recycled material was the main reagent in the synthesis of the EPS/TiO_2 nanocomposite material.

4.2.2 *Preparation of the EPS/TiO₂ Nanocomposite*

The method for synthesizing nanocomposite EPS/TiO_2 was simple. The first step of dispersing the recycled polymeric material in benzene was conducted at room temperature. A suitable amount of $TiCl_4$ was slowly added to the PS that was dispersed in benzene. This mixture was heat treated at 300°C for approximately 3 h. After the mixture was allowed to return to room temperature, a black powder product was obtained.

4.2.3 *EPS/TiO₂ Nanocomposite Characterization*

Particle size and shape distribution are two important nanoparticle characteristics. Thus, the size, shape, surface area and spectroscopic properties of the nanoparticles were determined. Each of the obtained nanocomposite materials was characterized by using a combination of the following techniques.

4.2.4 *Surface Area*

Nitrogen adsorption isotherms and surface area measurements were performed using nitrogen at 77 K. First, the samples were degassed by heating at a rate of 5 K/min and by evacuating at a rate of 50 mm Hg/s for 6 h. The specific surface area was determined using the Langmuir method at a relative pressure range of 0.01–0.20 Torr. A static volumetric adsorption unit (ASAP 2020 Micrometrics, Norcross, GA, USA) was used for these analyses.

4.2.5 *FTIR and Raman spectroscopy*

Raman spectra were collected with a Renishaw RM2000 microspectrometer that was equipped with 532 and 785 nm excitation sources. Raman spectra were acquired under the following conditions: a spectral range of 100-3200 cm^{-1}; an accumulation of 2; an acquisition time of 20 s; and laser power levels of 10-60 mW. A Bruker Optics IFS 66 series FT-IR spectrometer coupled to a Hyperion Infrared Microscope and the OPUS™ 4.0 data acquisition and analysis suite was used to obtain the IR spectra of the starting materials and the prepared nanocomposites.

4.2.6 *SEM and TEM Images*

Scanning Electron Microscope (SEM) and Transmission Electron Microscope (TEM) images were used to determine the average particle size and morphology of the prepared nanocomposites. The SEM images were obtained with a JEOL JSM-541 OL SEM microscope. The TEM images were used to observe the morphologies of the nanocomposite particles. First, the nanocomposite samples were dispersed in benzene.

Next, a portion of the dispersed sample was placed (using a dropper) on a copper grid that was coated with Formvar and a carbon film. The solvents were allowed to evaporate on the grid. The TEM images were recorded by a model 1011 transmission electron microscope that had a lattice resolution of 0.2 nm and a magnification between 50 and 10^6 at an accelerating voltage of between 40 and 100 kV (JEOL, Peabody, MA). The samples were prepared by placing 1.0 μL of the Ag-NPs solution on ultrathin carbon film/holey carbon 400 mesh copper TEM grids (01824, Ted Pella, Inc., Redding, CA). The solvents were allowed to evaporate at room temperature. The grids were stored in a desiccator to provide a dust free environment. White light images were obtained with an Olympus America, Inc. (Center Valley, Pa, USA) model BH2-UMA high resolution optical microscope that was equipped with 10-250 $\times$ magnification and a 6.0 MB PAX-Cam image capturing CCD camera controlled by PAX-it!™ Software (Midwest Information Systems, Inc., Villa Park, IL, USA).

4.2.7   TGA Analysis

The thermal degradation behavior of the samples was analyzed with a thermal gravimetric analyzer (TGA) model Q-500 (TA Instruments, New Castle, DE, USA). Aluminum pans (5 mm I.D.) were used to hold the standards, and platinum sample holders were used to hold the nanocomposites. Approximately 5 mg of dried material was heated from 20 to 600°C at a scan speed of 10°C/min.

4.2.8   Photocatalytic Degradation Capability of EPS/TiO$_2$

The nanocomposite photodegradation capability was evaluated by using a

discoloration method with the methylene blue (MB) dye. For these tests, 30 mg of the EPS/TiO$_2$ composite were mixed with 10 mL of a 14 ppm MB solution. A 2.0 mL aliquot of this reaction mixture was removed with a syringe at pre-determined time intervals. The sampled aliquots were filtered through 0.45 nm Millipore membranes before analysis with a UV/Vis spectrophotometer (Agilent 8453 UV-Visible). The MB concentration was monitored by measuring the absorbance of the sample filtrate at 663 nm. All the experiments were performed in batches. The catalytic efficiency of the nanocomposite was evaluated by measuring the decolorizing efficiency of the MB solutions. All the samples were analyzed in triplicate and commercial TiO$_2$ was used as the control or blank.

4.3   Results and Discussion.

The new EPS/TiO$_2$ nanocomposite was characterized with various analytical techniques. The TEM images are shown in Figure 4.1a-b and indicate that the particles were nearly spherical in form. The darker areas in the images correspond with TiO$_2$, and lighter gray and white areas correspond with the recycled EPS. These images confirm the presence of these two materials in the final product. The average nanoparticle sizes were between 5 and 15 nm. In addition, the TEM images show the morphology of the formed nanocomposite. The TiO$_2$ occurred in the form of islands within the polymeric matrix and was agglomerated in some regions. The SEM images (Figure 4.1c-d) show a granular morphology with a size of less than 100 μm. In Figure 4.1d, the SEM image focuses in on one EPS/TiO$_2$ grain. In this case, a smooth particle surface was observed.
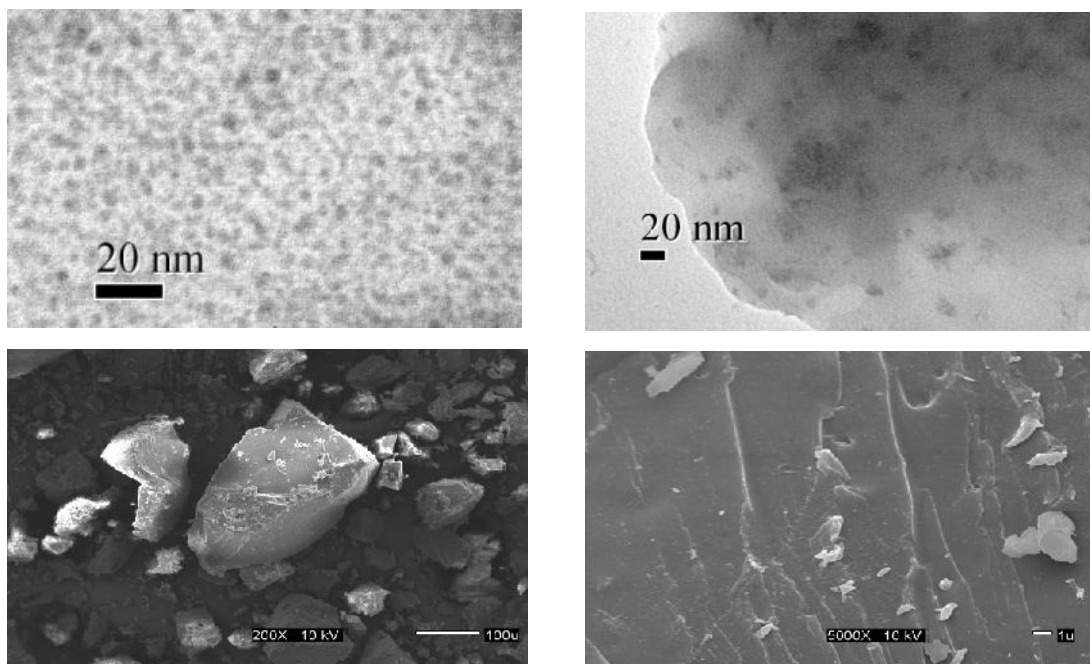
Figure 4.1 SEM and TEM images of the EPS/TiO₂ nanocomposite. Micrographs of the TEM images (a) and (b). The SEM images, (c) and (d).

The FT-IR spectra of the TiO_2, EPS and EPS/TiO_2 were compared to observe the vibrational pattern changes of the nanocomposite spectra relative to those of the parent compounds. Figure 4.2 shows the FT-IR spectra of the rutile-TiO_2, untreated EPS films and EPS/TiO_2. Nearly all of the vibrational information that was observed in the starting materials was observed in the nanocomposite. Persistent vibrational signatures that corresponded to phenyl ring vibrations were identified at approximately 1630, 1490 and 1450 cm^{-1}.
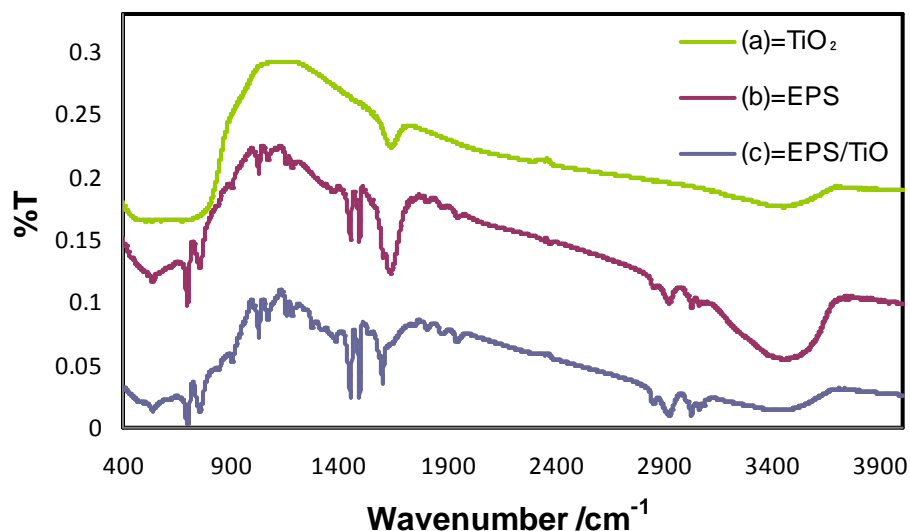
Figure 4.2. FT-IR spectra of, (a) rutile TiO$_2$, (b) EPS, and (c) EPS/TiO$_2$ nanocomposite.

A broad band at approximately 3400 cm^{-1} was attributed to surface hydroxyl bending vibrations. Figure 3 shows the Raman spectra of the TiO$_2$ in the anatase and rutile phases and in the nanocomposite. These spectra were obtained to identify which of the bands from these crystalline forms were present in the final product. The main signal corresponded to the anatase phase. The Raman spectra of the new material and TiO$_2$ shows bands that correspond to TiO$_2$, which supports the presence of this material in the final product and indicates that no significant changes in the vibrational profile of the polymer occurred in the low frequency region (Figure 4.3).
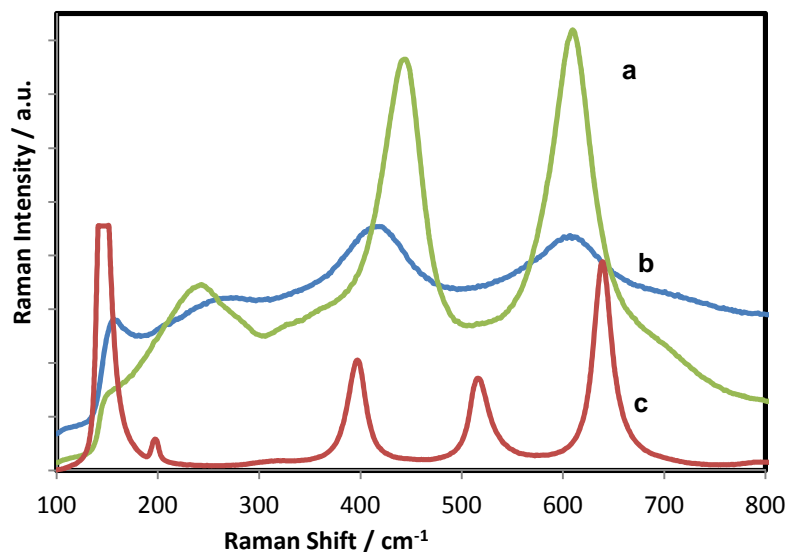
Figure 4. 3. Raman spectra of the (a) anatase phase of TiO_2, (b) EPS/TiO_2 nanocomposite, and (c) rutile TiO_2

The thermal behavior of the EPS/TiO_2 nanocomposite was measured and compared to that of the recycled EPS. TGA analysis of the EPS/TiO_2 and EPS resulted in different mass loss profiles at different temperatures. While the thermal degradation of EPS/TiO_2 begins at 344 °C with a 5% of weight loss, that of the recycled EPS begins at 293 °C, which is more than 50 °C earlier than that of the EPS/TiO_2 nanocomposite. This shift reflects that the incorporation of TiO_2 into the polymer improves its thermal stability. The EPS and nanocomposite curves in a nitrogen atmosphere are shown in Figure 4.4.

These results were similar to those obtained by Dzunuzovic et al. The final synthesis product that was described in this paper (EPS/TiO_2) had similar thermal properties to those of the nanocomposite that was formed by the polymerization of styrene (Džunuzovi , 2009). Thus, this new chemical process provides an important contribution to industrial sustainability and embraces its challenges.

In addition, the absorbent and catalytic properties of EPS/TiO$_2$ were studied and evaluated. The gas adsorption results showed that the new material had a poor adsorption capacity. This result was confirmed by the BET analysis results, in which the surface area was relatively low (BET surface area of 5.11 m^2/g). Figure. 4.5 contains the EPS/TiO$_2$ composite adsorption results.
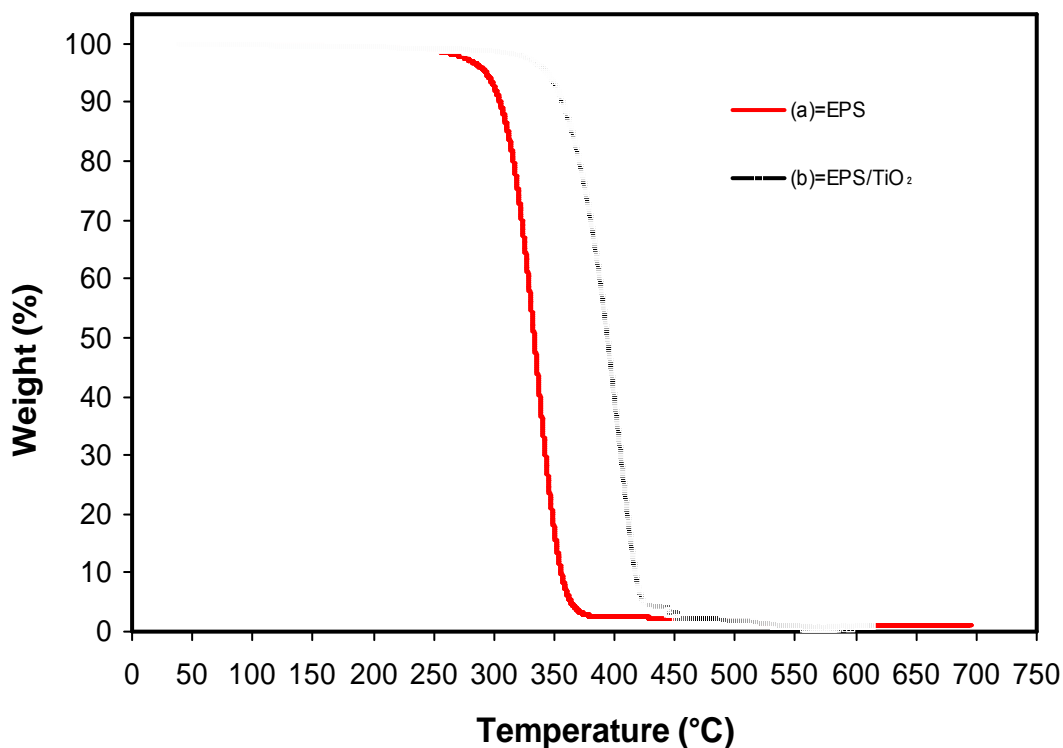
Figure 4.4. Thermo gravimetric curves of the EPS (red trace) and EPS/TiO$_2$ (black trace).
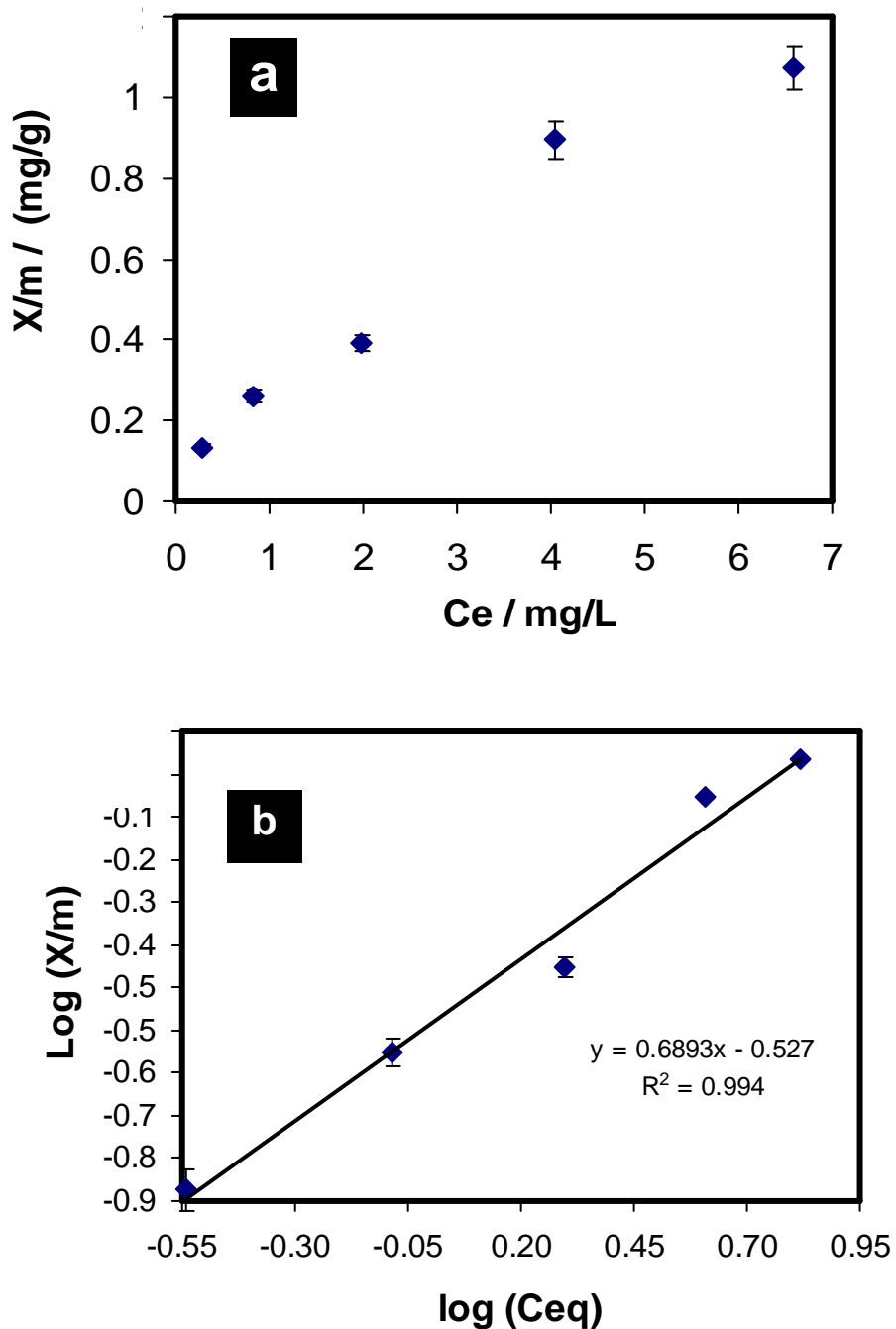
Figure 4. 5. The adsorption capacity of several MB aqueous solution concentrations including (a) normal plot of amount adsorbed vs. equilibrium concentration and (b) the Freundlich plot of the data represented in (a).

The adsorption capacity of the composite was also determined to ensure that adsorption was not the only process that occurred. However, this process is important for heterogeneous photocatalysis. The adsorption capacity of EPS/TiO$_2$ was analyzed

by using MB. Approximately 0.01 g of the EPS/TiO_2 sample were added to aqueous MB

solutions and magnetically stirred for 2 h. The samples were placed in the dark to

prevent photodecomposition by white light irradiation. After various contact times, the

MB concentration was measured to evaluate its dependency on the contact time with

EPS/TiO_2. The MB concentration remained constant during nearly 12 h of contact. The

Freundlich Isotherm model best fit the results. The well-known linear form of the

Freundlich model is shown below.

$x/m = K_F\,Ceq^{1/n}$ 4. 1

    or

$\log(x/m) = \log K_F + 1/n\,\log Ceq$ 4. 2

Where K_F is the "Freundlich" equilibrium constant and $1/n$ is a constant that can

be evaluated with the linearized Freundlich equation (Eq. 4.2). The amount of analyte

that is adsorbed at equilibrium (mg, MB) is represented by x/m, where m is the mass of

the adsorbent (g) and Ceq is the equilibrium concentration of the adsorbate (MB).
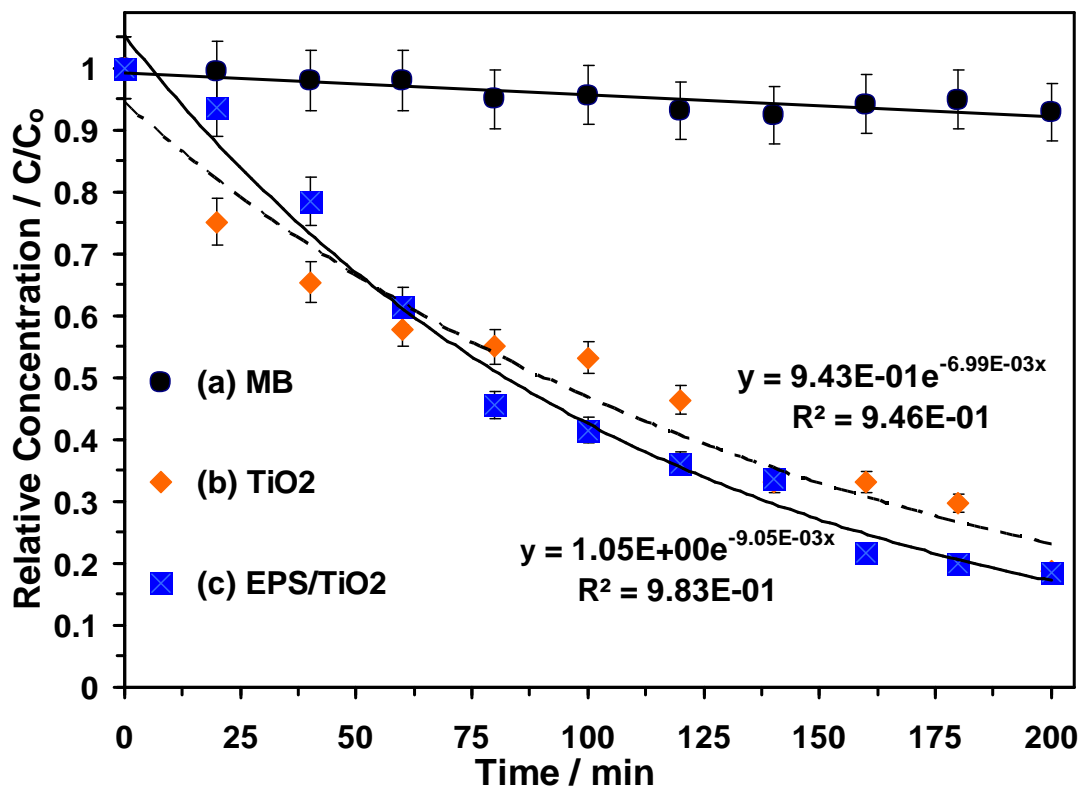
Figure 4.6. Photocatalytic degradation of MB under UV light irradiation. (a) MB without TiO_2, (b) 30 mg of TiO_2 in contact with MB, and (c) 30 mg of EPS/TiO_2 in contact with MB.

If ($1/n$) approaches 1, then the equation is linear. This linear equation occurs for a limited range of the adsorption values. For the complete range of values, the non-linear isotherm data can be plotted in a linear form by taking the log of both sides of the equation. The linear fit of the adsorption data that is shown in Figure. 4.5b is $\log(x/m) = 0.689 \log(C_{eq}) - 0.513$ (with a coefficient of determination of $R^2 = 0.994$, $1/n = 0.689$ ($n = 1.45$) and $K_F = 0.307$). The value of $1/n$ is related to the heterogeneity of the materials surface. Based on these results, the adsorption in this composite is semi-heterogeneous. Another way to evaluate the adsorption efficiency of the material is with a cross comparison experiment that is designed to evaluate the photocatalytic activity of EPS/TiO_2 and TiO_2. The results of these experiments are presented in Figure. 4.6. A

similar degradation time was observed for EPS/TiO$_2$ and the commercial TiO$_2$ when 30 mg of material were added to the MB solutions.

In addition, an alternative method was used to determine the photocatalytic activity of EPS/TiO$_2$. This method was conducted using the discoloration efficiency value (*D*) of the MB solution as a comparative parameter and was used by Su et al. in 2007. The catalytic reaction was performed in a flask under UV irradiation at 254 nm. Exactly 50 mg of powder were added to 10 mL of a 14 mg/L MB solution. Next, the system was stirred for under UV irradiation at 254 nm before measuring the absorbance as a function of time (Su, 2007).

The discoloration efficiency values were calculated by using the MB solution absorbance that was determined after it was in contact with the EPS/TiO$_2$. The discoloration efficiency was evaluated using Eq. 4.3 in terms of percent discoloration (*D*).

$$D \, (\%) = \{(C_o - C_t)/C_o\} \times 100\% \qquad\qquad\qquad 4.3$$

Where, *D* represents the discoloration efficiency (%) of the MB solutions, C_o and C_t represent the absorption values of the MB solutions at the initial time $t = 0$ and at a particular time *t*, respectively. Commercial TiO$_2$ was used as a reference material. Figure 4.7 shows the representative discoloration for MB with the EPS/TiO$_2$ and TiO$_2$ photocatalysts.
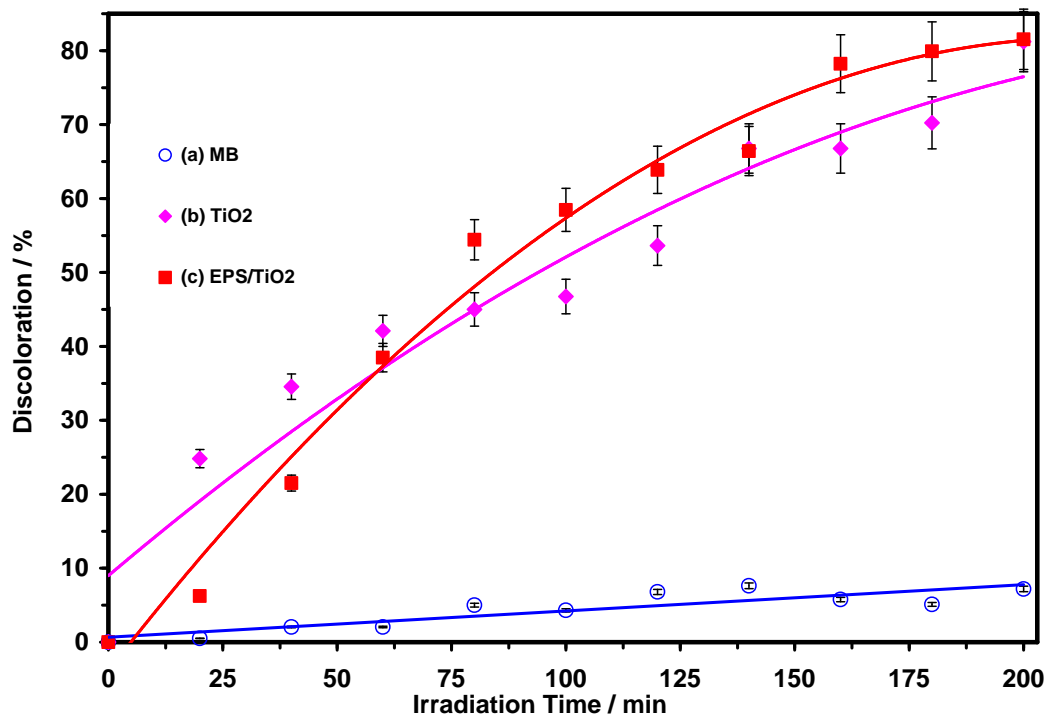
Figure 4.7. Discoloration of the MB solutions under UV light irradiation of, (a) MB with EPS/TiO$_2$, (b) MB with TiO$_2$, and (c) MB without TiO$_2$ or EPS/TiO$_2$ (control).

The best discoloration behavior was observed in the EPS/TiO$_2$ nanocomposite. The percent discoloration of the MB solutions reached 98% (data not shown). Poor discoloration of the MB solutions was observed when the photocatalysts were not added to the solutions (control runs), which confirmed the photocatalytic activity of the nanocomposite.

4.4 Conclusions.

A new nanocomposite made with extruded polystyrene (EPS/TiO$_2$) was synthesized from recycled polymer sources. The new material was characterized by various techniques, such as SEM, TEM, BET, FT-IR, and Raman spectroscopy. No differences in vibrational spectra were observed between the EPS and EPS/TiO$_2$, which

indicated that TiO_2 was attached to the polystyrene and produced a black nanocomposite with an average particle size of between 5 and 12 nm. Raman spectroscopy was used as a complementary tool to evaluate the inorganic portion of the new nanocomposite including the anatase phase of the TiO_2. The EPS/TiO_2 nanocomposite had high discoloration efficiency for aqueous methylene blue (MB) solutions. The percent of discoloration reached 98% in the MB solution. Better results were obtained for the new nanocomposite than for the commercially available one. Thus, EPS/TiO_2 will be used in future degradation tests of persistent organic pollutants that occur in water.

References

Alonso, E., Montequi, I., and Cocero, M.J. (2009), 'Effect of synthesis conditions on photocatalytic activity of TiO_2 powders synthesized in supercritical CO_2', *J. Supercrit. Fluids,* 49 (2), 233-238.

Antonietti, M. and Landfester, K. (2002), 'Polyreactions in miniemulsions', *Prog. Polym. Sci.,* 27 (4), 689-757.

Cho, S. and Choi, W. (2001), 'Solid-phase photocatalytic degradation of PVC-TiO2 polymer composites', *J. Photochem. Photobiol., A.,* 143 (2-3), 221-228.

Choudhary, V.R., Patil, V.P., Jana, P., and Uphade, B.S. (2008), 'Nano-gold supported on Fe2O3: A highly active catalyst for low temperature oxidative destruction of methane green house gas from exhaust/waste gases', *Appl. Catal., A,* 350 (2), 186-190.

Džunuzovi , E., Vodnik, V., Jeremi , K., and Nedeljkovi , J.M. (2009), 'Thermal properties of PS/TiO2 nanocomposites obtained by in situ bulk radical polymerization of styrene', *Mater. Lett.,* 63 (11), 908-910.

Fa, W., Zan, L., Gong, C., Zhong, J., and Deng, K. (2008), 'Solid-phase photocatalytic degradation of polystyrene with TiO_2 modified by iron (II) phthalocyanine', *Appl. Catal., B,* 79 (3), 216-223.

Fujishima, A., Zhang, X., and Tryk, D.A. (2008), 'TiO_2 photocatalysis and related surface phenomena', *Surf. Sci. Rep.,* 63 (12), 515-582.

Gandhi, K., Dixit, B.K., and Dixit, D.K. (2012), 'Effect of addition of zirconium tungstate, lead tungstate and titanium dioxide on the proton conductivity of polystyrene porous membrane', *Int. J. Hydrogen Energy,* 37 (4), 3922-3930.

Jaleh, B., Madad, M.S., Habibi, S., Wanichapichart, P., and Tabrizi, M.F. (2011), 'Evaluation of physico-chemical properties of plasma treated PS–TiO2 nanocomposite film', *Surf. Coat. Technol.,* 206 (5), 947-950.

Kawahara, T., Ozawa, T., Iwasaki, M., Tada, H., and Ito, S. (2003), 'Photocatalytic activity of rutile–anatase coupled TiO_2 particles prepared by a dissolution–reprecipitation method', *J. Colloid Interface Sci.,* 267 (2), 377-381.

Kumar, A.P., Depan, D., Singh Tomer, N., and Singh, R.P. (2009), 'Nanoscale particles for polymer degradation and stabilization--Trends and future perspectives', *Prog. Polym. Sci.,* 34 (6), 479-515.

Lim, J.I., Yu, B., Woo, K.M., and Lee, Y.-K. (2008), 'Immobilization of TiO_2 nanofibers on titanium plates for implant applications', *Appl. Surf. Sci.,* 255 (5, Part 1), 2456-2460.

Lin, L.-H., Liu, H.-J., Hwang, J.-J., Chen, K.-M., and Chao, J.-C. (2011), 'Photocatalytic effects and surface morphologies of modified silicone-TiO$_2$ polymer composites', *Mater. Chem. Phys.,* 127 (1-2), 248-252.

Liu, G., Zhu, D., Zhou, W., Liao, S., Cui, J., Wu, K., and Hamilton, D. (2010), 'Solid-phase photocatalytic degradation of polystyrene plastic with goethite modified by boron under UV-vis light irradiation', *Appl. Surf. Sci.,* 256 (8), 2546-2551.

Liu, G.L., Zhu, D.W., Liao, S.J., Ren, L.Y., Cui, J.Z., and Zhou, W.B. (2009), 'Solid-phase photocatalytic degradation of polyethylene-goethite composite film under UV-light irradiation', *J. Hazard. Mater.,* 172 (2-3), 1424-1429.

Lowes, B., Bohrer, A., Tran, T., and Shipp, D. (2009), 'Grafting of polystyrene "from" and "through" surface modified titania nanoparticles', *Polym. Bull.,* 62 (3), 281-289.

Luo, H.L., Sheng, J., and Wan, Y.Z. (2008), 'Preparation and characterization of TiO2/polystyrene core–shell nanospheres via microwave-assisted emulsion polymerization', *Mater. Lett.,* 62 (1), 37-40.

Magalhães, F. and Lago, R.M. (2009), 'Floating photocatalysts based on TiO$_2$ grafted on expanded polystyrene beads for the solar degradation of dyes', *Sol. Energy,* 83 (9), 1521-1526.

Montgomery, R. (2004), 'Development of biobased products', *Bioresour. Technol.,* 91 (1), 1-29.

Nohynek, G.J., Antignac, E., Re, T., and Toutain, H. (2010), 'Safety assessment of personal care products/cosmetics and their ingredients', *Toxicol. Appl. Pharmacol.,* 243 (2), 239-259.

Ohno, T., Tokieda, K., Higashida, S., and Matsumura, M. (2003), 'Synergism between rutile and anatase TiO2 particles in photocatalytic oxidation of naphthalene', *Appl. Catal., A,* 244 (2), 383-391.

Palaniappan, S. and John, A. (2008), 'Polyaniline materials by emulsion polymerization pathway', *Prog. Polym. Sci.,* 33 (7), 732-758.

Peng, B., Tang, F., Chen, D., Ren, X., Meng, X., and Ren, J. (2009), 'Preparation of PS/TiO2/UF multilayer core-shell hybrid microspheres with high stability', *J. Colloid Interface Sci.,* 329 (1), 62-66.

Porkodi, K. and Arokiamary, S.D. (2007), 'Synthesis and spectroscopic characterization of nanostructured anatase titania: A photocatalyst', *Mater. Charact.,* 58 (6), 495-503.

Rozenberg, B.A. and Tenne, R. (2008), 'Polymer-assisted fabrication of nanoparticles and nanocomposites', *Prog. Polym. Sci.,* 33 (1), 40-112.

Shang, J., Chai, M., and Zhu, Y. (2003), 'Solid-phase photocatalytic degradation of polystyrene plastic with TiO2 as photocatalyst', *J. Solid State Chem.,* 174 (1), 104-110.

Singh, B. and Sharma, N. (2008), 'Mechanistic implications of plastic degradation', *Polym. Degrad. Stab.,* 93 (3), 561-584.

Song, M., Pan, C., Li, J., Zhang, R., Wang, X., and Gu, Z. (2008), 'Blends of TiO_2 nanoparticles and poly (N-isopropylacrylamide)-co-polystyrene nanofibers as a means to promote the biorecognition of an anticancer drug', *Talanta,* 75 (4), 1035-1040.

Su, B., Ma, Z., Min, S., She, S., and Wang, Z. (2007), 'Preparation of TiO_2/PS complex nanoparticles', *Mater. Sci. and Eng., A,* 458 (1–2), 44-47.

Suresh Kumar, M., Mudliar, S.N., Reddy, K.M.K., and Chakrabarti, T. (2004), 'Production of biodegradable plastics from activated sludge generated from a food processing industrial wastewater treatment plant', *Bioresour. Technol.,* 95 (3), 327-330.

Tang, E., Liu, H., Sun, L., Zheng, E., and Cheng, G. (2007), 'Fabrication of zinc oxide/poly(styrene) grafted nanocomposite latex and its dispersion', *Eur. Polym. J.,* 43 (10), 4210-4218.

Wang, J., Zhao, G., Zhang, Z., Zhang, X., Zhang, G., Ma, T., Jiang, Y., Zhang, P., and Li, Y. (2007a), 'Investigation on degradation of azo fuchsine using visible light in the presence of heat-treated anatase TiO2 powder', *Dyes Pigm.,* 75 (2), 335-343.

Wang, Y., Ke, Y., Li, J., Du, S., and Xia, Y. (2007b), 'Dispersion behavior of core-shell silica-polymer nanoparticles', *China Particuology,* 5 (4), 300-304.

Wibawa, P.J., Saim, H., Agam, M.A., and Nur, H. (2011), 'Design, Preparation and Characterization of Polystyrene Nanospheres Based-Porous Structure towards UV-Vis and Infrared Light Absorption', *Phys. Procedia,* 22 (0), 524-531.

Wu, Y., Zhang, Y., Xu, J., Chen, M., and Wu, L. (2010), 'One-step preparation of PS/TiO2 nanocomposite particles via miniemulsion polymerization', *J. Colloid Interface Sci.,* 343 (1), 18-24.

Yan, S., Bala Subramanian, S., Tyagi, R.D., and Surampalli, R.Y. (2008), 'Bioplastics from activated sludge treating pulp and paper wastewater', *J. Biotechnol.,* 136 (Supplement 1), S31-S32.

Yang, C., Gong, C., Peng, T., Deng, K., and Zan, L. (2010), 'High photocatalytic degradation activity of the polyvinyl chloride (PVC)-vitamin C (VC)-TiO_2 nano-composite film', *J. Hazard. Mater.,* 178 (1-3), 152-156.

Zan, L., Tian, L., Liu, Z., and Peng, Z. (2004), 'A new polystyrene-TiO$_2$ nanocomposite film and its photocatalytic degradation', *Applied Catalysis A: General,* 264 (2), 237-242.

Zan, L., Wang, S., Fa, W., Hu, Y., Tian, L., and Deng, K. (2006), 'Solid-phase photocatalytic degradation of polystyrene with modified nano-TiO2 catalyst', *Polymer,* 47 (24), 8155-8162.

Zhang, J., Gao, G., Zhang, M., Zhang, D., Wang, C., Zhao, D., and Liu, F. (2006), 'ZnO/PS core-shell hybrid microspheres prepared with miniemulsion polymerization', *J. Colloid Interface Sci.,* 301 (1), 78-84.

Zhao, X., Li, Z., Chen, Y., Shi, L., and Zhu, Y. (2008), 'Enhancement of photocatalytic degradation of polyethylene plastic with CuPc modified TiO$_2$ photocatalyst under solar light irradiation', *Appl. Surf. Sci.,* 254 (6), 1825-1829.

Chapter 5

Surface Enhanced Raman Scattering (SERS) Studies of Gold and Silver Nanoparticles Prepared by Laser Ablation

Abstract

Gold and silver nanoparticles (NPs) were prepared in water, acetonitrile and isopropanol by laser ablation methodologies. The average characteristic (longer) size of the NPs obtained ranged from 3 to 70 nm. 4-Aminobenzebethiol (4-ABT) was chosen as the surface enhanced Raman scattering (SERS) probe molecule to determine the optimum irradiation time and the pH of aqueous synthesis of the laser ablation-based synthesis of metallic NPs. The synthesized NPs were used to evaluate their capacity as substrates for developing more analytical applications based on SERS measurements. A highly energetic material, TNT, was used as the target compound in the SERS experiments. The Raman spectra were measured with a Raman microspectrometer. The results demonstrate that gold and silver NP substrates fabricated by the methods developed show promising results for SERS-based studies and could lead to the development of micro sensors.

5.1 Introduction

The many uses of nanotechnology include very important applications in areas, such as medicine (Albrecht, 2005; Chen, 2008; Hamouda, 2012; Piao, 2011; Rai, 2009), catalysis (Chang, 2012; Chen, 2011; Eriksson, 2004; Haruta, 2003; Hutchings, 2012; Lee, 2007; Niu, 2003; Wei, 2010; Yang, 2012), industrial applications (El-Rafie, 2012; Jung, 2010; Yu, 2008) and scientific investigations. The size, shape and physicochemical properties are very important in future applications and are the main theme in studies currently conducted. There are several ways to synthesize metal nanoparticles (NPs). Their synthesis can be classified as either chemical or physical methods. Some chemical methods include the chemical reduction of metal salts, the alcohol reduction process, the polyol process, microemulsions, the thermal decomposition of metal salts and electrochemical synthesis (Ganesh, 2006; Lawrence, 2006). Physical methods include pulsed laser ablation, the exploding wire technique, plasma, chemical vapor deposition, microwave irradiation, supercritical fluids, sono-chemical reduction and gamma radiation (Sergeev, 2006). Laser ablation is a very clean physical method for the preparation of metallic nanoparticles (NPs). During the last year, the laser ablation of metals has increased in popularity, due to the fast and simple nature of the procedure. In addition, the important advantage of this method when compared to chemical synthesis ("wet chemistry syntheses") is the preparation of high surface purity NPs in the chosen solvent. There are no counter ions and no residuals of the reducing agents remaining on the surfaces of the NPs (Haibo, 2012; Stratakisa, 2012; Takeshi, 2012). To take advantage of these features, we have prepared gold (Au) and silver (Ag) NPs by laser ablation. Colloidal suspensions of prepared NPs were

deposited on gold-coated slides to immobilize them and to test them for potential use as substrates for the detection of explosives using surface enhanced Raman scattering (SERS).

The use of spectroscopic techniques with intensities augmented by nanostructured metal surfaces has attracted great interest in recent years. The SERS effect discovered in the seventies is largely attributed to the interaction of light with matter. Specifically, SERS is related to the inelastic scattering (or Raman scattering) of certain molecules in the presence of specially prepared roughened or discontinuous metallic nanostructures. There are two mechanisms that explain the increase in the Raman signal. The first is explained through an electromagnetic interaction model (EM) and the second through a chemical interaction model or charge transfer (CT) (López-Tocón, 2001; Luo, 2006). Both mechanisms are thought to contribute to the signal intensity enhancement observed, although the extent of the contribution of each source of enhancement depends on the system under study. The enhancement mechanisms of the Raman signal lead to a technique with a sensitivity and selectivity that make Raman scattering a highly promising technique for further developing analytical applications (Hou, 2011; Kundu, 2004; Photopoulos, 2011; O. M. Primera-Pedrozo, 2008; Oliva M. Primera-Pedrozo, 2012; Vlckova, 2007). These applications are closely related to the properties and the surface morphology of the metallic NP used. A large part of the contribution to the SERS effect is due to the increase in the inelastically scattered Raman signal intensity by the nanostructured metal systems present and the particular properties of the particles to induce greater morphological coupling with the incident radiation, resulting in intense spectroscopic signals. The molecule-surface relative

orientation allows the emergence of new selection rules, resulting in the intensification of the Raman spectrum bands corresponding to the molecular vibrations of the molecular polarizability components perpendicular to the surface. The Au and Ag NPs prepared by laser ablation were deposited on various substrates and subsequently evaluated as SERS substrates, with the objective of detecting explosives, such as TNT.

5.2   Experimental Section

5.2.1   *Laser Ablation Synthesis*

Au or Ag metal foils (99.99%, Sigma-Aldrich, Milwaukee, WI, USA) were placed in a vial containing 10 mL of deionized water as ablation and heat tempering media. Laser pulses at 1064 nm, obtained using a Quanta-Ray Pro Series pulsed Nd:YAG laser from Spectra-Physics/Newport Corporation (Mountain View, CA, USA), were used to ablate the metallic foils. The laser was operated in single-shot mode (5 ns, 10 Hz). The target was irradiated using a focusing lens with a focal length of 86.4 cm. The laser power used was 0.980 mW, and the energy was 106 mJ. The ablation process was carried out for time intervals of 5, 10, 15 and 20 min of near IR laser pulse irradiation.

5.2.2   *Characterization of NPs Suspensions*

A UV-Vis spectrophotometer (Agilent model 8453, Santa Clara, CA, USA) was used to acquire the electronic absorption spectra of the NPs in water. The spectra were recorded in the range of 300 to 900 nm. Quartz cells with a 1.0 cm path length (72-Q-10, obtained from Starna Cells, Inc., Atascadero, CA, USA) were used for the experiments. The NPs morphology and size were obtained from high-resolution transmission electron microscopy (HR-TEM) images (Zeiss, model 922 operated at 200

kV). The samples for TEM analysis were prepared by depositing 5 µL of the metallic NP suspensions on ultrathin carbon film/holey carbon 400 mesh copper grids (01824 from Ted Pella, Inc., Redding, CA, USA). Zeta potential and hydrodynamic radius (HR) measurements were obtained using a Zetasizer™ Nano Series (Malvern Instruments Ltd., Worcestershire, UK).

5.2.3 Effect of pH on the Synthesis of NPs

Solutions of 1 mM 4-ABT were used as analytes to evaluate the pH effect on the synthesis by laser ablation of colloidal suspensions of Au and Ag NPs. The preparation method used was as described in Section 2.1. Studies were performed only at the optimum irradiation time. Dilute solutions of NaOH and HCl were used to adjust the pH in the aqueous media used as the solvent in the synthesis of nanoparticles. After the synthesis at various pH values was studied, the UV-Vis spectra of the suspensions were obtained. The pH values of the aqueous colloidal suspensions used for synthesis were 2.6, 4.8, 8.1 and 10.3.

5.2.4 Evaluation of SERS Activity

SERS spectra were excited with a 514.5 nm INNOVA 308 Argon ion laser or a 532 nm VERDI 6.0 solid-state diode laser (both from Coherent, Inc., Santa Clara, CA, USA) and a 785 nm solid-state laser (InProcess Inc., Salt Lake City, UT, USA). 4-Aminobenzebethiol (4-ABT, Sigma-Aldrich) and 1,2-bis(4-pyridyl)ethylene (BPE, Sigma-Aldrich) were used as SERS probe analytes. Renishaw Raman Microspectrometers RM1000 and RM2000 systems (Agiltron, Inc., Woburn, MA) were used to acquire

normal Raman (NR) and SERS spectra. The laser power at the samples was typically in the range of 10–60 mW. The data acquisition time was 20 s with 2 accumulations. The spectra are presented without pre-treatments or baseline corrections.

Au and Ag NPs at different pH values were used to evaluate the effect of the pH of the colloidal suspensions on the SERS activity obtained. Thus, 1.0 mM 4-ABT solutions and TNT solutions were used to evaluate the SERS activity at different pH values. Aliquots of 3 µL of TNT solutions at 1.0 mM were deposited on Au NP/Au substrates. To determine the surface enhancement factor (SEF), a solution of 4-ABT at 1.0×10^{-9} M was deposited on Au NP/Au substrates (approximately 5–10 µL of Au NPs deposited on Au substrates).

5.2.5 *Detection of TNT using Au NP/Au Substrates*

The low limit of detection (LOD) of TNT using Au NPs deposited on Au-coated glass slides and used as substrates for the NPs was calculated based on the SERS data. For the spectral measurements, aqueous solutions of 2,4,6-trinitoluene (TNT) of 1.0×10^{-4} M, 1.0×10^{-6} M and 1.0×10^{-10} M were used. Aliquots of 10 µL of Au NPs were deposited on Au-coated substrates, and Raman spectra were measured. Then, 2.5 µL of TNT solutions were deposited on Au NP films. The NPs used were prepared in acetone to facilitate the evaporation of the solvent and the quicker use of the substrate.

5.3 Results and Discussion

This contribution focuses on developing fast and simple methods for the preparation of SERS-active substrates with high sensitivity. For this purpose, NPs were synthesized using laser ablation methods. Au and Ag NP suspensions were

synthesized at different irradiation times (5, 10, 15 and 20 min). UV-Vis absorption measurements were obtained to characterize the NPs obtained (Figure 5.1A,B). The typical positions of the surface plasmon maximum absorption wavelength for Au NPs and Ag NPs were approximately 525 nm (Figure 5.1A) and 400 nm (Figure 5.1B), respectively. These absorption maxima correspond to spherical (or nearly spherical) NPs with a characteristic average diameter between 2 and 100 nm (Burda, 2005). These results were corroborated with TEM images and the corresponding statistical and morphological analyses.

(A)   (B)
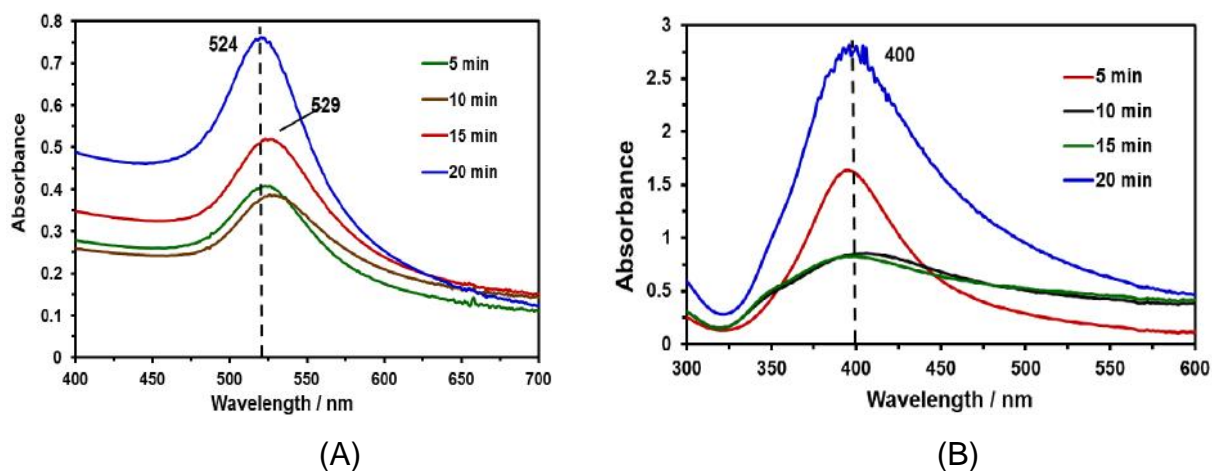
Figure 5.1. UV-Vis absorption spectra of Au and Ag NPs at various irradiation times. (A) absorption spectra of Au NPs, and (B) absorption spectra of Ag NPs.

TEM images of the prepared Au and Ag NPs are shown in Figure 5.2. Colloidal suspensions of Au NPs of different sizes were obtained. Purple colloids are typical of large Au NPs of approximately 126 ± 36 nm (Figure 5.2A). Red colloid suspensions have average sizes of 11 ± 4 nm (Figure 2B). The spherical shape is predominant in the images. Similarly, Figure 2C,D show TEM images of typical colloidal suspensions of Ag

NPs. Green-gray colloidal suspensions have NPs with spheroidal, large Ag NPs of approximately 132 ± 5 nm and yellow Ag NPs are spherical seeds of 5 ± 1 nm. The average sizes of the NPs shown in these TEM images were determined using the "ImageJ" program (NIH).

The effect of the irradiation time on the enhancements obtained in the SERS experiments using the metallic NPs prepared was evaluated using 4-ABT for Ag NPs. Similarly, 1,2-bis(4-pyridyl)ethylene (BPE) was used to evaluate the optimum conditions for the synthesis of Au NPs. These analytes were selected based on the affinity of the compounds with the corresponding NPs. Figure 5.3 displays the SERS spectrum results of Au NPs at different irradiation times. The best enhancement in the Raman signals for 4-ABT was observed at 20 min of irradiation time for Ag and Au NPs. The optimized parameter (20 min of irradiation) was used during all subsequent syntheses in this work. Aliquots of 5 µL of NP suspensions at different times of analysis were deposited on Au slides of approximately 0.25 cm^2. The drops of NP suspensions were allowed to dry in a desiccator overnight, and then, the analyte was deposited on the substrate and again placed in a desiccator.
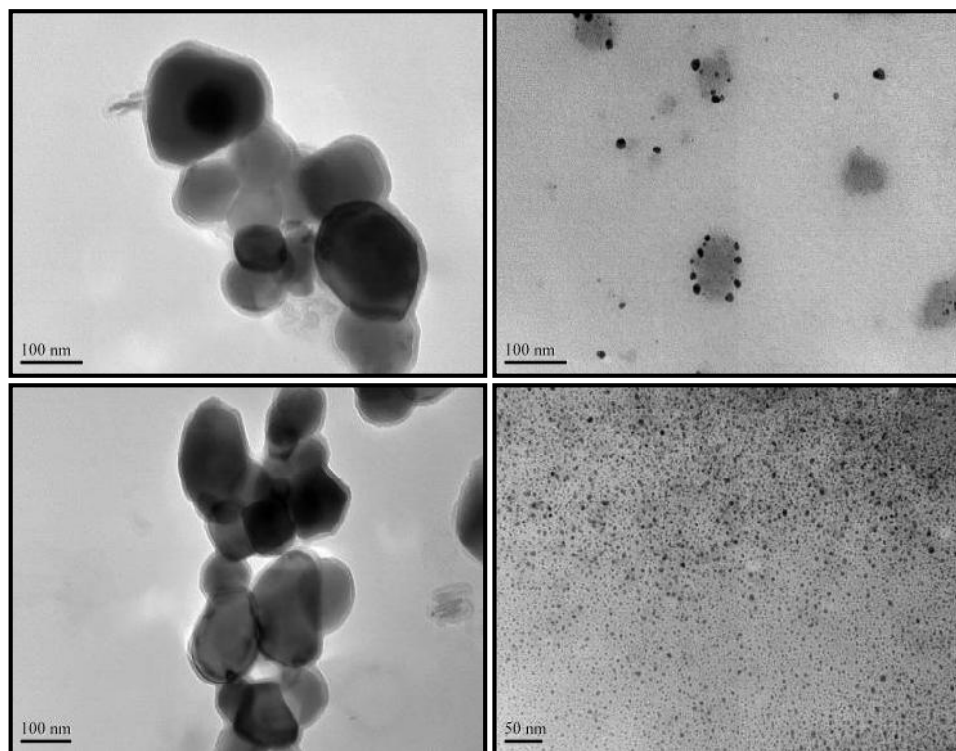
Figure 5.2. TEM images of Au and Ag NPs. Au NPs: (A) large spheres with average diameters of 126 ± 39 nm are violet. (B) red colloids have average diameters of 11 ± 4 nm Ag NPs: (C) yellow Ag NPs suspensions have average sizes of 132 ± 5 nm; (D) silver seed-like NP with an average long axis of 5 ± 1 nm are green-gray.

Predominant vibrational signals were observed in the Raman spectrum of 4-ABT at 1140, 1390 and 1430 cm^{-1}. These signals can be attributed to modes assigned to the 9b, 3 and 19b modes of the b2-type ring, respectively. The low intensity band at 1080 cm^{-1} is due to the 7a mode of the a1-type ring (K. Kim, 2011b; K. Kim, 2011c; K. Kim, 2011d; K. Kim, 2012b; K. Kim, 2012a). The main Raman bands of BPE are observed in SERS spectrum of the probe molecules deposited on Au NPs. The peak at 994 cm^{-1} corresponds to the ring breathing mode of BPE pyridine. A blue shift of 27 cm^{-1} was observed in the SERS spectra of BPE, which includes the vibrational movement of the pyridyl nitrogen atom. Similarly, the vibrational signature observed at 1596 cm^{-1} corresponds to the C–N stretching mode of the pyridyl ring. This band presents a blue shift of approximately 10 cm^{-1} in the SERS spectrum of BPE deposited on Au NPs.

These results suggest that the molecule of BPE interacts strongly with the surface of the Au NPs through the nitrogen atom corresponding to the pyridyl ring (A. Kim, 2011a). However, the bands at 1637 cm^{-1} and 1200 cm^{-1} remain unshifted.

Size distribution of gold and silver nanoparticles was evaluated. The analysis was conducted to verify how the irradiation time during the laser ablation synthesis affected the average size of the NPs. The results are shown in Table 5.1. The average particle size distributions of Au and Ag NPs synthesized by different ablation times are shown. The particles at 5 min are larger (96 nm) than those obtained at 20 min. As the ablation time increases from 5 to 20 min, the size distribution experiences a significant decrease of NP size and the average particle size is reduced to 75 nm. Similar results were obtained by Baladi (Baladi, 2010) in the synthesis of Al nanoparticles (Mahfouz, 2008; Tsuji, 2002).

(**A**) BPE   (**B**) 4-ABT
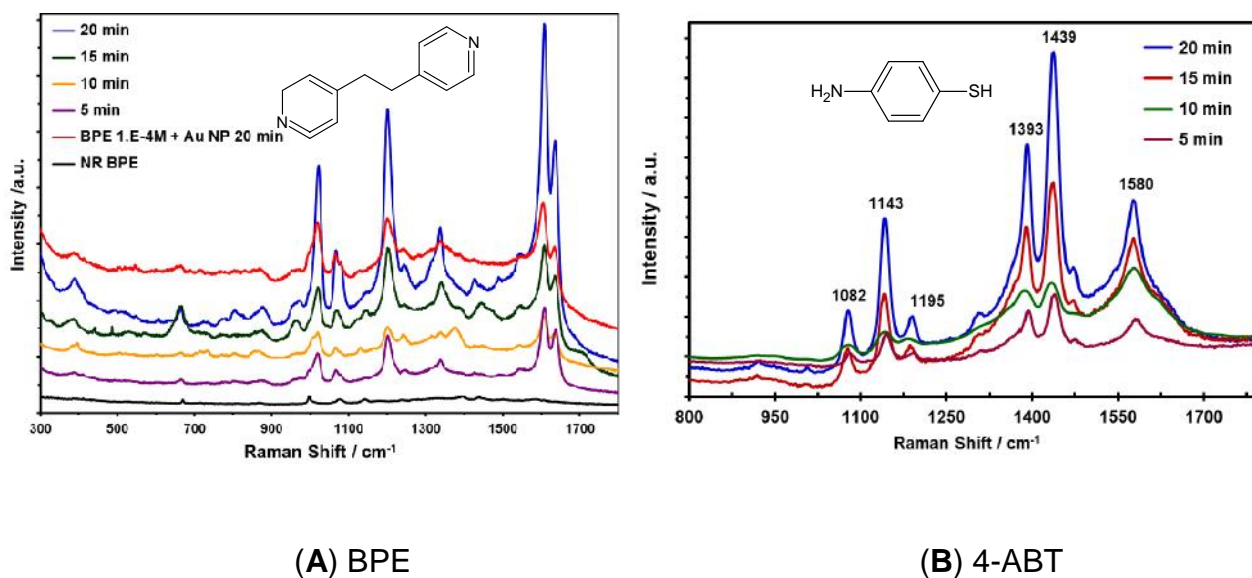
Figure 5.3. Surface enhanced Raman scattering (SERS) spectrum of, (A) 1 mM BPE in Au NPs at various irradiation times. Raman and SERS spectra were acquired at 785 nm, and (B) 1 mM 4-ABT deposited on Ag NPs deposited on Au-coated glass slide at various irradiation times. SERS spectra were acquired at 532 nm.

Table 5.1. Average size of Au and Ag NPs synthesized by laser ablation.

Nanoparticle Type	Irradiation Time (min)	Average Size (Z size, nm)
Au	5	96
Au	10	82
Au	15	71
Au	20	75
Ag	5	77
Ag	20	66

pH plays a very important role in the properties of the NPs (Riabinina, 2012) prepared, including their SERS activity (Cañamares, 2005). A change in the ionic strength in the medium leads to the formation of clusters of particles or even a monolayer of particles on a surface. This conglomeration of NPs leads to changes in their color analogous to the variation in color associated with altering the size or the shape of the particles. When two or more particles stick together, the absorption produced is very similar to that of a single rod-like particle with a larger length (Schatz).

Water at different pH values was used to evaluate the SERS activity of the NPs. The pH of the water was adjusted to 2.6, 4.8, 8.1 and 10.3. The irradiation time used for the syntheses was 20 min. The colors of the NPs in water depend on the pH value. Figure 5.4 contains color micrographs of Au and Ag NPs suspensions synthesized at the various pH values studied. Differences in the predominant colloidal color were found. These color changes can be associated with the average size and the predominant shapes of the NPs in the suspensions.

pH: 2.6   4.8   8.1   10.3
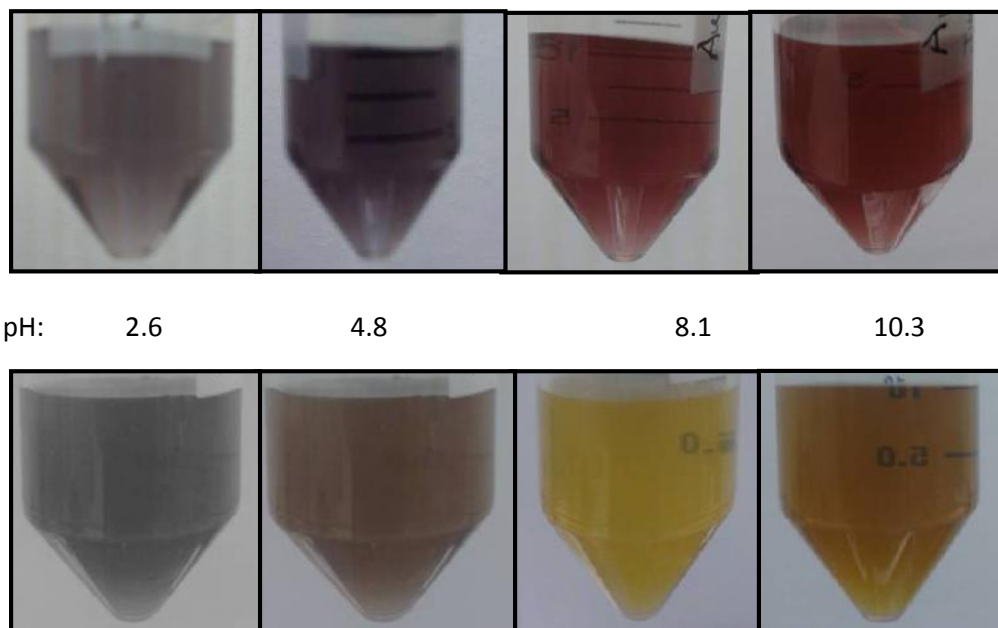
Figure 5.4. NPs suspensions at different pH values of the solvent during synthesis: (A) Au NPs suspensions; and (B) Ag NPs suspensions

Figure 5.5 shows the UV-Vis absorption spectra for Au and Ag nanoparticles synthesized at different pH values. A broad absorption band indicates the presence of different sizes coexisting in the colloidal suspension. At acidic pH values, a low absorbance was found for both Au and Ag NP suspensions. Therefore, at pH values of 8.1 (slightly basic) and 10.3 (basic), intense absorbances were exhibited by the suspensions. No changes in the characteristic wavelength location of the plasmon resonance absorption bands were detected for the metallic NPs under study. Au or Ag NPs suspensions at different pH values were transferred onto gold-coated glass slides to prepare the SERS substrates. Then, the samples were allowed to dry, and 5.0 µL of 1 mM 4-ABT was deposited on the substrates. The SERS measurements were acquired using a Raman excitation source at 532 nm for the analytes deposited on Ag NPs and

82

785 nm for the Au NPs substrates. The results for 4-ABT on Au and Ag NPs are shown in Figure 5.6.

The SERS spectra of 4-ABT on Au NPs shown in Figure 5.6A are in good agreement with previous results [32]. The four strong peaks at 1591, 1436, 1389 and 1143 cm^{-1} can be assigned to ring 8b, 19b, 3 and 9b modes of 4-ABT, respectively. The peaks at Raman shifts of 1491 and 1081 cm^{-1} are due to 8a and 19a modes, respectively, that possess the a1-type of symmetry (K. Kim, 2005; Oliva M. Primera-Pedrozo, 2012). For Au NPs, the best results were found at pH values of 10.3 and 4.8. Kim and collaborators found that the b2-type bands of 4-ABT are strongly affected by the solution pH (K. Kim, 2011b). Regardless of the excitation wavelength and the type of SERS substrates, the b2-type bands appeared very weak or negligible at acidic pH, while they were observed very distinctly at basic pH in Ag NPs. Our results show differences in the signals at 1143 and 1181 cm^{-1} for Au NPs at different pH values. Kim (K. Kim) attributes the disappearance of the b2-type bands at acidic pH to the protonation of the amine group, thus causing the charge transfer resonance chemical enhancement to be less likely to occur.

Likewise, the results for 4-ABT obtained for Ag NPs deposited on Au-coated glass slides presented good enhancement in the Raman signals, specifically the NP suspensions prepared at basic pH. Figure 5.6B shows the Raman signals for 1 mM 4-ABT. To determine the surface enhancement factor (SEF) for 4-ABT, aliquots of 1.0 × 10^{-9} M were deposited on the NP substrates. The deposited sample covered an area of approximately of 0.25 cm^2. If the spot of the laser using an objective of 10× is

approximately 13 µm^2, the number of 4-ABT molecules that were illuminated was calculated to be 1.4×10^5, which represents a SEF of 1.6×10^9.

(**A**) Au   (**B**) Ag
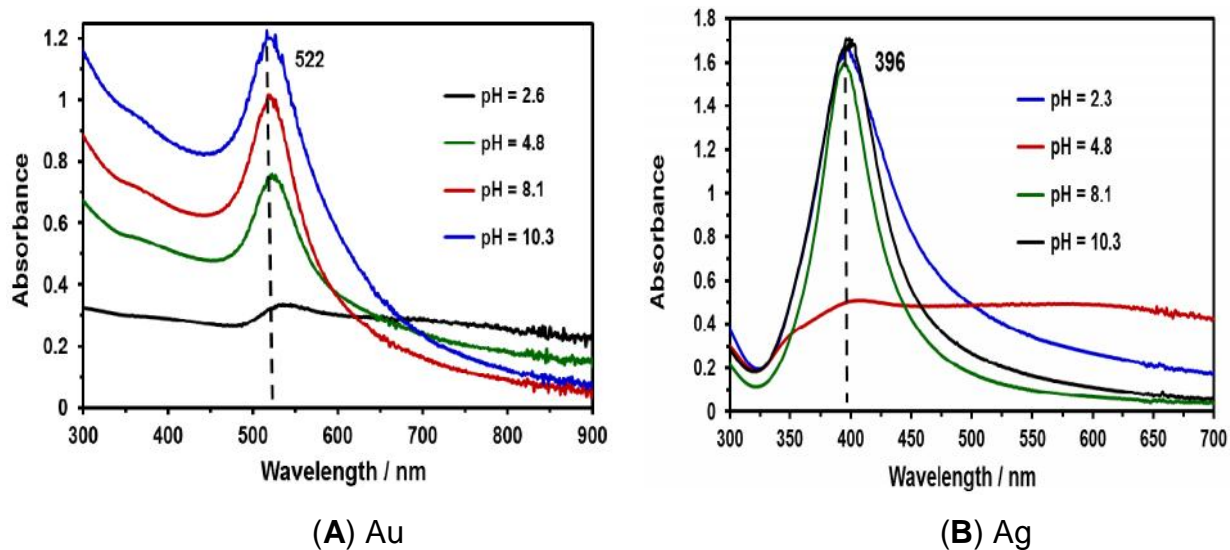
Figure 5.5. UV-Vis absorption spectra of NPs colloids after synthesis at various pH: (A) Au, and (B) Ag.

(A) 4-ABT/AuNP   **(B) 4-ABT/AgNP**

(**C**) TNT/AuNP   (**D**) TNT/Au-COLL
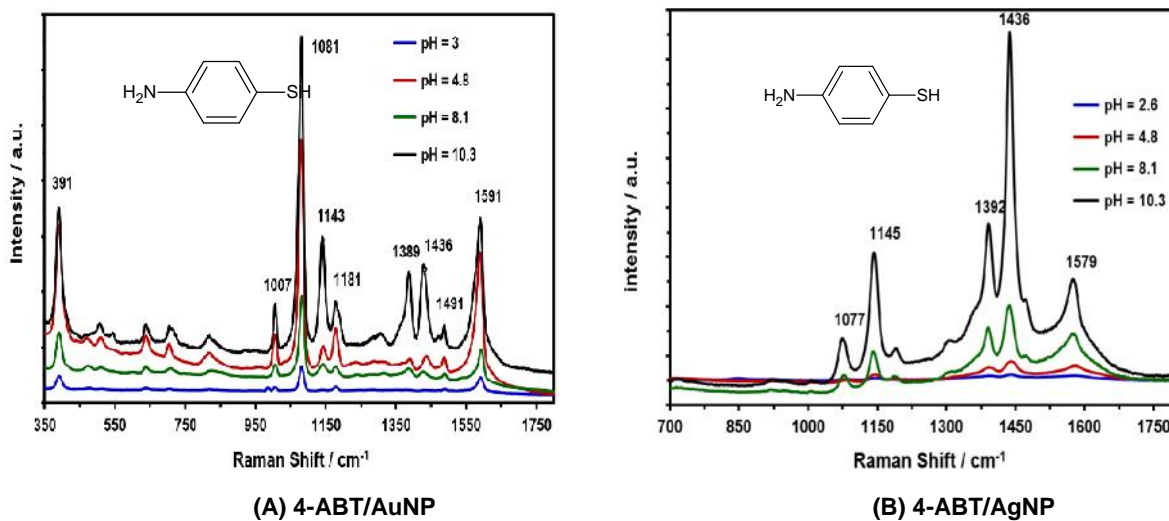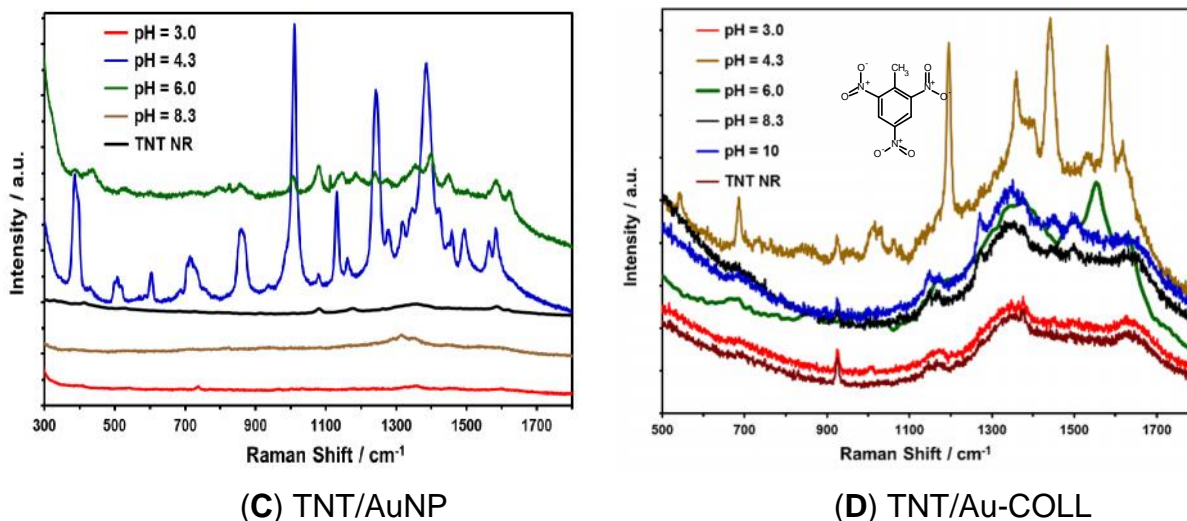
Figure 5.6. pH effect on SERS activity of, (A**) SERS spectra of 4-ABT on the Au NPs/Au substrate, (**B**) SERS spectra of 4-ABT on the Ag NPs/Au substrate, (**C**) TNT SERS spectra on the Au NPs/Au substrate, and (**D**) SERS spectra of TNT interacting with an Au colloidal suspension, included for comparison.**

To determine the effect of pH on Au NPs in SERS activity for the detection of TNT, 3 µL of a solution of the explosive at 1.17 mM was deposited on different Au substrates with gold NPs deposited. The NPs were synthesized at various pH values. The best results were observed at a pH value of nanoparticles of 4.3 and 6.0. The particles obtained at acidic pH (~3) were very unstable for Au NPs. The NPs were precipitated approximately 1 h after preparation. Colloidal results are shown in Figure 5.6D to compare the results of nanoparticles deposited versus colloidal suspensions of nanoparticles. A poor enhancement is observed in the colloidal suspension at pH 4.3.

Results confirm one of the intrinsic limitations of metal colloidal nanoparticles for SERS applications, where their robustness as SERS substrates is compromised. An important factor in the enhancement obtained through SERS is the need for aggregation to generate the necessary plasmonic conditions for the production of significant SERS. If adequate aggregation does not occur, the reproducibility of SERS on colloidal NPs is

affected because the kinetics of the process can be uncontrollable once aggregation begins.

SERS is an important technique to develop applications for the detection of highly energetic materials (HEM) (Caygill, 2012; Fierro-Mercado, 2012; Izake, 2010; Kawaguchi, 2008; Kneipp, 1995; Lin; Liu, 2011; P. Fierro-Mercado, 2012). TNT is a HEM of vast military applications and uses. TNT was selected as a nitroaromatic HEM to evaluate Au NPs on different substrates. Solutions containing TNT were transferred onto various substrates containing Au NPs that were deposited and immobilized. Substrates, such as Al and quartz plates, were also used to deposit Au NPs. TNT solutions at different concentrations (1.0×10^{-4} M, 1.0×10^{-6} M and 1.0×10^{-10} M) were used to determine the lowest amount of HEM that could be quantitatively detected (Low Limit of Detection, LOD). The results shown in Figure 5.7 indicate an increase in the intensity of the principal vibrational signals of TNT due to SERS, which presents strong bands.

(A) (B)
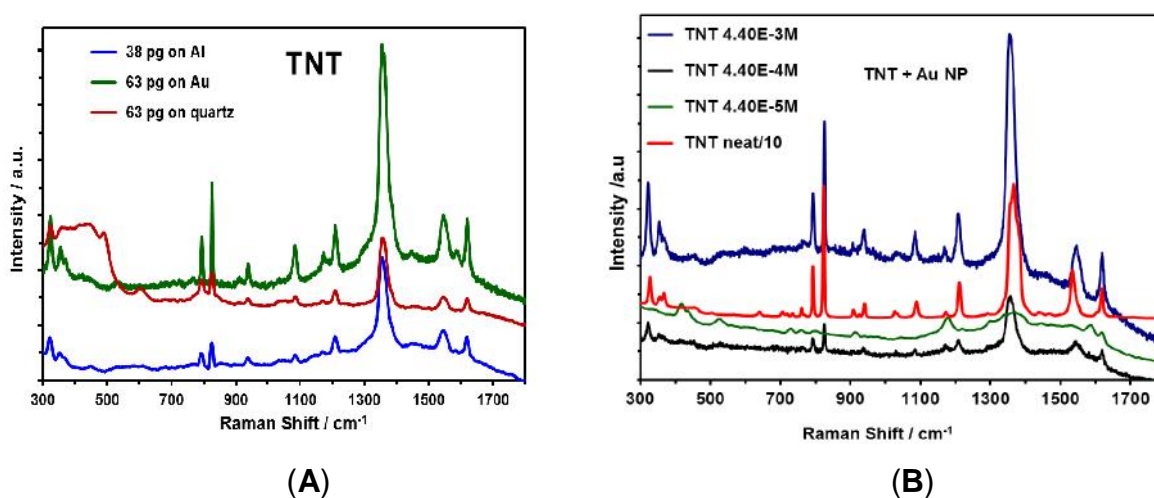
Figure 5.7. SERS spectra of TNT deposited on Au NPs; spectra were taken at 785, (A**) NPs were deposited on different substrates (Al film, Au film and quartz), (**B**) TNT deposited at different concentrations and Al was used as the substrate.**

The signal observed corresponded to the presence of the NO_2 group out-of-plane bending mode at 826 cm^{-1} and the NO_2 stretching mode at 1300–1370 cm^{-1} (Jerez Rozo, 2007). Primera-Pedrozo *et al.* reported similar results in 2008 (O. M. Primera-Pedrozo, 2008), where the enhancement was obtained from colloidal gold NPs with a modification of the ionic strength of the media that was used to interact with the explosive. A SEF of 2×10^9 was obtained for TNT.

The zeta potential of a system is a measure of the charge stability and controls all particle-particle interactions within a suspension. Understanding the zeta potential is of critical importance in controlling the dispersion and determining the stability of a nanoparticle suspension, *i.e.*, to what degree aggregation will occur over time (Cosgrove, 2005). A lower level of the zeta potential results (0 to ±30 mV) in a smaller electrostatic repulsion between the particles, maximizing aggregation/flocculation.

Zeta potential measurements of the as-prepared samples yielded values of –34.9 mV for the Au colloid and –20.9 mV for the Ag colloid, thus confirming the moderate stability of gold and silver nanoparticles. Similarly, the Z-potential and the Z-size were acquired for colloidal suspensions of Ag and Au NPs at different pH values. The results confirm the color differences in the colloidal suspension when the pH was adjusted to the solutions before the synthesis. The results are shown in Table 5.2. The values of the Z potential reflect that the stability of the Au NPs is compromised at different pH values of the synthesis of colloidal suspensions. For this reason, the suspended colloidal NPs result in low reproducibility, lower SEF values and higher LODs.

Moreover, we have determined the number of TNT molecules that were present on the Au NPs for an area of approximately of 1.3×10^7 µm^2 deposited on a substrate.

The interrogation area (circular) or laser spot when using a 20× objective was 2.3×10^3 μm^2. The TNT mass contained in the interrogated area for the highest concentration solution was 7.8×10^{-12} g. The number of TNT molecules that were SERS excited was calculated to be 2.1×10^{10} molecules (1.0×10^{-4} M, 2 µL deposited), 2.1×10^8 molecules (1.0×10^{-6} M, 2 µL) and 2.1×10^4 molecules (1.0×10^{-10} M, 2 µL).

Table 5. 2.   Results of the Z-potential and the Z-size for Au NPs and Ag NPs at various pH values.

NP Type	pH	Average Size (nm)	Z Potential (mV)
Ag	4.2	96	−18.0
Ag	6.0	90	−21.8
Ag	8.3	87	−24.1
Ag	10.0	72	−26.2
Ag	10.8	70	−29.1
Au	4.3	93	−11.1
Au	6.0	75	−39.2
Au	8.3	73	−3.7
Au	10.0	47	−5.2

Data were compared with experiments using colloidal NPs. Raman signals were not observed in colloidal NPs. A possible explanation is that the acquisition of good enhanced Raman signals depends on the reliability and stability of the SERS-active sites (or "hot spots"), which have a large influence on the enhancement of the Raman

signal intensities. However, enhancement in the signals obtained depends significantly on the aggregation of Ag or Au colloids and the analyte used in the analysis. The stability of metal colloids is due to the repulsive forces derived from the charged species on the surface of the colloidal particles, which assume a nonzero effective charge. When these charges are replaced with a neutral adsorbate, aggregation occurs, usually when a ligand has a greater affinity for the metal than that of the surface charged species (Muniz-Miranda, 2007).

5.4 Conclusions

Colloidal suspensions of Ag and Au NPs were successfully synthesized by laser ablation using water as the solvent. Colloids of different colors and sizes were obtained, depending on the time of irradiation in the synthesis and the pH of water. Excellent SERS results were found for Au and Ag NPs deposited on Au films using 4-ABT at a pH value of 10.3.

The potential application of Au and Ag nanoparticles in SERS detection of explosives was evaluated. We have detected 7.8×10^{-18} g of TNT on Au NPs deposited on Al sheets. The SEF obtained establishes the possibility of using the substrates prepared for the detection of contaminants in water, such as nitroaromatic HEM.

representation of the official policies, either expressed or implied, of the U.S. Department of Homeland Security.

References

Albrecht, M., Janke, V., Sievers, S., Siegner, U., Schüler, D., and Heyen, U. (2005), 'Scanning force microspy study of biogenic nanoparticles for medical applications', *J. Magn. Magn. Mater.,* 290–291, Part 1 (0), 269-271.

Baladi, A. and Sarraf Mamoory, R. (2010), 'Investigation of different liquid media and ablation times on pulsed laser ablation synthesis of aluminum nanoparticles', *Appl. Surf. Sci.,* 256 (24), 7559-7564.

Burda, C., Chen, X., Narayanan, R., and El-Sayed, M.A. (2005), 'Chemistry and Properties of Nanocrystals of Different Shapes', *Chem. Rev.,* 105 (4), 1025-1102.

Cañamares, M.V., Garcia-Ramos, J.V., Gómez-Varga, J.D., Domingo, C., and Sanchez-Cortes, S. (2005), 'Comparative Study of the Morphology, Aggregation, Adherence to Glass, and Surface-Enhanced Raman Scattering Activity of Silver Nanoparticles Prepared by Chemical Reduction of Ag+ Using Citrate and Hydroxylamine', *Langmuir,* 21 (18), 8546-8553.

Caygill, J.S., Davis, F., and Higson, S.P.J. (2012), 'Current trends in explosive detection techniques', *Talanta,* 88 (0), 14-29.

Chang, C.-C., Yang, K.-H., Liu, Y.-C., and Hsu, T.-C. (2012), 'New pathway to prepare gold nanoparticles and their applications in catalysis and surface-enhanced Raman scattering', *Colloids Surf., B,* 93 (0), 169-173.

Chen, X. and Schluesener, H.J. (2008), 'Nanosilver: A nanoproduct in medical application', *Toxicol. Lett.,* 176 (1), 1-12.

Chen, X. and Zhu, H. (2011), '3.01 - Catalysis by Supported Gold Nanoparticles', in Editors-in-Chief: David, L.A., Gregory, D.S., and Gary, P.W. (eds.), *Comprehensive Nanoscience and Technology* (Amsterdam: Academic Press), 1-11.

Cosgrove, T. (ed.), (2005), *Colloid Science Principles, Methods and Applications* (Department of Chemistry, University of Bristol, Bristol -UK: Blackwell Publishing Ltd).

El-Rafie, M.H., Shaheen, T.I., Mohamed, A.A., and Hebeish, A. (2012), 'Bio-synthesis and applications of silver nanoparticles onto cotton fabrics', *Carbohydr. Polym.,* 90 (2), 915-920.

Eriksson, S., Nylén, U., Rojas, S., and Boutonnet, M. (2004), 'Preparation of catalysts from microemulsions and their applications in heterogeneous catalysis', *Appl. Catal., A,* 265 (2), 207-219.

Fierro-Mercado, P., Renteria-Beleño, B., and Hernández-Rivera, S.P. (2012), 'Preparation of SERS-active substrates using thermal inkjet technology', *Chem. Phys. Lett.,* 552 (0), 108-113.

Fierro-Mercado, P.M. and Hernandez-Rivera, S.P. (2012), 'Highly Sensitive Filter Paper Substrate for SERS Trace Explosives Detection', *International Journal of Spectroscopy,* 2012, 1-7.

Ganesh, S. and Amit, S. (2006), 'Perspectives on the Science and Technology of Nanoparticle Synthesis', *Nanomaterials Handbook* (CRC Press).

Haibo, Z., Shikuan, Y., and Weiping, C. (2012), 'Formation of Nanoparticles Under Laser Ablation of Solids in Liquids', *Laser Ablation in Liquids* (Pan Stanford Publishing), 327-396.

Hamouda, I.M. (2012), 'Current perspectives of nanoparticles in medical and dental biomaterials', *J. Biomed. Mater. Res.,* 26 (3), 143-151.

Haruta, M. (2003), 'Catalysis and applications of gold nanoparticles', in Masakazu Anpo, M.O. and Hiromi, Y. (eds.), *Studies in Surface Science and Catalysis* (Volume 145: Elsevier), 31-38.

Hou, X., Zhang, X., Chen, S., Fang, Y., Li, N., Zhai, X., and Liu, Y. (2011), 'Size-controlled synthesis of Au nanoparticles and nanowires and their application as SERS substrates', *Colloids Surf., A,* 384 (1–3), 345-351.

Hutchings, G.J. and Edwards, J.K. (2012), 'Chapter 6 - Application of Gold Nanoparticles in Catalysis', in Roy, L.J. and Wilcoxon, J.P. (eds.), *Frontiers of Nanoscience* (Volume 3; Amsterdam, United Kingdom: Elsevier), 249-293.

Izake, E.L. (2010), 'Forensic and homeland security applications of modern portable Raman spectroscopy', *Forensic Sci. Int.,* 202 (1–3), 1-8.

Jerez Rozo, J.I., Chamoun, A.M., Peña, S.L., and Hernández-Rivera, S.P. (2007), 'Enhanced Raman scattering of TNT on nanoparticle substrates: Ag colloids prepared by reduction with hydroxylamine hydrochloride and sodium citrate', *Proc. SPIE 653824* (Sensors, and Command, Control, Communications, and Intelligence (C3I) Technologies for Homeland Security and Homeland Defense VI,; Florida, USA), 653824-653824..

Jung, S.-H., Kim, K.-I., Ryu, J.-H., Choi, S.-H., Kim, J.-B., Moon, J.-H., and Jin, J.-H. (2010), 'Preparation of radioactive core-shell type 198Au@SiO2 nanoparticles as a radiotracer for industrial process applications', *Appl. Radiat. Isot.,* 68 (6), 1025-1029.

Kawaguchi, T., Shankaran, D.R., Kim, S.J., Matsumoto, K., Toko, K., and Miura, N. (2008), 'Surface plasmon resonance immunosensor using Au nanoparticle for detection of TNT', *Sens. Actuators, B,* 133 (2), 467-472.

Kim, A., Ou, F.S., Ohlberg, D.A.A., Hu, M., Williams, R.S., and Li, Z. (2011a), 'Study of Molecular Trapping Inside Gold Nanofinger Arrays on Surface-Enhanced Raman Substrates', *J. Am. Chem. Soc.,* 133 (21), 8234-8239.

Kim, K. 'Surface-Enhanced Raman Scattering Characteristics of 4-Aminobenzenethiol Derivatives Adsorbed on Silver', *http://ipc.iisc.ernet.in/~umalab/icors2012/Mo_109.pdf*.

Kim, K. and Lee, H.S. (2005), 'Effect of Ag and Au Nanoparticles on the SERS of 4-Aminobenzenethiol Assembled on Powdered Copper', *J. Phys. Chem. B,* 109 (40), 18929-18934.

Kim, K., Kim, K.L., Lee, H.B., and Shin, K.S. (2012a), 'Similarity and Dissimilarity in Surface-Enhanced Raman Scattering of 4-Aminobenzenethiol, 4,4´-Dimercaptoazobenzene, and 4,4´-Dimercaptohydrazobenzene on Ag', *The J. Phys. Chem. C,* 116 (21), 11635-11642.

Kim, K., Shin, D., Choi, J.-Y., Kim, K.L., and Shin, K.S. (2011b), 'Surface-Enhanced Raman Scattering Characteristics of 4-Aminobenzenethiol Derivatives Adsorbed on Silver', *J. Phys. Chem. C,* 115 (50), 24960-24966.

Kim, K., Lee, H.B., Choi, J.-Y., Kim, K.L., and Shin, K.S. (2011c), 'Surface-Enhanced Raman Scattering of 4-Aminobenzenethiol in Nanogaps between a Planar Ag Substrate and Pt Nanoparticles', *J. Phys. Chem. C,* 115 (27), 13223-13231.

Kim, K., Yoon, J.K., Lee, H.B., Shin, D., and Shin, K.S. (2011d), 'Surface-Enhanced Raman Scattering of 4-Aminobenzenethiol in Ag Sol: Relative Intensity of a1- and b2-Type Bands Invariant against Aggregation of Ag Nanoparticles', *Langmuir,* 27 (8), 4526-4531.

Kim, K., Kim, K.L., Shin, D., Choi, J.-Y., and Shin, K.S. (2012b), 'Surface-Enhanced Raman Scattering of 4-Aminobenzenethiol on Ag and Au: pH Dependence of b2-Type Bands', *J. Phys. Chem. C,* 116 (7), 4774-4779.

Kneipp, K., Wang, Y., Dasari, R.R., Feld, M.S., Gilbert, B.D., Janni, J., and Steinfeld, J.I. (1995), 'Near-infrared surface-enhanced Raman scattering of trinitrotoluene on colloidal gold and silver', *Spectrochim. Acta, Part A,* 51 (12), 2171-2175.

Kundu, S., Mandal, M., Ghosh, S.K., and Pal, T. (2004), 'Photochemical deposition of SERS active silver nanoparticles on silica gel and their application as catalysts for the reduction of aromatic nitro compounds', *J. Colloid Interface Sci.,* 272 (1), 134-144.

Lawrence, D.Ä. and Ryan, R. (2006), 'Synthesis of Metal Colloids', *Catalyst Preparation* (CRC Press), 93-137.

Lee, K.Y., Hwang, J., Lee, Y.W., Kim, J., and Han, S.W. (2007), 'One-step synthesis of gold nanoparticles using azacryptand and their applications in SERS and catalysis', *J. Colloid Interface Sci.,* 316 (2), 476-481.

Lin, D., Liu, H., Qian, K., Zhou, X., Yang, L., and Liu, J. 'Ultrasensitive optical detection of trinitrotoluene by ethylenediamine-capped gold nanoparticles', *Anal. Chim. Acta,* 744 (0), 92-98.

Liu, X., Zhao, L., Shen, H., Xu, H., and Lu, L. (2011), 'Ordered gold nanoparticle arrays as surface-enhanced Raman spectroscopy substrates for label-free detection of nitroexplosives', *Talanta,* 83 (3), 1023-1029.

López-Tocón, I., Centeno, S.P., Otero, J.C., and Marcos, J.I. (2001), 'Selection rules for the charge transfer enhancement mechanism in SERS: dependence of the intensities on the L-matrix', *J. Mol. Struct.,* 565–566 (0), 369-372.

Luo, Z. and Fang, Y. (2006), 'Investigation of the mechanism of influence of colloidal gold/silver substrates in nonaqueous liquids on the surface enhanced Raman spectroscopy (SERS) of fullerenes C60 (C70)', *J. Colloid Interface Sci.,* 301 (1), 184-192.

Mahfouz, R., Cadete Santos Aires, F.J., Brenier, A., Jacquier, B., and Bertolini, J.C. (2008), 'Synthesis and physico-chemical characteristics of nanosized particles produced by laser ablation of a nickel target in water', *Appl. Surf. Sci.,* 254 (16), 5181-5190.

Muniz-Miranda, M., Pergolese, B., Bigotto, A., and Giusti, A. (2007), 'Stable and efficient silver substrates for SERS spectroscopy', *J. Colloid Interface Sci.,* 314 (2), 540-544.

Niu, Y. and Crooks, R.M. (2003), 'Dendrimer-encapsulated metal nanoparticles and their applications to catalysis', *C.R. Chim.,* 6 (8–10), 1049-1059.

Photopoulos, P., Boukos, N., Panagopoulou, M., Meintanis, N., Pantiskos, N., Raptis, Y., and Tsoukalas, D. (2011), 'Size control of Ag nanoparticles for SERS sensing applications', *Procedia Eng.,* 25 (0), 280-283.

Piao, M.J., Kang, K.A., Lee, I.K., Kim, H.S., Kim, S., Choi, J.Y., Choi, J., and Hyun, J.W. (2011), 'Silver nanoparticles induce oxidative cell damage in human liver cells through inhibition of reduced glutathione and induction of mitochondria-involved apoptosis', *Toxicol. Lett.,* 201 (1), 92-100.

Primera-Pedrozo, O.M., Jerez-Rozo, J.I., De La Cruz-Montoya, E., Luna-Pineda, T., Pacheco-Londono, L.C., and Hernandez-Rivera, S.P. (2008), 'Nanotechnology-Based Detection of Explosives and Biological Agents Simulants', *Sensors Journal, IEEE,* 8 (6), 963-973.

Primera-Pedrozo, O.M., Rodríguez, G.D.M., Castellanos, J., Felix-Rivera, H., Resto, O., and Hernández-Rivera, S.P. (2012), 'Increasing surface enhanced Raman spectroscopy effect of RNA and DNA components by changing the pH of silver colloidal suspensions', *Spectrochim. Acta, Part A,* 87 (0), 77-85.

Rai, M., Yadav, A., and Gade, A. (2009), 'Silver nanoparticles as a new generation of antimicrobials', *Biotechnol. Adv.,* 27 (1), 76-83.

Riabinina, D., Zhang, J., Chaker, M., Margot, J., and Ma, D. (2012), 'Size Control of Gold Nanoparticles Synthesized by Laser Ablation in Liquid Media', *ISRN Nanotechnology,* 2012, 5.

Schatz, S.H.a.G. 'Synthesis and Analysis of Silver/Gold Nanoparticles', *http://nanohub.org/topics/GeneralChemistry/File:Silvergold_module.pdf*.

Sergeev, G.B. (2006), 'Synthesis and Stabilization of Nanoparticles', *Nanochemistry* (Amsterdam: Elsevier Science), 7-36.

Stratakisa, E. and Shafeevb, G. (2012), 'Nanostructures? Formation Under Laser Ablation of Solids in Liquids', *Laser Ablation in Liquids* (Pan Stanford Publishing), 815-854.

Takeshi, T. (2012), 'Preparation of Nanoparticles Using Laser Ablation in Liquids', *Laser Ablation in Liquids* (Pan Stanford Publishing), 207-268.

Tsuji, T., Iryo, K., Watanabe, N., and Tsuji, M. (2002), 'Preparation of silver nanoparticles by laser ablation in solution: influence of laser wavelength on particle size', *Appl. Surf. Sci.,* 202 (1–2), 80-85.

Vlckova, B., Pavel, I., Sladkova, M., Siskova, K., and Slouf, M. (2007), 'Single molecule SERS: Perspectives of analytical applications', *J. Mol. Struct.,* 834–836 (0), 42-47.

Wei, D., Ye, Y., Jia, X., Yuan, C., and Qian, W. (2010), 'Chitosan as an active support for assembly of metal nanoparticles and application of the resultant bioconjugates in catalysis', *Carbohydr. Res.,* 345 (1), 74-81.

Yang, J. and Pan, J. (2012), 'Hydrothermal synthesis of silver nanoparticles by sodium alginate and their applications in surface-enhanced Raman scattering and catalysis', *Acta Mater.,* 60 (12), 4753-4758.

Yu, C.H., Oduro, W., Tam, K., and Tsang, E.S.C. (2008), 'Chapter 10 Some Applications of Nanoparticles', in John, A.B. (ed.), *Handbook of Metal Physics* (Volume 5: Elsevier), 365-380.

Chapter 6

Concluding Remarks

The objective of this work was to contribute to the development of new nanomaterials with important applications in the photodegradation of pollutants in water and detection of these contaminants.

Magnetite, hematite, and Au/magnetite were synthesized through a simple hydrothermal method. All oxides were characterized to determine the phase present. In the XRD results, the use of data base in the equipment was helpful in determining that R-Fe_2O_3 principally presents the hematite phase, meanwhile B-Fe_3O_4 exhibited characteristic magnetite x-ray reflections. Magnetic and vibrational properties, pore size and particle size were also determined.

In the evaluation of the MB catalytic activity, degradation was detected at approximately one hour of UV light exposure. Similarly, a decrease of more than 90% in the original concentration of ONP was observed. This indicates that B-Fe_3O_4 and Au/Fe_3O_4 can be used as photocatalyst to assist in removing contaminants from water. Then, using the magnetic properties the oxides could be easily removed from the reaction media.

Parameters such as pH, addition of H_2O_2, irradiation wavelength were studied. An evaluation of TNT degradation at three pH values (pH = 4, 7, 9) was carried out. TNT degradation showed a 46% degradation when the process was carried out at pH = 9 during 3 h of irradiation. The explanation can be attributed to an enhanced number of

OH$^-$ ions and as consequence the ·OH radicals increased. Similarly, the addition of a strong oxidant agent as H$_2$O$_2$ decreased degradation time to nearly half of its value.

In a report filed in 1995, the Agency for Toxic Substances and Disease Registry estimated that the amount of TNT effluent reaching the production/manufacturing, loading, assemble, and finally use and disposition of TNT is about 25-120 mg/L. The samples concentration used for this work that were subjected to a photodegradation process were at a concentration of 25 mg/L. This concentration is within the parameters that we can find in a waste water effluent. This also indicates that magnetite is a possible candidate for the treatment of waste waters.

A new nanocomposite was prepared from extruded polystyrene and titanium dioxide (EPS/TiO$_2$) by synthesizing from recycled polymer sources. The EPS/TiO$_2$ nanocomposite presented high discoloration efficiency for aqueous MB solutions. The percent of discoloration reached 98% in the MB solutions. Better results were obtained for the new nanocomposite than for the commercially available. Thus, EPS/TiO$_2$ will be used in future degradation tests of persistent organic pollutants that occur in water. Another important advantage encountered in the preparation of the nanocomposite (expanded polystyrene–TiO$_2$) is that the polymer permits an easier recuperation process after photodegradation.

Colloidal suspensions of Ag and Au NPs were successfully synthesized by laser ablation using water as solvent. Colloids of different colors and sizes were obtained, depending on the time of irradiation of the synthesis and the pH of the media. Excellent SERS results were found in terms of Raman signal enhancements for Au and Ag NPs

deposited on Au films using 4-ABT at a pH of 10.3. The results also demonstrated the importance the pH during the synthesis of NPs, affecting the size and stability of NPs.

The potential application of Au and Ag nanoparticles in SERS detection of explosives was evaluated. An LOD of 7.8×10^{-18} g of TNT on Au NPs deposited on Al plates was achieved. These results indicate the possibility of using these nanoparticles for detecting analytes in water at trace level. Additionally, a SEF value of 2×10^9 was obtained supporting the possibility of using the substrates prepared for the detection of contaminants in water, such as nitroaromatic explosives.

APPENDIX A

A.1 Internship

As part of Applied Chemistry Doctoral Program at the Chemistry Department of the University of Puerto Rico-Mayagüez every student is required to spend one semester or two summers doing a research internship in an industrial site, academic lab or National Lab outside the UPRM campus. The objective of this experience is increase the student's knowledge and skills in the chosen area of specialty and developing their communication and research skills through exposure to multiple research groups (De Jesus, 2012).

The internship work was carried out at the University of Turabo, Ana G. Méndez Foundation University System, under the direction of Dr. Francisco Márquez and consisted in preparing and characterizing ordered arrays of devices with different materials based primarily magnetite at the nano scale. Important applications were explored such as to heterogeneous photocatalysis and study the functionality of nanostructures by adhesion or encapsulation of organic molecules to the magnetic guidance to biological targets and for the detection and localization of biomarkers.

The potential application of hollow magnetite nanospheres and microspheres was evaluated and a paper concerning their applications as drug carriers was published in Nanoscale Research Letters (Marquez, 2012). A summary of work is presented below.

A.2 Preparation of hollow magnetite microspheres and their applications as drugs carriers

Abstract

Hollow magnetite microspheres have been synthesized by a simple process through a template-free hydrothermal approach. Hollow microspheres were surface modified by coating with a silica nanolayer. Pristine and modified hollow microparticles were characterized by field-emission electron microscopy, transmission electron microscopy, X-ray diffraction, X-ray photoelectron spectroscopy, FT-IR and Raman spectroscopy, and VSM magnetometry. The potential application of the modified hollow magnetite microspheres as a drug carrier was evaluated by using Rhodamine B and methotrexate as model drugs. The loading and release kinetics of both molecules showed a clear pH and temperature dependent profile.

A.2.1 Synthesis of hollow magnetic Fe$_3$O$_4$ microspheres

For a typical synthesis, 2 mmol of FeCl$_3$ were dissolved in 10 mL of propylene glycol; the solution was magnetically stirred at room temperature for 10 min followed by soft ultrasonic treatment for 5 min. Next, 1 mmol of ferrocene was added, and the solution was stirred at room temperature for 2 h. Finally, 3 mL of diethyl amine were added to the mixture. The solution was placed into the Teflon-lined stainless steel autoclave of 30 mL capacity and maintained at 180°C for 24 h. Lower synthesis temperatures (100 to 150°C) were tested although the synthesized hollow magnetite microspheres were not stable, and the degradation was produced in a few days,

generating compact magnetite nanoparticles of no more than 10 nm diameter. Use of $FeCl_3$ /ferrocene as precursor is required to induce a faster self-assembling of nanoparticles into hollow microspheres. After cooling to room temperature, the black sediment is collected and washed in water by five centrifugation (6,000 rpm, 10 min) re-dispersion cycles. Next, the black sediment was resuspended in ethanol and washed by two centrifugation (6,000 rpm, 5 min)-re-dispersion cycles. Finally, the microspheres were suspended in ethanol and dried overnight at 60°C. Hollow Fe_3O_4 microspheres were maintained in sealed containers before characterization.

A.2.2 Preparation of magnetic SiO_2@Fe_3O_4 microspheres

The schematic procedure used to synthesize SiO_2@Fe_3O_4 hybrid hollow microspheres is illustrated in Figure 2, and the detailed synthesis is described as follows. The silica shell has been prepared by using a modified Stobe-Fink-Bohn method [33,34], which consists of two steps: (i) the hydrolysis of TEOS ($Si(C_2H_5O)_4$) in ethanol, in presence of ammonium hydroxide as catalyst, and (ii) the polymerization phase, where the siloxane (Si-O-Si) bonds are formed and anchored on the hollow magnetite surface. In a typical synthesis, 50 mg of hollow Fe_3O_4 microspheres were added to 20 mL of ethanol. The mixture was homogenized in an ultrasound bath for 10 min. Next, 0.5 mL of deionized water and 0.5 mL of ammonium hydroxide (36%) were added into the flask under vigorous mechanical stirring to prevent particles from settling. The temperature was controlled at 20 °C for at least 20 min, and after this period, 0.5 mL of TEOS was added dropwise to the reaction mixture over the course of 5 min under constant stirring in fume hood. After addition, reaction mixture was vigorously stirred for 30 min. Next, the solvent of the reaction mixture is evaporated at 60 °C overnight. The

residue is washed twice in distilled water and finally in ethanol and allowed to dry in vacuum at room temperature.

A.2.3 Encapsulation efficacy within hollow microparticles

To evaluate the potential application of these hollow spheres as drug carriers, three different infiltrations of an organic compound were tested. Rhodamine B, Rh-B, was chosen as test molecule for different reasons. First of all, the size of this molecule is not too small (as occurs with the most of drugs used for therapeutic treatments). On the other hand, this compound is soluble in polar solvents and shows a very high fluorescence quantum yield that can be useful to evidence the presence of very low amounts of this compound, even at trace levels. In this way, Rh-B at three different concentrations (0.05, 0.1, and 0.2 mg/mL) in ethanol were prepared. The infiltration consisted in adding the appropriate amount of Rh-B solution into an Erlenmeyer flask containing 5 mg of hollow particles. This mix was mechanically stirred, and the result for each Rh-B concentration was evaluated at different time period, namely 1, 2, 4, 6, 8, 9, and 12 h. These infiltrations were developed at 20 °C and 40 °C. After infiltration, the particles were centrifuged (1,000 rpm, 5 min) and washed three times with MilliQ water. The particles loads with Rh-B were dried overnight at 60 °C. To determine the amount of Rh-B storage in the hollow microspheres, thermogravimetry (TG) was employed to directly measure the weight loss of as-prepared product. The release kinetics was studied in aqueous solution by controlling the pH and temperature of the solvent by the dialysis bag method. The dialysis bag was soaked in water for 3 h before use. The dialysis bag retained the magnetite microspheres allowing free Rh-B to diffuse into the

solution of study. To monitor the Rh-B release by pH and temperature effect, solutions at different times were analyzed by fluorescence spectroscopy. The pH of solution was adjusted using acetate 0.01 M (pH =3.7) and phosphate 0.01 M (pH = 7.4) buffers. All load and release tests developed on Rh-B were also tested on methotrexate, MTX, a drug used in some cancer treatments.

A.3 Results and discussion

A.3.1 Characterization of magnetite microspheres

Figure A.1 gives the representative FE-SEM micrographs of as-synthesized magnetite microspheres. As can be seen there, these microparticles are very regular in size with diameters of ca. 300 nm and high sphericity. Figure A.1c-d shows some broken spheres confirming that these particles have a hollow interior. In all cases, magnetite microspheres show a mean inner hole of around 160 nm and wall thicknesses of ca. 80 nm. As stated in a previous work, these dimensions are directly related to the synthesis temperature and time of growth [20]. In our research, it was found that the hydrothermal synthesis at 180°C and 24 h provided the best results. Additionally, magnetite microspheres obtained under these reaction conditions showed high stability even in water solution. These structures have been further investigated by TEM. Figure 4 shows the morphological characterization of magnetite microspheres obtained after different growth steps. As can be seen, the size of the spheres increases from diameters around 200 nm in initial growth steps (Figure A.2) to ca. 300 nm (after 24 h). Figure A.2 a,b shows that these spheres are built from smaller building blocks of no more than 5-8 nm assembled together to form the shell wall. The final structures,

synthesized after a reaction time of 24 h, show a homogeneous surface with constant dimensions. The contrast between the black margin and the clear center of the microparticles confirms the existence of hollow spheres, according to the FE-SEM observations. Additionally, the corresponding selected area electron diffraction (SAED) (Figure A.2e) taken from an individual hollow microsphere, as shown in Figure A.1d (marked by a rectangle), reveals the crystalline nature of the material.

Characterization of material was carried out and results were discussed in the article; but in this appendix do not detail the results concerning the characterization. For more information refer to the publication launched in Nanoscale Research Letters (Marquez, 2012).

Figure 3 FE-SEM images of the as-synthesized hollow magnetite microspheres obtained at different magnification
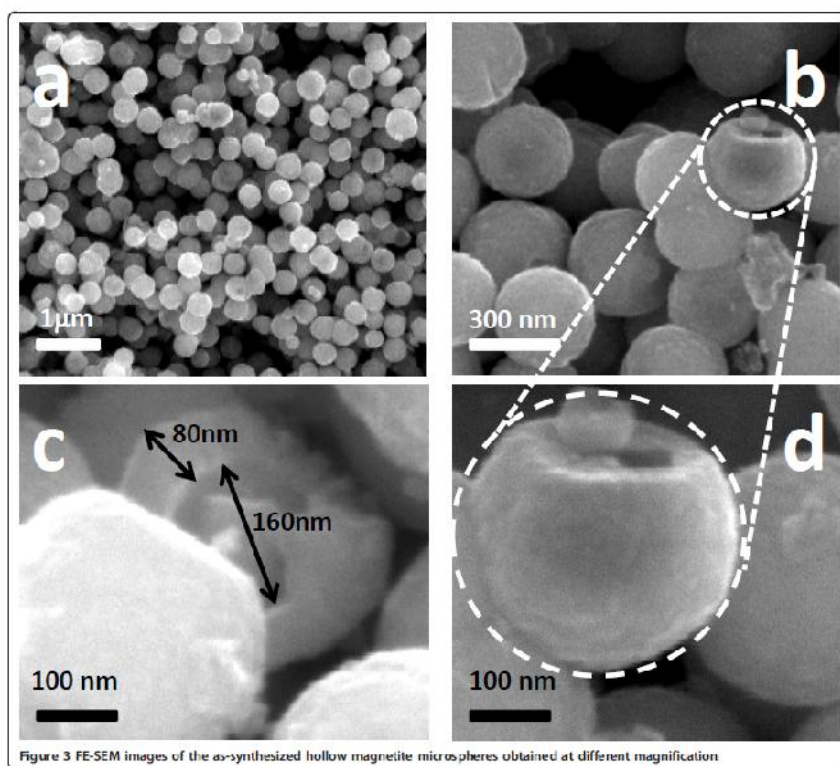
Figure A.1. FE-SEM images of the as-synthesized hollow magnetite microspheres obtained at different magnification.

A.3.2 Loading and release of test molecules

To investigate hollow magnetite microspheres as a candidate of drug carriers for delivery, we selected Rh-B and MTX as models. MTX is a well-known chemotherapy drug used in treating certain types of cancer. Figure A.3 shows the loading of Rh-B in SiO2@hollow magnetite microspheres at different Rh-B concentrations (0.05, 0.1, and 0.2 mg/mL) and temperatures (20 °C and 40 °C). As expected, the microspheres show distinctly different loading capacity toward Rh-B at different temperatures. As can be seen, the highest loading capacity is observed at higher temperature (40 °C) and clearly depends on the initial Rh-B concentration. As determined by TG, the loading of Rh-B in SiO_2@hollow magnetite microspheres is ca. 0.413 mg Rh-B/mg MP at 40 °C and after contact times of 9 h. The release behavior of Rh-B from SiO_2@hollow magnetite microspheres was examined in buffered solutions at pH = 3.7 and 7.4, and the results are shown in Figure A.4. As can be seen there, the higher release values are observed near to physiological conditions in the human body (pH = 7.4 and 37 °C). Releasing of Rh-B from the host is produced in a short period of time, typically during the first hour and clearly depends on pH and temperature.

Figure 4 TEM Images of the hollow magnetite microspheres obtained at different reaction times. TEM Images of the hollow magnetite microspheres obtained at different reaction times: 8 h (a), 16 h (b) and 24 h (c, d). Figure 4e corresponds to the SAED pattern of the boxed region shown in image d.
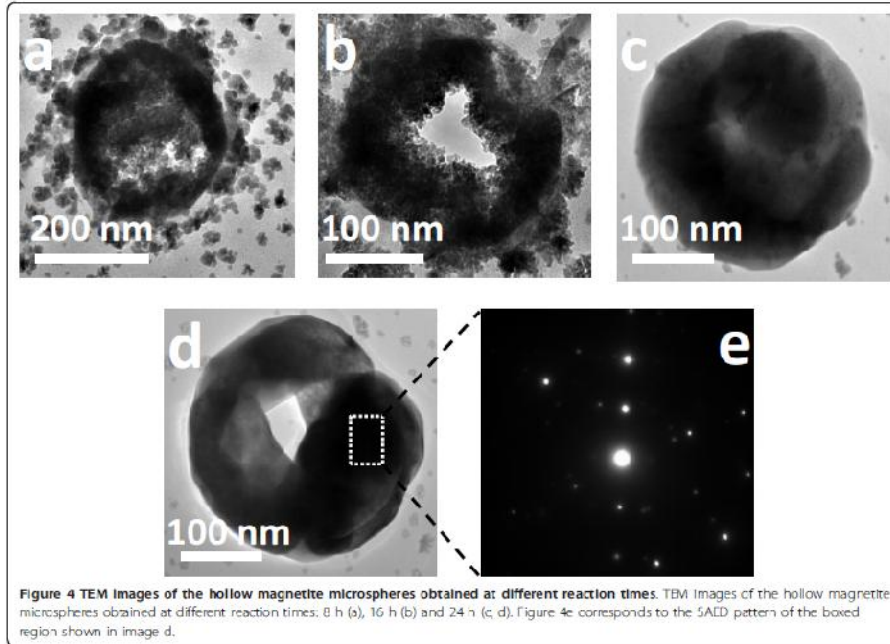
Figure A. 2Tem images of the hollow magnetite microspheres at different reaction times. TEM images of the hollow magnetite microspheres obtained at different reaction times: 8 h (a), 16 h (b) and 24 h (c, d). Figure A.2e corresponds to the SAED pattern of the boxed region shown in image d.

Figure 11 Loading kinetics of Rh-B in SiO$_2$@hollow magnetite microspheres at different Rh-B concentrations and temperatures.
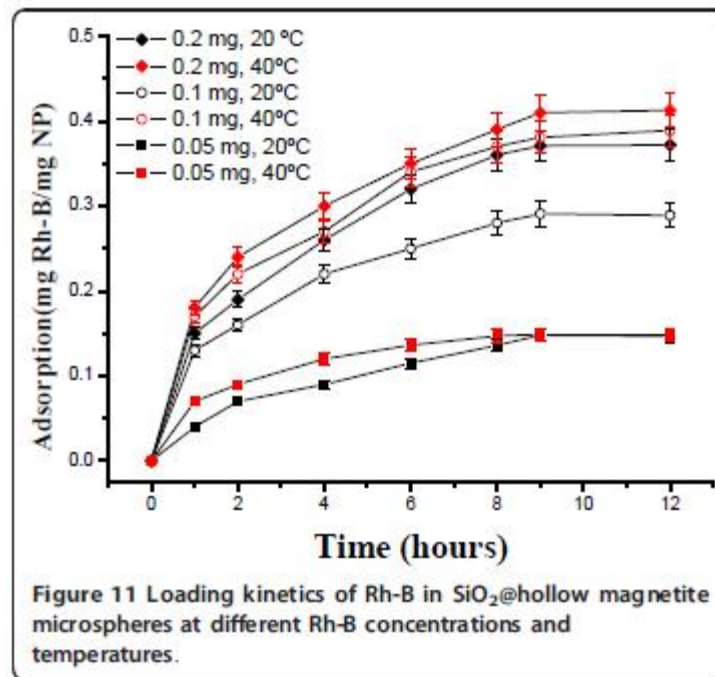
Figure A. 3. Loading kinetics of Rh-B in SiO$_2$@hollow magnetite microspheres at different Rh-B concentrations and temperatures.

106

Figure 12 Release kinetics of Rh-B incorporated within SiO$_2$@hollow magnetite microspheres at different pH and temperatures.
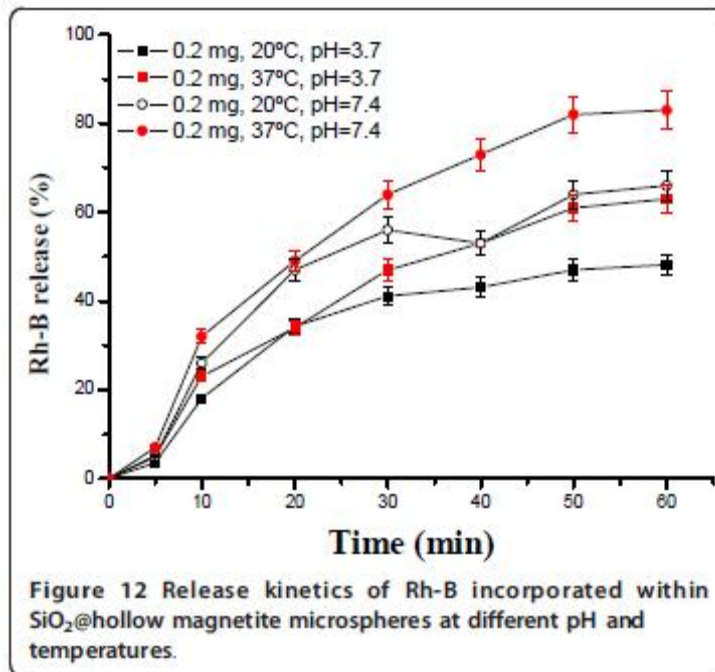
Figure A. 4Release kinetics of Rh-B incorporated within SiO$_2$@hollow magnetite microspheres at different pH and temperatures.

In a similar way, we examined the loading and release kinetics of MTX in SiO$_2$@hollow magnetite microspheres.

As shown in Figure A.6, the loading of MTX depends on the temperature, and the maximum value is observed after 9 h of contact time (0.343 g MTX/ mg MP at 40°C). The decrease of MTX loading in SiO$_2$@hollow magnetite microspheres, as compared with loadings of Rh-B, can be ascribed to the reduced solubility of MTX in water. Nevertheless, the loadings of MTX were surprisingly higher than those expected, exceeding our expectations. The release kinetic of MTX was studied after incubating in phosphate (pH = 7.4) and acetate (pH = 3.7) buffer solutions at two different temperatures (20°C and 37° C). As shown in Figure A.7, MTX was released more rapidly (typically during the first 60 min) at pH = 7.4 and 37 °C). These results show that within the first hour almost 70% of MTX was released from the microparticles, and the

remaining drug was slowly released in a sustained fashion over a period of 5 h (not shown). Such long stability and delay of MTX could be due to favorable ionic interactions between amino and carboxylic groups of MTX and the surface of the magnetite nanoparticles forming the hollow microparticles. Additional work is currently in progress to provide answers to these outstanding issues.


Figure 13 Loading kinetics of MTX in SiO₂@hollow magnetite microspheres at 20°C and 40°C.
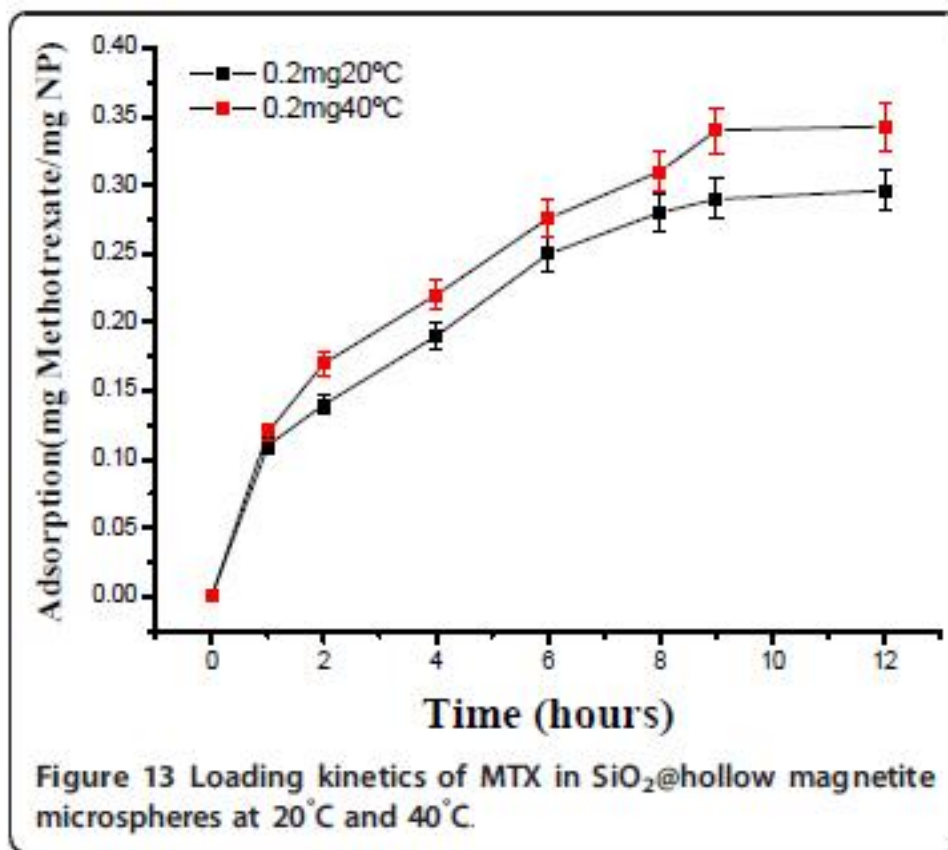
Figure A. 5. Loading kinetics of MTX in SiO_2@hollow magnetite microspheres at 20°C and 40°C.

Figure 14 Release kinetics of MTX incorporated within SiO₂@hollow magnetite microspheres at different pH and temperatures.
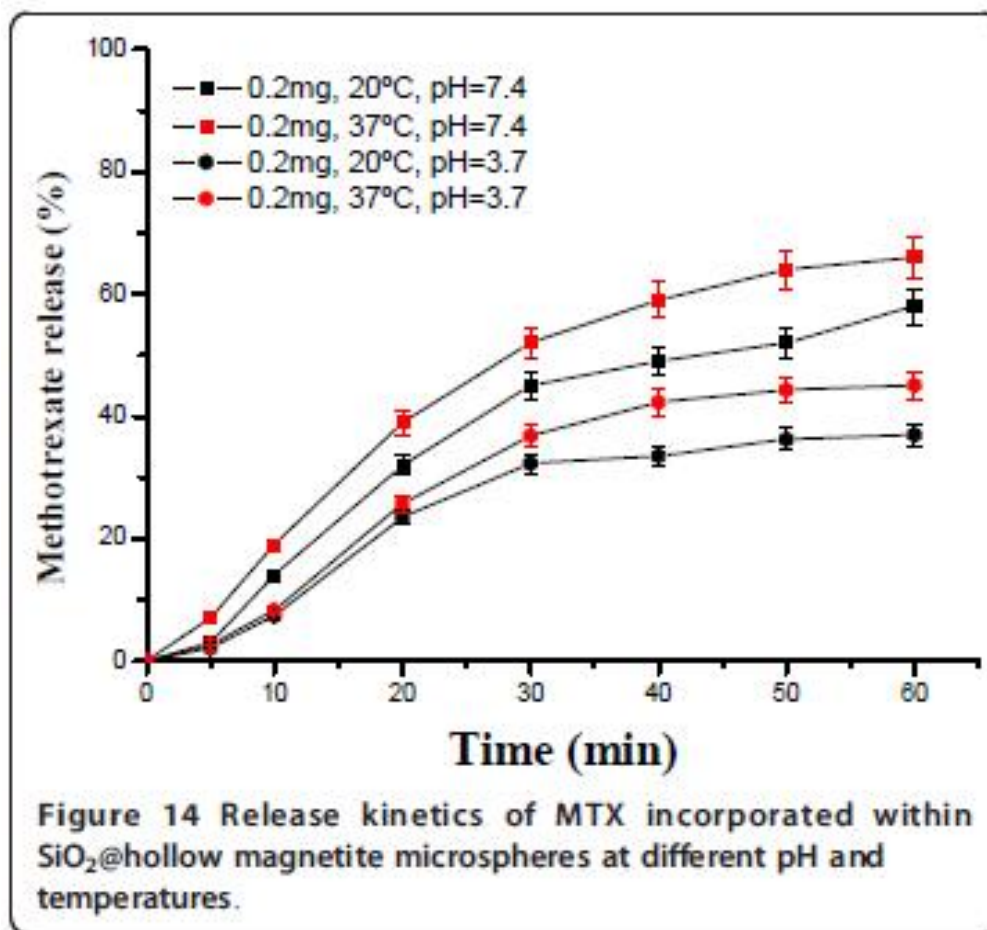
Figure A.6 Release kinetics of M TX incorporated within SiO$_2$@hollow magnetite microspheres at different pH and temperatures.

A.4 Conclusion

In the present work, we have synthesized hollow magnetite microspheres by a simple one-step hydrothermal procedure. With the aim to increase the solubility in polar solvents, these microspheres were subsequently surface modified by growing a silica nanolayer via sol gel process. The potential application of the modified hollow magnetite microspheres as a drug carrier was evaluated by using Rh-B and MTX as model drugs. The loading and release kinetics of both molecules experienced a pH and temperature

dependent profile. It is expected that this dependency could be modified and selected

for specific functions, opening up promising applications in biomedical fields.

References

De Jesus, M. (2012), 'Graduate Student Guide to the Graduate Program in Applied Chemistry'.

Marquez, F., Herrera, G., Campo, T., Cotto, M., Duconge, J., Sanz, J., Elizalde, E., Perales, O., and Morant, C. (2012), 'Preparation of hollow magnetite microspheres and their applications as drugs carriers', *Nanoscale Res. Lett.,* 7 (1), 210.

APPENDIX B

Degradation Products of TNT

B.1 Methodology

The identification of TNT degradation products was carried out with an Agilent 6890 GC coupled to a Hewlett-Packard HP 5972A mass selective detector (GC/MSD). Electron impact energy of 70 eV was used to generate ions in an ionization chamber at a temperature of 280°C.

The injection conditions were: 150 °C, with splitless mode. An inlet liner of 78.5 mm long and an outer diameter (O.D.) of 6.5 mm and internal diameter (I.D.) of 2.0 mm obtained from Sigma-Aldrich-Supelco (Bellefonte, PA) was used for direct injection. A capillary column of 15.0 m × 0.25 mm (ID) × 0.25 μm film thickness bonded and cross linked with 5% phenyl methylsiloxane (Agilent Technologies) was used. The GC oven program used was: 80 °C at 0.0 min, then 10 °C/min to 230 °C for 17.5 min. Helium gas was used as carrier gas using a flow rate 2.5 mL/min. The mass spectrometer scan mode used a mass range of 35-350 amu. A quadrupole mass selector with a HP-Chem program, Enhanced Chemstation™, version 4.03.00-1996 was employed in the analysis. The NIST Registry of Mass Spectra Edition was used for identification of the peaks in the chromatograms.

The extraction of TNT from aqueous samples was carried out using the method of immersion mode solid phase microextraction, I-SPME (Baez, 2006; Bowen, 2006). Previously, in the work realized by Baez, et al. (Baez-Angarita, 2005) SPME fibers were tested to analyze the most common explosives

including nitroaromatics, nitramines and nitroesters. The nitroesters family showed the best affinity for PDMS/DVB. For this reason PDMS/DVB was chosen (Sigma-Aldrich-Supelco, Bellefonte, PA) fiber for this work. The procedure of extraction was as follows: the sample was placed in 2 mL vials containing 1.0 mL of aqueous solution of TNT (see Figure B.1). Fibers were introduced into the vial and placed in mode immersion inside the sample. The extraction time was fixed at 30 min. These samples remained at constant agitation during test period. Desorption time on the GC/MSD inlet port was 5 min. To test for reproducibility, samples were run in triplicate. The analysis of samples was only qualitative and intended to identify the photodegradation products of TNT.
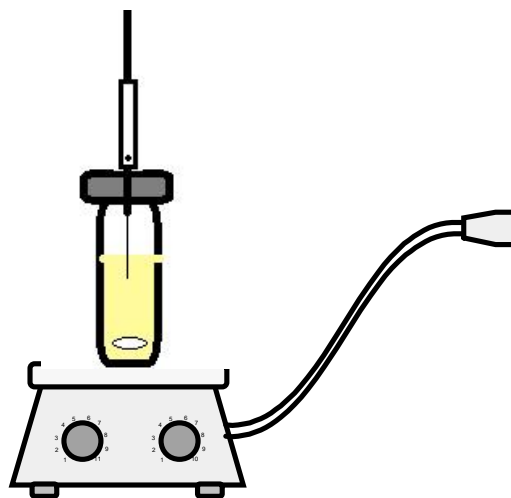
Figure B.1. Scheme of the methodology for I-SPME extraction of TNT from aqueous solution.

B.1 Results

Samples obtained from heterogeneous photodegradation described in Chapters 2 and 3 were used to extract TNT using I-SPME methodology. A sample of TNT at 0 h of UV irradiation was injected in the GC/MSD. This served

112

as baseline measurement. A sample of TNT solution was irradiated a 254 nm without catalyst and used as control.
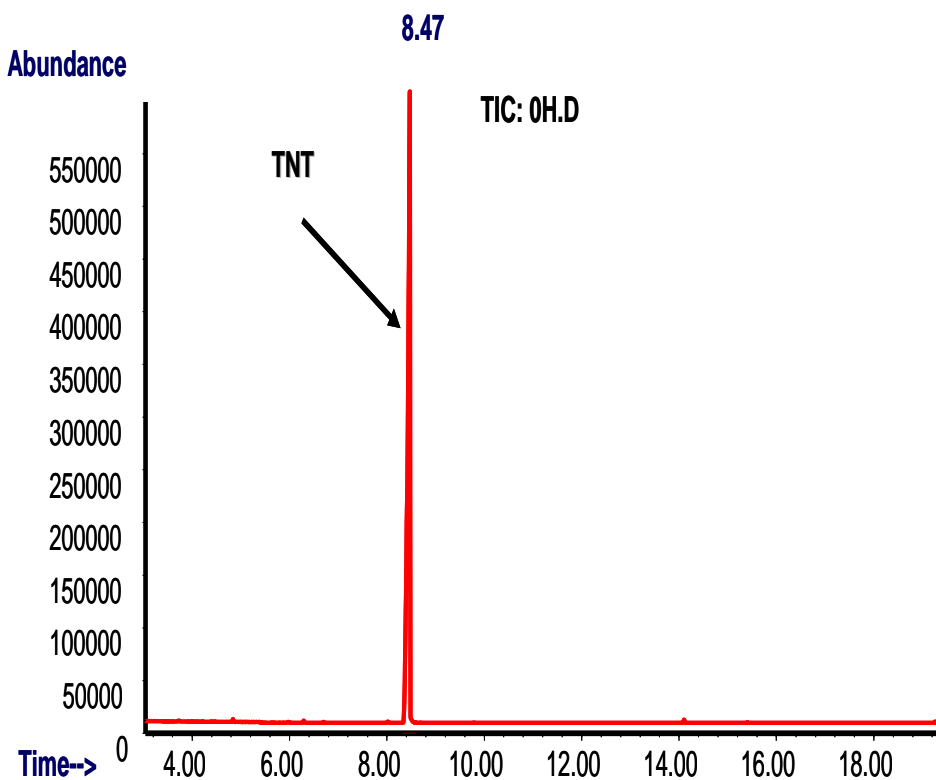

Figure B.2. TNT chromatogram at 0 h of irradiation (with 254 nm UV light).

The results reveal that TNT presented 39% of degradation at 48 h of irradiation without presence of iron oxide as catalyst. Figure B.3 display the results of degradation of TNT during the 48 h of analysis. Photodegradation products are shown in Table B.1. Ion chromatograms of different degradation products of TNT are presented in Figures B.4 to B.7.
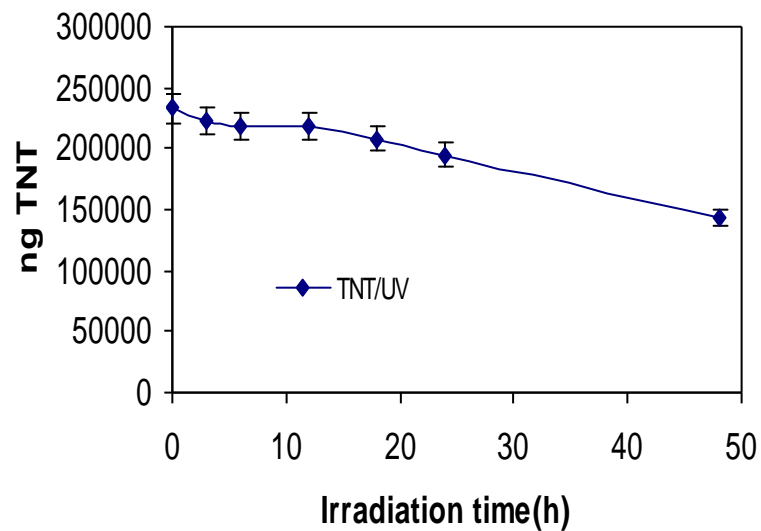
Figure B.3. TNT Photodegradation by photocatalysis process. Irradiation with 254 nm UV light during 48 h. TNT without presence of photocatalyst.
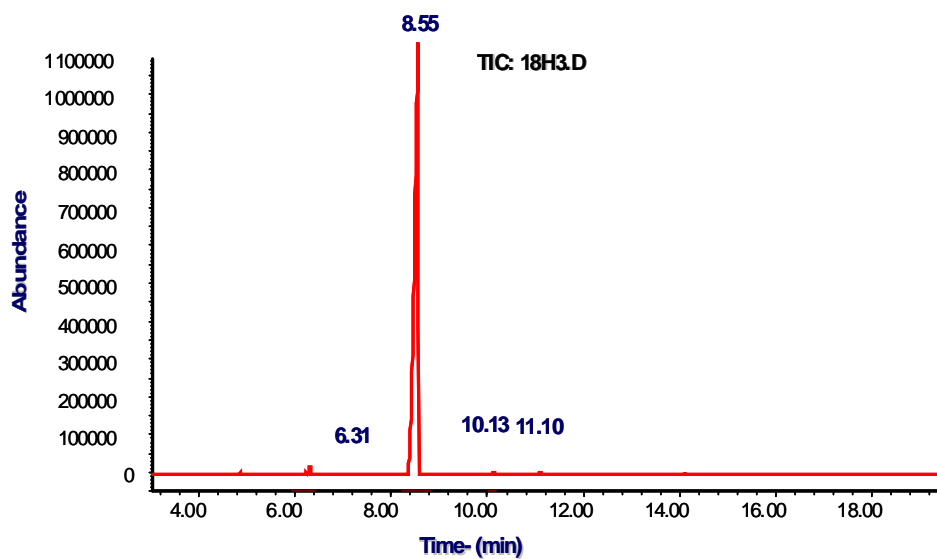

**Figure B.4 TNT Chromatogram at 18h of irradiation (254nm)**
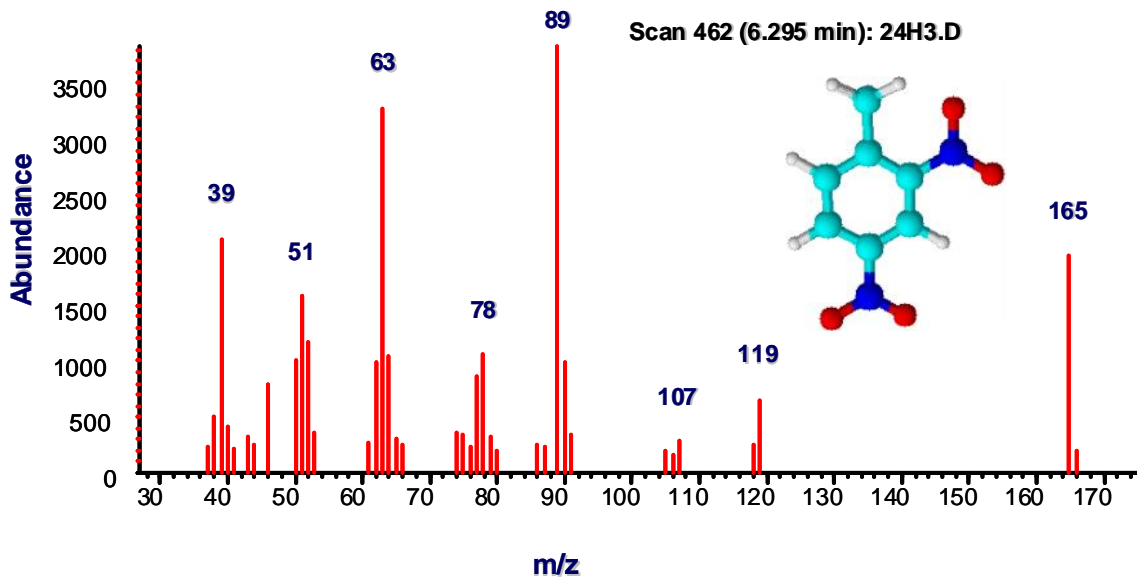
Figure B.5. Total ion chromatogram of degradation product of TNT with a Tr = 6.29min. The library of equipment identify the product as 2,4-DNT
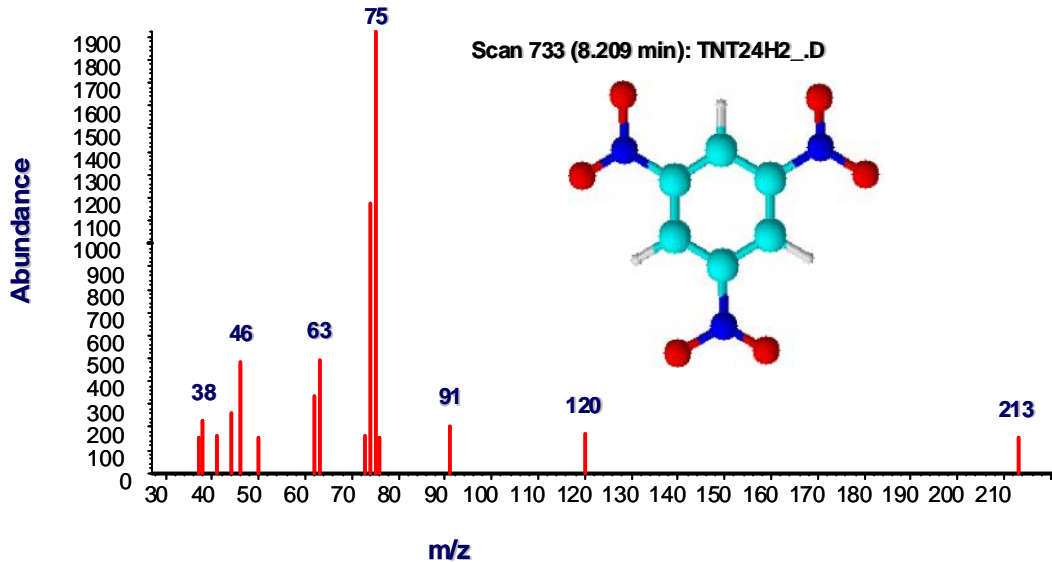

Figure B.6. Total ion chromatogram of degradation product of TNT with a Tr = 8.209min. The library of equipment identify the product as 1,3,5-TNB.
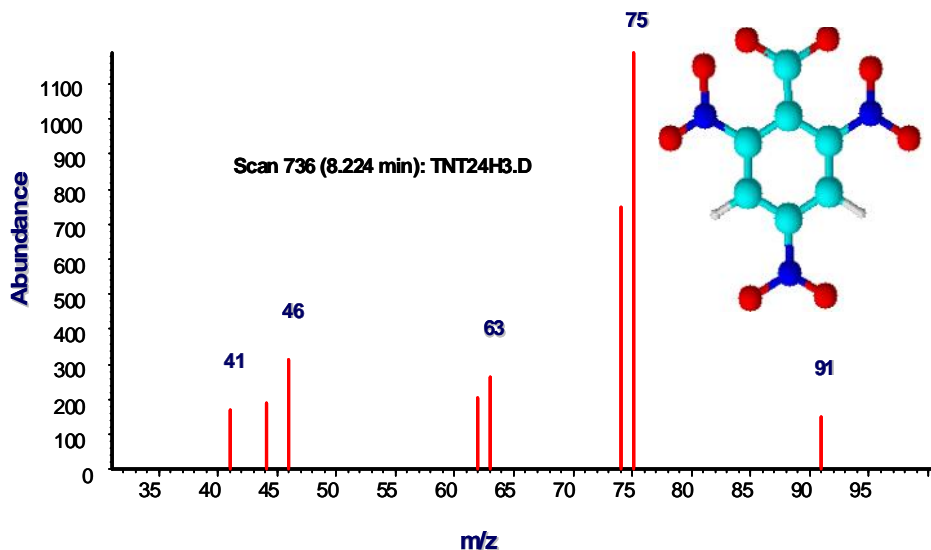
Figure B.7. Total ion chromatogram of degradation product of TNT with a Tr = 8.22 min. The library of equipment identified the product as 2,4,6-trinitrobenzoic acid.
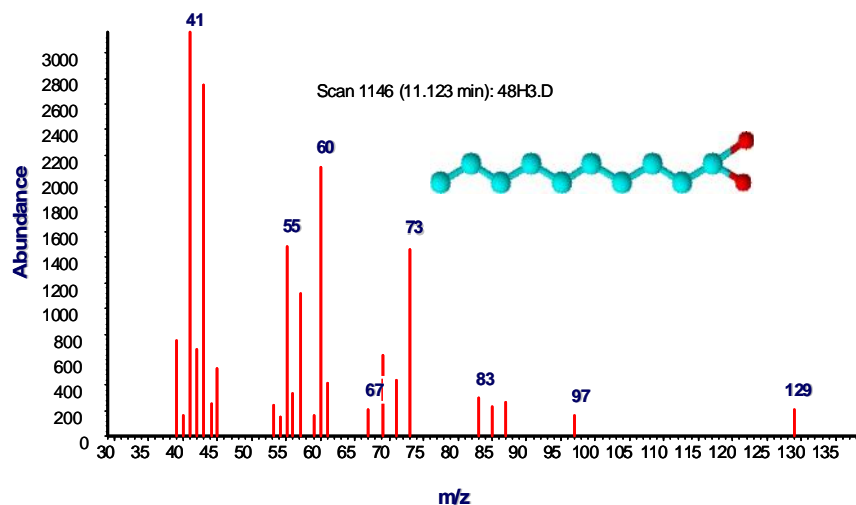

Figure B.8. Total ion chromatogram of degradation product of TNT with a Try = 11.12 min. The library of equipment identified the product as octanoic acid.

Figure B.9 presents the chromatogram of TNT at 0 h of irradiation when iron oxide was added. A chromatogram of an aliquot of mixture TNT –Fe_3O_4 was analyzed by GC/MSD and the result presented degradation products, which are labeled. Several carboxylic acids are presented as products of degradation.
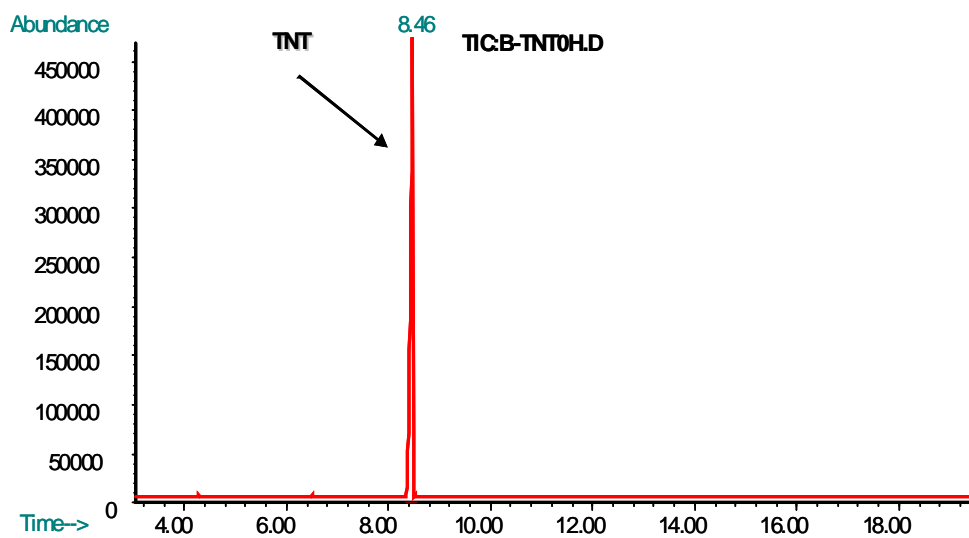
**Figure B. 9. TNT-Fe$_3$O$_4$ mixture chromatogram at 0h of irradiation.**
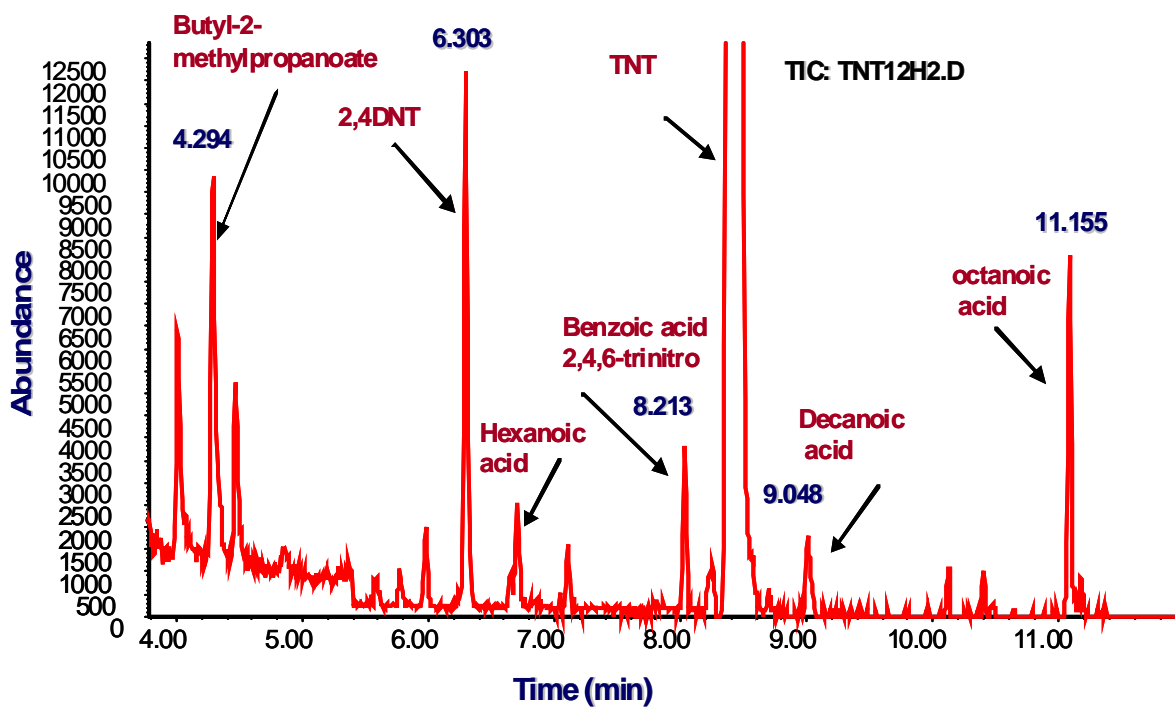
Figure B.10. Chromatogram for TNT at 12 h of irradiation of TNT-Fe$_3$O$_4$ mixture.

117

Table B. 1. Photodegradation products of TNT.

Retention Time (min)	Product	ions
6.295	2,4–dinitrotoluene (2,4DNT)	165
8.209	Benzoic acid 2,4,6-trinitro	75, 213, 120, 91
8.22	1,3,5-trinitrobenzene (1,3,5TNB)	91, 75
8.55	2,4,6 –trinitrotoluene (2,4,6-TNT)	210
11.1	Octanoic acid	149, 129

References

Baez-Angarita, D.B. (2005), 'Detection Of Explosive Vapors from TNT Buried In Sand by Gas Chromatography and Tunable Electron Energy Monochromator-Mass Spectrometry Using HS-SPME', (University of Puerto Rico).

Baez, B., Florian, V., Hernandez-Rivera, S., Cabanzo, A., Correa, S., Irrazabal, M., Briano, J.G., Castro, M. (2006), 'Detection of chemical signatures from TNT buried in sand at various ambient conditions: phase II.', *Detection and Remediation Technologies for Mines and Minelike Targets XI* (Orlando: SPIE International Society Optical Engineering), 62171M.

Bowen, A.T., Conder, J.M., and La Point, T.W. (2006), 'Solid phase microextraction of aminodinitrotoluenes in tissue', *Chemosphere,* 63 (1), 58-63.